VNiVERSiDAD
D SALAMANCA

UNIVERSIDAD DE SALAMANCA
Departamento de Fisica Aplicada

Doctoral thesis

Micromagnetic modeling of magnetization processes and magnetoelastic interactions

---

Author:
Mouad Fattouhi

Supervisors:
Prof. Luis López-Díaz
Prof. Eduardo Martínez

A thesis submitted in fulfilment of the requirements for the degree of Doctor of Philosophy in Applied Physics and Technology at the University of Salamanca

November 15, 2023

The research leading to this doctoral dissertation has received funding from the European union. The author of this thesis gratefully acknowledges financial support from the European Union H2020 Program under Marie Sklodowska Curie Action International training network MagnEFi "MAGNETISM AND THE EFFECTS OF ELECTRIC FIELD" (Grant No. 860060),

Certificado

D. Luis López Díaz, Catedrático de Universidad y D. Eduardo Martínez Vecino, Catedrático de Universidad , ambos miembros del Departamento de Física Aplicada de la Universidad de Salamanca,

Certifican:

Que la presente memoria,“Micromagnetic modeling of magnetization processes and magnetoelastic interactions / Modelado micromagnético de procesos de magnetización e interacciones magnetoelásticas" ha sido realizada bajo su dirección en el Aréa de Electromagnetismo de Física Aplicada de la Universidad de Salamanca por D. Mouad Fattouhi y constituye su Tesis Doctoral para optar al grado de Doctor en Física con Mención Internacional.

En Salamanca, a 14 de Noviembre de 2023

D. Luis López-Díaz

LOPEZ DIAZ LUIS - 07959968J
Firmado digitalmente por LOPEZ DIAZ LUIS - 07959968J
Fecha: 2023.11.15 14:11:40 +01'00'

D. Eduardo Martínez Vecino

MARTINEZ VECINO EDUARDO - 10203187L
Firmado digitalmente por MARTINEZ VECINO EDUARDO - 10203187L
Fecha: 2023.11.15 13:34:28 +01'00'

Abstract

Efficient control of the static and dynamic properties of magnetic textures at the nanoscale is one of the key elements towards energy-efficient spintronics. The control of magnetic textures such as domain walls and skyrmions can be achieved using several methods, including magnetic field, spin-polarized current, and laser pulses. These approaches opened up new avenues towards exploring spintronics-based applications such as racetrack memories, logic gates, artificial neuron synapses, and sensors. However, the growing need to minimize the energy consumption of computational and data storage devices imposes the to find new alternatives to control magnetic systems. One of the promising alternatives that has emerged in the last few years is the use of electric fields. It has been shown that in artificial multiferroics, electric field-induced strain can be used to achieve efficient control over magnetic systems via magnetoelastic coupling. This method showed great potential due to its low energy dissipation rates. Despite these achievements, the strain effects on magnetic systems are still a topic of fundamental research. The aim of this thesis is to explore new ways to use strain to control the statics and dynamics of magnetization in ferromagnetic systems by means of micromagnetic simulations as well as analytical models.

First, using electro-mechanical and micromagnetic simulations, we propose a new method to control the current-driven skyrmion motion. We show that in a piezoelectric/magnetic device, a transverse strain gradient can be created due to the non-uniform electric field profile in the piezoelectric layer. Such a strain gradient will be transferred to the magnetic system, inducing a force on the skyrmions that can be used to control their dynamics. In particular, we demonstrate that such a force tunes the skyrmion Hall effect in both ideal and disordered films.

In the second part, we focus on exploring the effects of both uniform and space-dependent strain on magnetic domain walls (DWs) in perpendicularly magnetized ferromagnetic strips. We show that uniform in-plane strains enable efficient switching of the DW state between Néel and Bloch configurations. Then, we demonstrate that both in-plane and out-of-plane strain gradients can drive DW motion in the absence of magnetic fields and spin-polarized current. On one hand, we find that the effect of an out-of-plane strain gradient on a DW is equivalent to that of an external field. In-plane strain gradients, on the other hand, induce particular dynamics where

the DW does not exhibit Walker breakdown. We demonstrate that this dynamics relies on the dependency of the internal DW angle on the local strain, which results in a new damping torque that prevents the onset of turbulent DW motion.

In the last part of this thesis, we put emphasis on the spin-orbit torque (SOT) driven Néel DWs stabilized via uniform in-plane strain. We show that in narrow strips, such DWs move with a velocity that depends linearly on the applied current up to a threshold value, where their velocity starts gradually decreasing and subsequently vanishes. We attribute this behavior to the precessional SOT that changes the DW internal configuration from Néel to Bloch, which eventually cancels out the torques contributing to the system. In wide strips, we again find that the DW stops moving beyond a certain threshold current; however, its internal structure exhibits a non-uniform pattern with complex transient dynamics. We explore this transient dynamics using micromagnetic simulations as well as an extended one-dimensional (1D) model that accounts for both time and space variations of the DW coordinates. Using this extended model, we demonstrate that the DW internal structure a regular ripple structure with 180° kinks, with the kink width being dependent on the exchange interaction and the magnetoelastic anisotropy. Besides, we note distortions in the DW shape, which we attribute to the competition between SOT and the exchange torque.

Resumen

El control eficiente de las propiedades estáticas y dinámicas de las texturas magnéticas es uno de los elementos clave hacia una spintrónica más eficiente desde el punto de vista energético. El control de texturas magnéticas como las paredes de dominio (DW, por sus siglas en inglés) y skyrmiones se ha logrado utilizando varios métodos, incluyendo campos magnéticos, corrientes de espín y pulsos láser. Estos enfoques han abierto nuevas vías para explorar aplicaciones basadas en la spintrónica, como memorias magnéticas, puertas lógicas, neuronas artificiales y sensores. Sin embargo, la creciente necesidad de minimizar el consumo de energía de los dispositivos informáticos y de almacenamiento de datos impone la necesidad de encontrar nuevas alternativas para controlar sistemas magnéticos. Una de las alternativas más prometedoras que ha surgido en los últimos años es el uso de campos eléctricos. Se ha demostrado que en multiferroicos artificiales, la deformación mecánica inducida por un campo eléctrico puede utilizarse para lograr un control eficiente sobre sistemas magnéticos mediante el acoplamiento magnetoelástico. Este método ha mostrado un gran potencial debido a sus bajos índices de disipación de energía. A pesar de estos logros, la manipulación de la respuesta magnética mediante esfuerzo mecánico sigue siendo un tema de investigación fundamental.

El objetivo de esta tesis es explorar nuevas formas de utilizar la deformación para controlar la estática y dinámica de la magnetización en sistemas ferromagnéticos a través de simulaciones micromagnéticas y modelos analíticos.

En primer lugar, utilizando simulaciones electro-mecánicas y micromagnéticas, proponemos un nuevo método para controlar el movimiento de skyrmiones impulsado por corriente. Mostramos que en una estructura piezoeléctrica/magnética aparece un gradiente de deformación transversal debido al perfil no uniforme del campo eléctrico en la capa piezoeléctrica. Este gradiente de deformación se transferirá al sistema magnético, induciendo una fuerza sobre los skyrmiones que se puede utilizar para controlar su dinámica. En particular, demostraremos que esta fuerza controla el efecto Hall de los skyrmiones tanto en películas ideales como en otras realistas.

En la segunda parte, nos centramos en explorar los efectos de una deformación, tanto uniforme como variable espacialmente, en la estructura y el movimiento de

paredes en tiras ferromagnéticas magnetizadas perpendicularmente. Mostramos que una deformación uniforme en el plano permite un cambio en la configuración de las paredes de dominio entre patrones de Néel y Bloch. Seguidamente, mostramos que es posible utilizar gradientes de deformación tanto en el plano como fuera del plano para impulsar el movimiento de las paredes de dominio en ausencia de campos magnéticos y corrientes de espín. Por un lado, encontramos que los gradientes de deformación fuera del plano son similares a los campos externos en términos de movimiento de las paredes de dominio. Por otro lado, mostramos que los gradientes de deformación en el plano inducen una dinámica particular en la que la pared de dominio no muestra la transición al régimen turbulento. Demostramos que esta dinámica depende del ángulo interno de la pared y de la deformación local, lo que resulta en un nuevo torque de amortiguamiento que evita el inicio del movimiento turbulento de la pared.

En la última parte de esta tesis, se estudia el comportamiento de las paredes de dominio de Néel impulsadas por corrientes de espin generados por acoplamiento espin-orbita (SOT) y estabilizadas mediante deformación uniforme en el plano. Mostramos que, en tiras estrechas, estas paredes se mueven con una velocidad que aumenta casi linealmente hasta un umbral de corriente, a partir de la cual su velocidad comienza a disminuir gradualmente y finalmente se anula. Atribuimos este comportamiento al SOT precesional, que cambia la configuración interna de la pared de Néel a Bloch, lo que finalmente anula los torques que contribuyen al sistema. En tiras anchas, nuevamente encontramos que la pared deja de moverse más allá de un cierto umbral de corriente. Sin embargo, su estructura interna exhibe un patrón no uniforme con una dinámica transitoria compleja. Exploramos esta dinámica transitoria utilizando simulaciones micromagnéticas, así como un modelo extendido en una dimensión que tiene en cuenta las variaciones tanto temporales como espaciales de las coordenadas de la pared de dominio. Utilizando dicho modelo, demostramos que la estructura interna de la pared de dominio adopta una configuración espacial caracterizada por la presencia de transiciones de 180º localizadas, cuya anchura depende de la interacción de intercambio y la anisotropía magnetoelástica. Además, observamos distorsiones en la forma de la pared, que atribuimos a la competencia entre el SOT y el torque de intercambio.

Acknowledgements

Now I am at the most challenging part of this thesis. It is tough because it makes me realize that my journey in Salamanca has come to an end. However, I cannot finish this journey without expressing my gratitude to the incredible people I have had the privilege of working with over the past three years. We have shared coffee breaks, discussions, lunches, papers, and even some unsuccessful attempts for winning the "Loteria de Navidad" (let's be honest, we never had a chance!). So, this chapter is dedicated to the people who have had a significant impact on both my professional and personal life during my time in Salamanca.

First and foremost, I want to express my deep gratitude to Luis López-Díaz for giving me the incredible opportunity to work in his wonderful research group and conduct research at such a high level. He has been there to discuss physics with me and listen to my ideas regardless how stupid they are. He patiently read my horrible writings and helped me improve them. I am thankful for the extensive knowledge he shared about micromagnetism, computational physics, elastodynamics, and various other concepts. He also taught me how to present and write effectively and patiently corrected this manuscript multiple times. I want you to know that you are an excellent supervisor who fosters a positive atmosphere for creativity and innovation. I would never reach this point without your guidance.

I am truly thankful to Eduardo Martínez for being my guide throughout this journey. He was always enthusiastic about discussing new ideas in fields like spintronics, nanomagnetism. Thanks to him, I learned how to be precise and accurate, and he also corrected my papers and reviewed this thesis. Without his hard work, this thesis wouldn't have turned out so well. You are such an amazing scientist and a careful supervisor, and I consider myself lucky to have worked with you.

I want to give a big thanks to Felipe García-Sánchez and Rocío Yanes. They are not just great coworkers, but also fantastic friends outside of work. Felipe, your questions about chaos have given me some real brain teasers, and your help both in and out of the office has been invaluable. Rocio, you are a passionate physicist. I want you to know that I enjoyed a lot of our multi-scale discussions ranging from ab initio to micromagnetics (don't worry, I will never forget your advice!).

I reserve a place of profound gratitude for André Thiaville, whose exceptional collaboration has illuminated our path, generously sharing his immense knowledge, and graciously engaging in discussions on our results. Being guided by you is a real privilege for me, and I am deeply honored to have had the opportunity to meet such a distinguished scientist in my academic journey.

I would like to express my appreciation to the members of the SINAMAG group, namely Luis Torres, Ana García, Marcelino Zazo, Víctor Raposo, José-Antonio Novoa, Amina Hadjoudja, and Amina Mazouz. Their contributions have created a pleasant and productive work environment. Thank you for the shared coffee breaks, and meaningful scientific meetings. I extend a particular note of gratitude to Víctor for his valuable assistance with technical matters and his insightful discussions regarding numerical simulations. I also want to express my gratitude to David Osuna for our discussions about future plans and for his invaluable advice.

I would like to express my sincere gratitude to MagneFI PIs Dafiné Ravelosona, Reinoud Lavrijsen, Gianfranco Durin, Liza Herrera Diez, Andreas Kehlberger and Mathias Kläui for their invaluable discussions about physics and their invaluable advice.

To the exceptional MagnEFi ESR Fellows, I want to convey my heartfelt appreciation. Subhajit, Rohit, Adriano, Jintao, Golam, Adithya, Beatrice, Adrien, Pingzhi, Sreeveni, Cristina, Mandy, and Giovanni, you all have not only been outstanding colleagues but also wonderful friends. I consider myself lucky to have had the privilege of meeting each one of you.

I would like to extend a special thank you to Clare, our dedicated MagnEFi project manager, for her unwavering professionalism and invaluable assistance in navigating the complexities of bureaucracy and paperwork.

Big thanks to Alberto and Vicente for keeping us energized with their awesome coffee shots and tasty pinchos.

A huge thank you to my mom and dad! They have been there for me through every step of my academic journey. I couldn't have made it this far without their support and encouragement. Grateful for everything they have done!

Lastly, I want to thank my wife for her endless love, support, and encouragement.

À mes parents
À mes grands-parents

Contents

List of Figures

Abbreviations

MRAM	Magnetic random access memory.
CMOS	Complementary metal-oxide semiconductor.
AMR	Anisotropic magnetoresistance.
TMR	Tunnel magnetoresistance.
GMR	Giant magnetoresistance.
DW	Domain Wall.
SkHE	Skyrmion Hall effect.
SAF	Synthetic antiferromagnet.
MTJ	Magnetic tunnel junction.
SOC	Spin-orbit coupling.
PMA	Perpendicular magnetic anisotropy.
PZ	Piezoelectric.
IP	In plane.
FM	Ferromagnet.
HM	Heavy metal.
DMI	Dzyaloshinskii-Moriya interaction.
iDMI	Interface Dzyaloshinskii-Moriya interaction.
LL	Landau-Lifshitz.
LLG	Landau-Lifshitz-Gilbert.
SHE	Spin Hall effect.
SOT	Spin-orbit torque.
FDM	Finite differences method.
FEM	Finite elements method.
FFT	Fast Fourier transform.
GPU	Graphical processing unit.
CPU	Central processing unit.
1DM	one-dimensional model.
μ**M**	Micromagnetic.

WB	Walker breakdown.
BL	Bloch line.
VBL	Vertical Bloch line.
LSA	Linear stability analysis.
RHS	Right hand side.
FTCS	Forward-time centered difference.
BCs	Boundary conditions.

Symbols

Symbol	Description	Unit
$\boldsymbol{\mu}$	Magnetic moment	$\mathrm{A\,m^2}$
$\mathbf{B}$	Magnetic field	T
$\boldsymbol{\tau}$	Torque	$\mathrm{N\,m}$
f_L	Larmor frequency	Hz
γ	Gyromagnetic ratio	$\mathrm{rad\,s^{-1}\,T^{-1}}$
$\hbar$	Reduced Planck constant	$\mathrm{J\,s}$
e	Electron charge	C
$\mathbf{M}$	Magnetization	$\mathrm{A\,m^{-1}}$
M_s	Saturation magnetization	$\mathrm{A\,m^{-1}}$
$\mathbf{m}$	Normalized magnetization $\mathbf{M}/M_\mathrm{s}$	
A_ex	Exchange stiffness	$\mathrm{J\,m^{-1}}$
D	Interface DMI constant	$\mathrm{J\,m^{-2}}$
K_u	Uniaxial anisotropy constant	$\mathrm{J\,m^{-3}}$
K_s	Surface anisotropy constant	$\mathrm{J\,m^{-2}}$
K_sh	Shape anisotropy constant	$\mathrm{J\,m^{-3}}$
K_bulk	Bulk anisotropy constant	$\mathrm{J\,m^{-3}}$
$\mathbf{H}_\mathrm{ext}$	External magnetic field	$\mathrm{A\,m^{-1}}$
$\mathbf{H}_\mathrm{d}$	Demagnetizing field	$\mathrm{A\,m^{-1}}$
$\mathbf{H}_\mathrm{mel}$	Magnetoelastic field	$\mathrm{A\,m^{-1}}$
$\mathbf{H}_\mathrm{DMI}$	DMI field	$\mathrm{A\,m^{-1}}$
$\mathbf{H}_\mathrm{eff}$	Effective field	$\mathrm{A\,m^{-1}}$
E	Energy	J
$\mathcal{E}$	Energy density	$\mathrm{J\,m^{-3}}$
B_1	First magnetoelastic coupling constant	$\mathrm{J\,m^{-3}}$
B_2	Second magnetoelastic coupling constant	$\mathrm{J\,m^{-3}}$
ε_{ij}	Mechanical strain	
σ_{ij}	Mechanical stress	Pa
λ_s	Saturation magnetostriction	
α	Gilbert damping	
$\mathbf{J}$	Electric current density	$\mathrm{A\,m^{-2}}$
θ_sh	Spin Hall angel	

Symbol	Description	Unit
t_{FM}	Ferromagnetic layer thickness	m
$\mathcal{U}_{\mathrm{DW}}$	DW surface energy	$\mathrm{J\,m^{-2}}$
q	DW position	m
φ	DW angle	rad
Δ	DW width	m
v, V	Velocity	$\mathrm{m\,s^{-1}}$
C_{ij}	Elastic constant	Pa
$\mathcal{Y}$	Young modulus	Pa
ν	Poisson ratio	
t	Time	s

1 Introduction

Spintronics, short for "spin electronics", is a scientific field that investigates the interplay between electron spin and charge [1]. This area of research has shown great potential since the discovery of Giant Magnetoresistance by Albert Fert and Peter Grunberg, for which they were awarded the Nobel Prize in 2007 [2, 3]. Spintronics has served as the foundation for various devices such as magnetic random-access memories (MRAMs) [4, 5], logic gates [6–9], racetrack memories [10, 11], sensors[12, 13], and artificial neuron synapses [8, 14–16]. Despite the technological advancements, spintroncis is still a topic of investigation in terms of the challenges related to energy costs and data capacity [17, 18]. Compared to complementary metal-oxide semiconductor technology (CMOS), spintronics offers a promising pathway towards a significant reduction in energy consumption, enhanced device battery life, and fast operation speed since the spin of an electron can be manipulated in a faster timescale than its charge. However, spintronics is still in the early stages compared to CMOS, and physicists are continuously exploring routes to improve its capabilities.

The development of reliable devices for spintronics applications involves a good understanding of magnetic systems and their dynamics at the nanoscale. The concept of magnetism is related to the atomic magnetic moment, which is a result of the spin and orbital momentum of the electrons orbiting around the nucleus [19]. In materials, magnetism originates from the interacting magnetic moments, resulting in different magnetic orders such as ferromagnetism, antiferromagnetism, and ferrimagentism [20]. Ferromagnetic materials, in particular, were the first building blocks of spintronic devices since they provide a net magnetic moment, allowing their measurement using simple experimental techniques. The atomic magnetic moments in such materials align in parallel, providing strong permanent magnetization (magnetic moment per unit volume) in the absence of external magnetic fields. To minimize their energy, ferromagnets tend to divide into multiple regions, where the orientation of the magnetic moments changes from one region to another. These uniformly magnetized regions are commonly called magnetic domains.

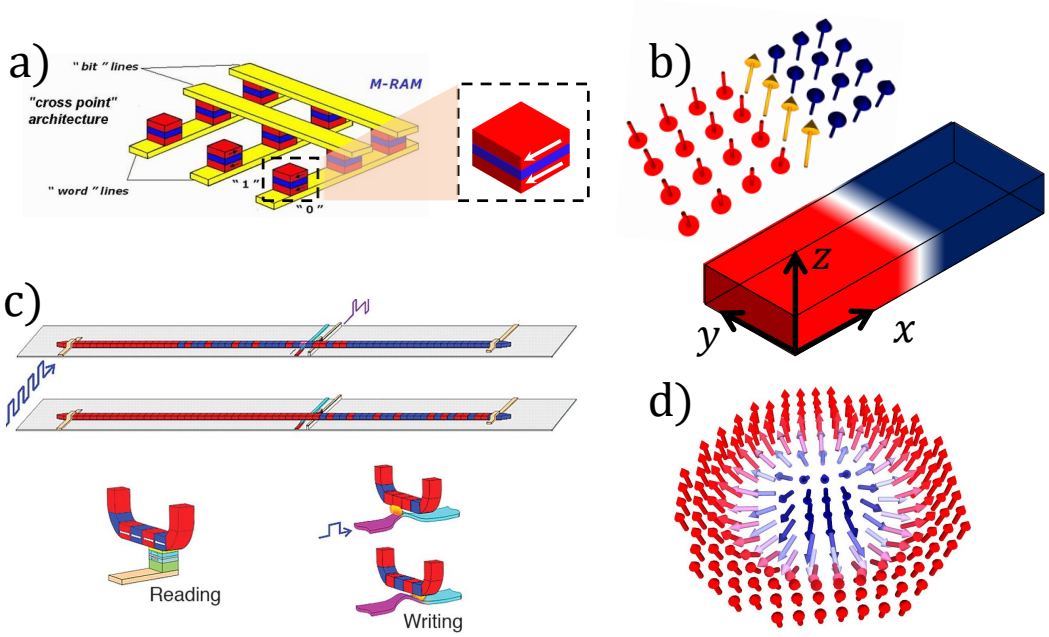

Fig. 1.1.: a) Overview of the Magnetic Random Access Memory (MRAM) architecture using an array of Magnetic Tunnel Junctions (MTJs) for data storage. The inset depicts a single MTJ consisting of two ferromagnetic layers separated by a metallic layer. The lower layer, known as the fixed layer, maintains a constant magnetization direction, while the upper layer, referred to as the free layer, allows for reversible magnetization switching. In MRAMs, information is encoded using the relative magnetic orientations of these layers: "0" when they are parallel and "1" when they are antiparallel. The resistance of the MTJ changes based on this alignment, facilitating data read and write operations. Adapted from [4]. b) Schematic representation of a magnetic Domain Wall (DW) showing two antiparallel magnetic domains separated by a gradual transition in magnetization. c) Schematics of the magnetic Racetrack Memory concept, where a ferromagnetic nanowire contains multiple magnetic domains separated by DWs. Data is encoded based on the presence or absence of these DWs, and it is transported using highly polarized spin currents that drive the DWs along the wire. The inset illustrates the components for reading and writing data in racetrack memory. Data retrieval involves measuring the TMR of an MTJ element connected to the racetrack. Writing data is achieved by employing the fringing fields of a DW manipulated within a second ferromagnetic nanowire oriented perpendicular to the storage nanowire. Adapted from [10]. d) Illustration of a magnetic skyrmion structure.

Manipulating the magnetization of a ferromagnet is traditionally done using a variety of techniques including magnetic fields and spin-polarized currents. This allowed for the discovery of several magneto-resistive effects [21–23] such as anisotropic magnetoresistance (AMR), tunneling magnetoresistance (TMR), and the giant magnetoresistance (GMR), which paved the way for the first realization of MRAMs and sensors as shown in Fig.1.1(a). The discovery of magnetic textures offered more versatility for magnetization manipulation. Magnetic domain walls (DWs) are gradual transitions of magnetization between two adjacent domains oriented in different directions, as shown in Fig.1.1(b). Efficient DW dynamics was a key element in opening avenues to explore a new generation of spintronic devices, such as the DW-based racetrack memory proposed by S. Parkin in 2008 [10]. This type of memory offers advantages like non-volatility, high-density storage, and fast access time. The racetrack memory, which is shown in Fig.1.1(c), is based on the motion of magnetic domains along a nanowire. The data in such memory is encoded in the domains between adjacent DWs or in the DW itself. This technology has the potential to overcome the limitations of traditional RAMs, such as their volatile nature and limited scalability.

The discovery of topological 2D magnetic textures, such as magnetic skyrmions, marked a breakthrough in the history of spintronics. Skyrmions were first proposed theoretically by A.N. Bogdanov in 1989 [24] and later observed experimentally by S. Muhlbauer et al. in 2009 using neutron scattering techniques [25]. Afterwards, extensive research has been conducted to study their static and dynamic properties [26–31]. Skyrmions, which are twisting magnetization textures (see Fig.1.1(d)), are considered topologically protected with a significant robustness against defects and thermal fluctuations that typically exist in real devices. However, they have exhibited undesired properties, such as the skyrmion Hall effect (SkHE). SkHE occurs when skyrmions are subjected to an external driving force and deviate from their path due to the gyrotropic nature of magnetization dynamics. This effect is detrimental to the performance of skyrmion-based devices, such as racetrack memories, where skyrmions are intended to follow a straight path from the writing to the reading elements of the track. To solve this problem, researchers proposed several methods, such as the use of synthetic antiferromagnets (SAF) (two ferromagnetic layers coupled antiferromagnetically via metallic spacer) [32], narrow magnetic films to confine the skyrmion between the system boundaries [33], or engineering the spin-orbit coupling (SOC) in the system [34]. The good understanding of skyrmion physics plays a pivotal role in the development of many skyrmion-based computing devices, including logic [14, 35–37], neuromorphic [38, 39], and memory applications [40, 41].

There is a growing need to explore methods that provide more freedom to drive or control magnetization dynamics [42]. In recent years, one promising approach has been the use of hybrid heterostructures, including multiferroics [43–45]. In such systems, the magnetization control can be accomplished using direct or indirect electric field effects. While direct electric field effects allow the magnetization control through magnetoelectric effect [46], indirect effects enable the magnetization manipulation via secondary mechanisms such as electric field-induced strain [47, 48]. Mechanical strain has been demonstrated to be an efficient tool to control magnetization in different systems [49–52]. Motivated by these facts, the aim of this thesis is to explore possible ways of using strain to drive or control magnetization dynamics in perpendicularly magnetized systems, using a combination of micromagnetic simulations and analytical models. Our goal is to study the potential of strain-based magnetization control and unveil its underlying physical mechanisms.

This thesis is structured in the following way:

Chapter 2 is devoted to presenting the theoretical background of this work. We will begin with an overview of the basic concepts of magnetism and introduce the micromagnetic formalism. Subsequently, we will discuss magnetization dynamics, introducing the Landau-Lifshitz-Gilbert equation, and addressing the additional torques arising from spin-polarized currents. Finally, we will explore magnetic patterns, DWs, and skyrmions in particular, discussing their static and dynamic properties from the micromagnetic perspective.

In chapter 3, we propose a strain-based approach to control the SkHE for current-driven skyrmion dynamics. We demonstrate that using the inverse piezoelectric effect, a transverse strain gradient can be generated in hybrid piezoelectric/magnetic systems. Due to the magnetoelastic coupling, this gradient generates a force acting on the skyrmions that can be used to control their trajectories for any arbitrary applied current. Moreover, we show that our proposed method works efficiently in the presence of structural disorder and enables the control of skyrmion motion with moderate voltages.

In chapter 4, we investigate the influence of uniform and space-dependent strain on magnetic domain walls in perpendicularly magnetized systems. On one hand, a uniform strain is shown to enable reversible switching of the DW configuration at rest between the Bloch and Néel patterns. On the other hand, strain gradients are used to drive magnetic domain walls in the absence of magnetic fields and external currents. We demonstrate that due to the dependence of the domain wall energy on the in-plane strain, it moves rigidly regardless of the strain gradient strength.

Furthermore, we demonstrate that average DW velocities in the range of 500 m/s can be obtained using voltage-induced strain in piezoelectric/ferromagnetic devices under realistic conditions.

Chapter 5 is devoted to investigating current-driven Néel DW dynamics in presence of uniform in-plane strain. The work is be based on micromangetic simulations and analytical models and it demonstrates that bistable Néel DWs stabilized by non-chiral interaction (in-plane strain in our case) exhibit very different dynamics with respect to conventional chiral Néel DWs. The investigation will also show that such DWs behave differently in narrow strips compared to wide ones, which display a much richer behaviour. In particular, the DW internal structure exhibits $180°$-kink structures, which forces the DW to deform adopting a ripple-like shape.

In chapter 6 the main conclusions of work and future perspectives are outlined.

Theoretical background

2

This chapter serves as a theoretical background for our research, providing the necessary tools to understand the behavior of ferromagnetic systems at the nanoscale. It starts by introducing the basic concepts of magnetism. Then, it briefly reviews the micromagnetic theory, a framework that examines magnetic systems by considering continuous magnetization vector fields rather than individual magnetic moments. Within this chapter, we discuss the contributions to the total micromagnetic energy density, which arise from interactions of different nature. Furthermore, this chapter delves into magnetization dynamics governed by the Landau-Lifshitz-Gilbert equation along with its associated torques. It discusses both the static and dynamic properties of magnetic textures, such as DWs and skyrmions, within the micromagnetic formalism. This chapter will serve as the cornerstone for the modeling and analytical investigations discussed within this thesis.

2.1 Basic concepts in magnetism

The magnetic moment is a fundamental quantity in magnetism [53, 54]. From a classical perspective, it can be associated with electrical current loops. The magnetic moment $\boldsymbol{\mu}$ corresponding to a current I circulating through a loop of radius R reads

$$\boldsymbol{\mu} = I \int \mathrm{d}\mathbf{S} = I\pi R^2 \mathbf{n} \tag{2.1}$$

where $\mathbf{S}$ is the surface vector with modulus equal to the surface area of the loop and $\mathbf{n}$ is the vector normal to the surface. The magnetic moment $\boldsymbol{\mu}$ is measured in units of $\mathrm{A\,m^2}$.

Since electric charges have mass, the magnetic moment $\boldsymbol{\mu}$ is closely linked to the angular momentum $\mathbf{L}$

$$\boldsymbol{\mu} = \gamma \mathbf{L} \tag{2.2}$$

where γ is a constant called the gyromagnetic ratio, which is proportional to the mass-to-charge ratio, as we will demonstrate later.

In presence of a uniform magnetic field $\mathbf{B}$, the magnetic moment $\boldsymbol{\mu}$ experiences a torque that reads [20]

$$\boldsymbol{\tau} = \boldsymbol{\mu} \times \mathbf{B} \tag{2.3}$$

Since the torque is related to the time variation of the angular momentum $\boldsymbol{\tau} = \frac{\mathrm{d}\mathbf{L}}{\mathrm{d}t}$ Eq. (2.3) can be transformed into

$$\frac{\mathrm{d}\boldsymbol{\mu}}{\mathrm{d}t} = \gamma \boldsymbol{\mu} \times \mathbf{B} \tag{2.4}$$

This equation dictates that the magnetic moment will precess around the magnetic field $\mathbf{B}$ with a frequency $f_L = \frac{\gamma|\mathbf{B}|}{2\pi}$, which is known as Larmor frequency [55]. The sketch of the magnetic moment preccesion is represented in Fig. 2.1.

The classical description of the magnetic moment can be used to describe the atomic magnetic moment. Let us consider an electron orbiting around a proton. Relying on Bohr's atomic model, an electron in the ground state possesses an angular momentum $\mathbf{L}_e = m_e\, v\, d\, \mathbf{n} = \hbar \mathbf{n}$, with m_e being the electron mass, v its velocity, and d the orbit radius. The electric current generated by the electron motion is $I = -\frac{|e|}{T}$, where $T = \frac{2\pi d}{v}$ is the orbital period and e is the electron charge with negative sign. Hence, the electron magnetic moment reads

$$\mu = I\pi d^2 = -\frac{|e|}{2m_e} L_e = -\mu_{\mathrm{B}} \tag{2.5}$$

where $\mu_{\mathrm{B}} = 9.274 \times 10^{-24} \mathrm{A\,m^2}$ is Bohr magneton, which is commonly used as a unit to measure the magnetic moment at the atomic scale. From Eq. (2.5), we can infer the electron's gyromagnetic ratio $\gamma = -\frac{e}{2m_e}$. The classical description that relies only on the electron orbital angular momentum is not enough to explain the origin of magnetism, and spin, the electron's intrinsic angular momentum, needs to be taken into account. When measured along a specific direction, the spin of an electron takes a value of $S = \pm\frac{\hbar}{2}$. The magnetic moment associated with the spin can be expressed as [55]

$$\boldsymbol{\mu} = -\frac{g\mu_{\mathrm{B}}}{\hbar}\mathbf{S} \tag{2.6}$$

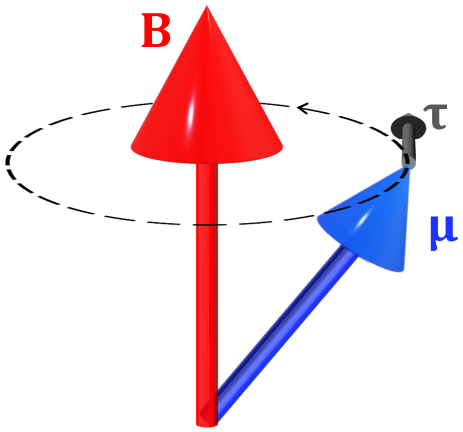

Fig. 2.1.: Illustration of a magnetic moment $\boldsymbol{\mu}$ precessing around a uniform magnetic field $\mathbf{B}$ due to the torque $\boldsymbol{\tau}$

where g is the so-called g-factor, which is approximately $g \approx 2$ for electrons [20].

The quantum origin of the magnetic moment demonstrates the inadequacy of the classical approach to fully explain the underlying principles of magnetism. However, when dealing with materials containing millions of atomic magnetic moments, the quantum approach becomes impractical due to the necessity of solving complex quantum many-body problems [56]. To bridge the gap between the classical and quantum descriptions, a mesoscopic approach known as **Micromagnetism** was developed. In this approach, a magnetization vector is employed to represent the magnetic moment per unit volume, denoted as $\mathbf{M} = \sum \frac{\boldsymbol{\mu}}{V}$, with V representing an elementary volume of dimensions much smaller than the atomic scale. It is considered that the magnetization is uniform within this volume and that it changes smoothly from one elementary volume to another, allowing us to treat $\mathbf{M}$ as a continuous and smooth vector field throughout the system. This is the main assumption of the micromagnetic formalism, which is described in the next section.

2.2 Micromagnetism

Micromagnetism is a theory that describes magnetic materials at the sub-micrometer scale. Unlike purely quantum mechanical theories, micromagnetics does not account for individual spins or the non-deterministic effects. Instead, this theory successfully incorporates essential quantum mechanical effects that underlie ferromagnetism, such as the exchange interaction, within a classical framework that describes magnetization in terms of continuous vector fields. The fundamental assumption in this

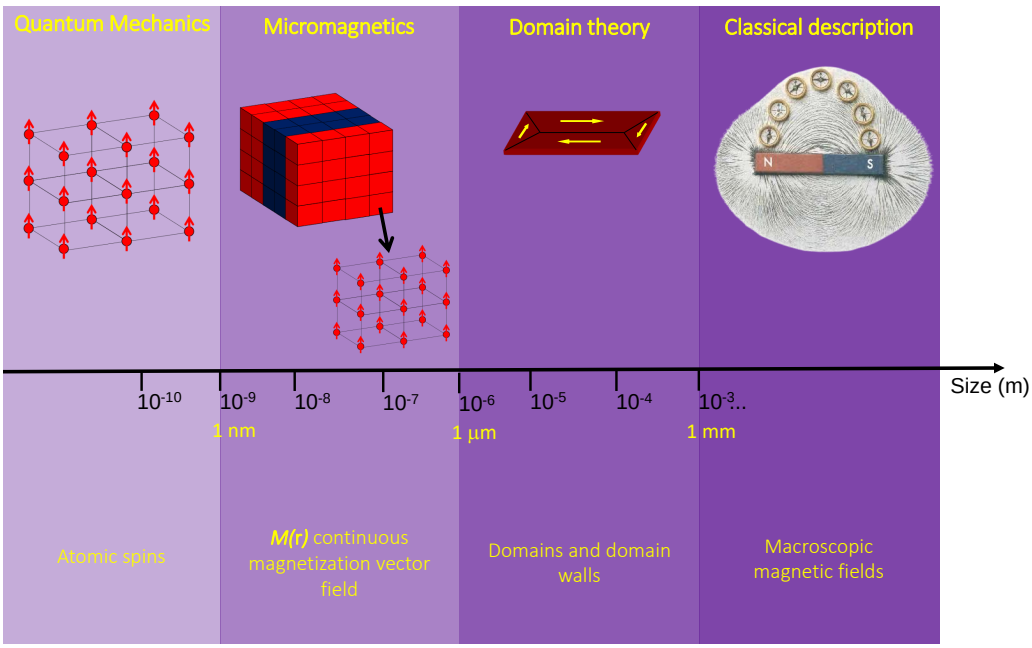

Fig. 2.2.: Diagram illustrating different approaches to describe magnetism across varying length scales. The micromagnetic theory, central to this thesis, operates within the mesoscopic scale, spanning from nanometers to micrometers. This theory treats the magnetization as a smooth vector field.

model is that the exchange interaction within the magnetic material is sufficiently strong to maintain magnetization alignment on a characteristic volume V, significantly larger than the atomic lattice volume a^3 but small enough to resolve magnetic textures such as DWs and skyrmions [57], as illustrated in Fig. 2.2.

In a ferromagnetic specimen, the spin direction changes only by a small angle between neighboring atoms due to the strong exchange interaction. This legitimates the use of the magnetization vector field $\mathbf{M}(\mathbf{r})$ to describe the magnetic system within the micromagnetic theory. This magnetization vector changes smoothly in space and can be expressed as

$$\mathbf{M}(\mathbf{r}) = M_\mathrm{s}\mathbf{m}(\mathbf{r}) \tag{2.7}$$

where M_s is the saturation magnetization that represents the modulus of $\mathbf{M}(\mathbf{r})$ and is considered constant, which is a valid approximation as long as we are well below the Curie temperature $T \ll T_C$ [58]. $\mathbf{m}(\mathbf{r})$ is the normalized magnetization vector, and it is the main variable of micromagnetics. Since we assume a fixed modulus for $\mathbf{m}(\mathbf{r})$, in particular $|\mathbf{m}(\mathbf{r})| = 1$, the derivative of such a vector will always be orthogonal to it, giving

$$\mathbf{m}(\mathbf{r}) \cdot \mathrm{d}\mathbf{m}(\mathbf{r}) = 0 \tag{2.8}$$

This interesting property will be used in later derivations within this thesis.

2.3 Micromagnetic energy terms

In this section, the total micromagnetic free energy is discussed and an overview of the terms involved is provided. Despite the quantum origin of some energy contributions such as exchange and anisotropy [20], micromagnetic theory successfully incorporates them in a semi-classical framework using the assumptions discussed in Sec. 2.2, as will be shown in the following [55].

2.3.1 Exchange energy

The exchange interaction favors the alignment of neighboring spins (i.e. magnetic moments) in the same direction, resulting in the ferromagnetic order. This interaction is a purely quantum mechanical effect, and it is related to the fact that identical fermions (e.g. electrons) must have anti-symmetric wave functions, as the Pauli exclusion principle dictates [59, 60]. Hence, two electrons with the same spin cannot occupy the same position, which minimizes Coulomb energy [56]. The exchange energy between neighboring spins at the atomic scale reads [61]

$$E_{\mathrm{ex}} = -\sum_{ij} J_{ij}(\mathbf{S}_i \cdot \mathbf{S}_j) \tag{2.9}$$

where J_{ij} is the exchange integral between the spin i and j.

Assuming that $\mathbf{S}_i$ and $\mathbf{S}_j$ have the same modulus $|\mathbf{S}|$, Eq. (2.9) can be written as

$$E_{\mathrm{ex}} = -\sum_{ij} J_{ij} \left|\mathbf{S}\right|^2 \cos\phi_{ij} \tag{2.10}$$

where ϕ_{ij} is the angle between the spins $\mathbf{S}_i$ and $\mathbf{S}_j$.

For infinitesimal tilting between two neighboring spins, one can use Taylor expansion where $\cos\phi_{ij} = 1 - \frac{{\phi_{ij}}^2}{2} + \mathcal{O}\left({\phi_{ij}}^4\right)$, which simplifies Eq. (2.10) into

$$E_{\text{ex}} = \text{cst} + \sum_{ij} \frac{J_{ij} \left|\mathbf{S}\right|^2}{2} {\phi_{ij}}^2 \tag{2.11}$$

where $\text{cst} = -\sum_{ij} J_{ij} \left|\mathbf{S}\right|^2$ is a constant.

Considering that $\phi_{ij} = |\mathbf{m}_i - \mathbf{m}_j| \approx (\mathbf{r}_{ij} \cdot \nabla)\, \mathbf{m}$, where $\mathbf{r}_{ij}$ is the distance vector between neighboring spins, the exchange energy per unit volume in the micromagnetic framework reads

$$\mathcal{E}_{\text{ex}} = A_{\text{ex}} \left[(\nabla m_x)^2 + (\nabla m_y)^2 + (\nabla m_z)^2 \right] \tag{2.12}$$

where $A_{\text{ex}} = \frac{2\text{z}J_{ij}|\mathbf{S}|^2}{a}$ being called the exchange stiffness with z is the number of atoms in one unit-cell of the crystal structure, and a is the lattice constant.

2.3.2 Dzyaloshinskii-Moriya energy

Another type of exchange interactions that occurs in magnetic materials is the so-called anti-symmetric exchange, known as Dzyaloshinskii-Moriya interaction (DMI). In 1960, Dzyaloshinskii constructed a model to describe weak ferromagnetism. Based on symmetry arguments, he introduced an asymmetric term to the exchange Hamiltonian that was later named the Dzyaloshinskii-Moriya interaction [62, 63]. Moriya found that the mechanism behind this interaction relies partly on spin-orbit coupling. In a simple description, the mechanism that leads to this anti-symmetric interaction can be seen as a particular case the indirect exchange (see [64] pag. 44), but it includes a non-magnetic atom with strong spin-orbit coupling as sketched in Fig. 2.3. The DMI energy expression at the atomic scale is given as

$$E_{\text{DM}} = \sum_{ij} \mathbf{d}_{ij} \cdot (\mathbf{S}_i \times \mathbf{S}_j) \tag{2.13}$$

In this expression, $\mathbf{S}_i$ and $\mathbf{S}_j$ represent the spins in the neighboring sites and $\mathbf{d}_{ij}$ is the DMI vector, whose magnitude is measured in Joules [63].

The DMI can exist in both bulk and thin magnetic films in different forms. As our work focuses on thin magnetic layers, we will discuss only the interface DM (iDMI). The iDMI occurs typically in thin multi-layers with broken inversion symmetry, such as heavy metal/ferromagnetic (HM/FM) systems, as illustrated in Fig. 2.3 [65, 66]. The iDMI energy per unit volume in the micromagnetic framework reads [67, 68]

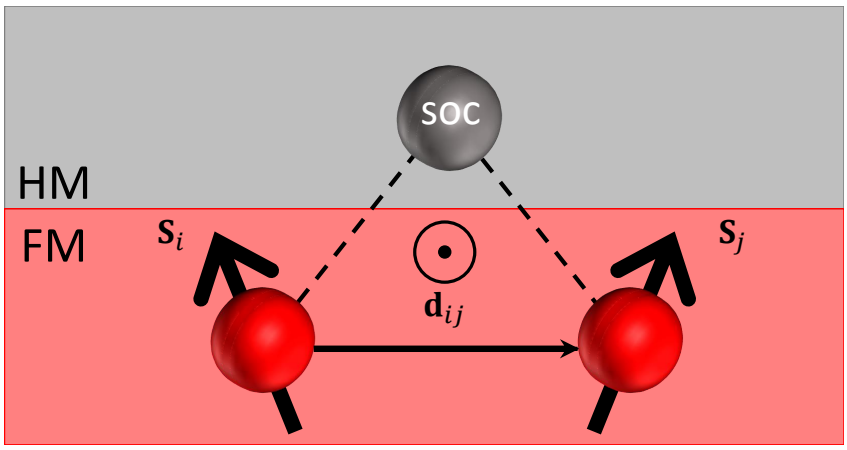

Fig. 2.3.: Schematic representation of the interface Dzyaloshinskii-Moriya interaction mechanism where two ferromagnetic atoms interact through a heavy metal atom with strong SOC.

$$\mathcal{E}_{\mathrm{DM}} = D[(\mathbf{m}\cdot\nabla)m_z - (\nabla\cdot\mathbf{m})m_z] \tag{2.14}$$

where D is the so-called continuous effective DMI constant and is measured in the units of $\mathrm{J\,m^{-2}}$ [69]. The relationship between D and $d = |\mathbf{d}_{ij}|$ depends on the lattice type and is inversely proportional to both the lattice constant a and the film thickness t_{FM}. Specifically, for a simple cubic lattice oriented along the $[001]$ direction, D can be expressed as $D = \frac{d}{a\,t_{\mathrm{FM}}}$. Similarly, in the case of a face-centered cubic lattice oriented along the $[111]$ direction, the relationship reads $D = \frac{d\sqrt{3}}{a\,t_{\mathrm{FM}}}$ [69].

2.3.3 Magneto-crystalline anisotropy energy

The magneto-crystalline anisotropy is associated with the spin-orbit coupling at the quantum scale. In simple words, this type of anisotropy originates from the interaction between the spins and the electric fields of the atomic lattice [20, 64]. This interaction causes the spins to align along a specific crystallographic axis [20]. The symmetry of the lattice structure is responsible for the manifestation of distinct magnetic anisotropy types. For systems with uniaxial anisotropy, the micromagnetic energy density reads

$$\mathcal{E}_{\mathrm{an}} = K_{\mathrm{u}}(1 - (\mathbf{m}\cdot\mathbf{e}_k)^2) \tag{2.15}$$

with $\mathbf{e}_k$ being the unit vector along the easy axis and K_u the uniaxial anisotropy constant measured in the units of $\mathrm{J\,m^{-3}}$.

When examining the role of the uniaxial anisotropy constant K_u on defining the magnetization orientation, we can determine two distinct situations: first, if $K_\mathrm{u} < 0$, the magnetization prefers to lay in the plane perpendicular to $\mathbf{e}_k$, called easy plane. However, if $K_\mathrm{u} > 0$ the magnetization prefers to align with the easy axis $\mathbf{e}_k$. In the case of ultra-thin multilayer structures such as Oxide/FM/HM, an additional contribution to K_u arises due to interfacial effects. This contribution is referred to as surface anisotropy and is due to the spin-orbit interaction with neighboring layers such as heavy metals [70–74]. Surface anisotropy exhibits an inverse scaling relationship with the thickness of the magnetic film and plays a pivotal role in creating PMA [75]. Considering both sources of anisotropy, namely bulk and surface, the uniaxial anisotropy constant can be expressed as

$$K_\mathrm{u} = K_\mathrm{bulk} + \frac{K_\mathrm{s}}{t_\mathrm{FM}} \tag{2.16}$$

where K_bulk is bulk magneto-crystalline anisotropy constant in $\mathrm{J\,m^{-3}}$, K_s is the surface magneto-crystalline anisotropy constant in $\mathrm{J\,m^{-2}}$, and t_FM is the ferromagnetic layer thickness.

2.3.4 Zeeman energy

Zeeman energy is related to the interaction of the magnetic moments with an externally applied magnetic field. It tends to align the magnetization of the system parallel to the field. In the continuum micromagnetics the Zeeman energy per unit volume reads

$$\mathcal{E}_Z = -\mu_0 M_\mathrm{s} \mathbf{m} \cdot \mathbf{H}_\mathrm{ext} \tag{2.17}$$

where $\mathbf{H}_\mathrm{ext}$ is the applied magnetic field in $\mathrm{A\,m^{-1}}$.

2.3.5 Magnetostatic energy

The magnetostatic energy refers to the energy of the magnetic moments in their self-generated magnetic field [76–78]. The magnetostatic field due to the magnetization itself can be obtained from the scalar potential as

$$\mathbf{H}_{\mathrm{d}}(\mathbf{r}) = -\nabla\Phi(\mathbf{r}) \tag{2.18}$$

with

$$\Phi(\mathbf{r}) = \frac{1}{4\pi}\left[\int_{\Omega}\frac{\rho(\mathbf{r}')}{\mid \mathbf{r}-\mathbf{r}' \mid}d\mathbf{r}' + \int_{\partial\Omega}\frac{\sigma(\mathbf{r}')}{\mid \mathbf{r}-\mathbf{r}' \mid}d\mathbf{r}'\right] \tag{2.19}$$

where $\rho = -M_{\mathrm{s}}\nabla\cdot\mathbf{m}$ is the magnetic volume charge density and $\sigma = M_{\mathrm{s}}\mathbf{m}\cdot\mathbf{n}$ is the magnetic surface charge density, with $\mathbf{n}$ being the vector normal to the surface. The magnetostatic energy per unit volume is expressed as

$$\mathcal{E}_{\mathrm{d}} = -\frac{\mu_0 M_{\mathrm{s}}}{2}\mathbf{m}\cdot\mathbf{H}_{\mathrm{d}} \tag{2.20}$$

In the case of uniformly magnetized bodies the averaged magnetostatic field is given by

$$\mathbf{H}_{\mathrm{d}} = -\overline{\mathbf{N}}\cdot\mathbf{M} \tag{2.21}$$

where $\overline{\mathbf{N}}$ is a diagonal tensor called demagnetizing tensor, whose components are called demagnetizing factors.

2.4 Energy minimization and effective field

The total micromagnetic energy includes all the energy contributions discussed within sec. 2.3 and reads

$$E(\mathbf{m}) = \int_V \Big(A_{\mathrm{ex}} \mid \nabla\mathbf{m} \mid^2 + D[(\mathbf{m}\cdot\nabla)m_z - (\nabla\cdot\mathbf{m})m_z] + K_{\mathrm{u}}[1-(\mathbf{m}\cdot\mathbf{e}_k)^2] - \frac{\mu_0 M_{\mathrm{s}}}{2}\mathbf{m}\cdot\mathbf{H}_{\mathrm{d}} - \mu_0 M_{\mathrm{s}}\mathbf{m}\cdot\mathbf{H}_{\mathrm{ext}}\Big)\,\mathrm{d}V \tag{2.22}$$

where the integration extends over the volume V of the ferromagnet.

As shown in Eq. (2.22), the total energy is a functional of the magnetization $\mathbf{m}(\mathbf{r})$, which is a space-dependent vector field. Hence, to find the equilibrium state of the

energy in Eq. (2.22), the latter should be minimized, fulfilling $\delta E = 0$ with δE being its variational. The variation of Eq. (2.22) reads [79]

$$\delta E(\delta\mathbf{m}) = \int_V (2A_{\mathrm{ex}}\nabla\mathbf{m}\cdot\nabla(\delta\mathbf{m}) + D[(\nabla\cdot\mathbf{m})\delta m_z + m_z(\nabla\cdot\delta\mathbf{m}) - \nabla m_z\cdot\delta\mathbf{m} \\ -\mathbf{m}\cdot\nabla\delta m_z] - 2K_{\mathrm{u}}(\mathbf{m}\cdot\mathbf{e}_k)(\mathbf{e}_k\cdot\delta\mathbf{m}) - \mu_0 M_{\mathrm{s}}\delta\mathbf{m}\cdot\mathbf{H}_{\mathrm{d}} - \mu_0 M_{\mathrm{s}}\delta\mathbf{m}\cdot\mathbf{H}_{\mathrm{ext}})\,\mathrm{d}V \tag{2.23}$$

where $\nabla\mathbf{m}\cdot\nabla(\delta\mathbf{m}) = \nabla m_x\nabla(\delta m_x)+\nabla m_y\nabla(\delta m_y)+\nabla m_z\nabla(\delta m_z)$, and the reciprocity theorem was used to evaluate the variational of the magnetostatic energy, since the a variation of $\mathbf{m}$ induces a variation of $\mathbf{H}_{\mathrm{d}}$ [79].

Using the divergence theorem together with the identity $\nabla\cdot(A\mathbf{B}) = A(\nabla\cdot\mathbf{B}) + \mathbf{B}\cdot(\nabla A)$ we can rewrite Eq. (2.23) as

$$\delta E(\delta\mathbf{m}) = -\int_V (2A_{\mathrm{ex}}\nabla\cdot(\nabla\mathbf{m}) - 2D[(\nabla\cdot\mathbf{m})\mathbf{e}_z + \nabla m_z] + 2K_{\mathrm{u}}(\mathbf{m}\cdot\mathbf{e}_k)\mathbf{e}_k \\ +\mu_0 M_{\mathrm{s}}\mathbf{H}_{\mathrm{d}} + \mu_0 M_{\mathrm{s}}\mathbf{H}_{\mathrm{ext}})\cdot\delta\mathbf{m}\,\mathrm{d}V + \oint_S \left(2A_{\mathrm{ex}}\frac{\partial\mathbf{m}}{\partial\mathbf{n}} + D[\mathbf{m}\times(\mathbf{n}\times\mathbf{e}_z)]\right)\cdot\delta\mathbf{m}\,\mathrm{d}S \tag{2.24}$$

where $\mathbf{n}$ is the vector normal to the surface, and we used the fact that $m_z = \mathbf{m}\cdot\mathbf{e}_z \implies \delta m_z = \delta\mathbf{m}\cdot\mathbf{e}_z$ to evaluate the variational of iDMI energy. The first term in the rhs of Eq. (2.24) denotes the integral over the ferromagnetic volume and the second one refers to the integral over the surface. $\frac{\partial\mathbf{m}}{\partial\mathbf{n}}$ is the derivative of the magnetization across the direction normal to the surface.

Eq. (2.24) can be further simplified to

$$\delta E(\delta\mathbf{m}) = -d\int_V (\mu_0 M_{\mathrm{s}}\mathbf{H}_{\mathrm{eff}}\cdot\delta\mathbf{m})\,\mathrm{d}V + \oint_S \left(2A_{\mathrm{ex}}\frac{\partial\mathbf{m}}{\partial\mathbf{n}} + D[\mathbf{m}\times(\mathbf{n}\times\mathbf{e}_z)]\right)\cdot\delta\mathbf{m}\mathrm{d}S \tag{2.25}$$

where the effective field of the system reads

$$\mathbf{H}_{\text{eff}} = \frac{2A_{\text{ex}}}{\mu_0 M_{\text{s}}}\nabla^2\mathbf{m} + \frac{2D}{\mu_0 M_{\text{s}}}[(\nabla\cdot\mathbf{m})\mathbf{e_z} - \nabla m_z] + \frac{2K_{\text{u}}}{\mu_0 M_{\text{s}}}(\mathbf{m}\cdot\mathbf{e}_k)\mathbf{e}_k + \mathbf{H}_{\text{d}} + \mathbf{H}_{\text{ext}} \quad (2.26)$$

Considering the constraint $|\mathbf{m}| = 1$, the variation of the magnetization $\delta\mathbf{m}$ is solely related to the change of the magnetization orientation. Hence, we can express it as $\delta\mathbf{m} = \mathbf{m}\times\delta\theta$, with $\delta\theta$ being the variation of the magnetization orientation. Therefore, for a system without iDMI contribution ($D = 0$), Eq. (2.25) becomes

$$\delta E(\delta\mathbf{m}) \;=\; \mu_0 M_{\text{s}}\int_V (\mathbf{m}\times\mathbf{H}_{\text{eff}})\cdot\delta\theta\,\mathrm{d}V \;+\; \oint_S \left(2A_{\text{ex}}\frac{\partial\mathbf{m}}{\partial\mathbf{n}}\times\mathbf{m}\right)\cdot\delta\theta\,\mathrm{d}S \quad (2.27)$$

As mentioned in the beginning of this section, the minima of the energy functional must satisfy $\delta E(\delta\mathbf{m}) = 0$ for any variations of $\delta\theta$. Hence, Eq. (2.27) implies that equilibrium must fulfill two conditions:

$$\mathbf{H}_{\text{eff}}\times\mathbf{m} = \mathbf{0},\ \forall\mathbf{r}\in V \quad (2.28a)$$

$$\frac{\partial\mathbf{m}}{\partial\mathbf{n}}\times\mathbf{m} = \mathbf{0},\ \forall\mathbf{r}\in S \quad (2.28b)$$

Eq. (2.28a) is generally known as Brown's condition [80] and dictates that in equilibrium, the magnetization is aligned with the effective field at every point of the ferromagnet. On the other hand, Eq. (2.28b) which represents the boundary condition, dictates that the variation of $\mathbf{m}$ normal to the surface S is parallel to $\mathbf{m}$. As mentioned in sec. 2.2, the spatial derivatives of the magnetization $\mathbf{m}$ are always orthogonal to it. Hence, the boundary condition in Eq. (2.28b) is usually reduced to $\frac{\partial\mathbf{m}}{\partial\mathbf{n}} = 0$. In the case of non-zero iDMI ($D \neq 0$), the boundary condition in Eq. (2.28b) is modified to include the iDMI contribution and reads [69, 81]

$$\frac{\partial\mathbf{m}}{\partial\mathbf{n}} = \frac{D}{2A_{\text{ex}}}\mathbf{m}\times(\mathbf{e}_z\times\mathbf{n}) \quad (2.29)$$

2.5 Magnetoelastic energy

Up to here, we discussed the conventional micromagnetic energy terms as well as their corresponding effective fields. However, in this thesis, our aim is to explore the effects of mechanical strain on magnetization static and dynamic processes via magnetoelastic coupling. The magnetoelastic coupling relates to the change in magnetization due to a mechanical deformation. This includes the change of various magnetic interactions such as exchange, DMI, and anisotropy [82–84].

Let us consider that our anisotropy energy density is a function of the magnetization $\mathbf{m}$ and the strain tensor ε_{ij}, where $\mathcal{E}_{\mathrm{an}} = \mathcal{E}_{\mathrm{an}}(\mathbf{m}, \varepsilon_{ij})$. To find out the strain-induced variation of the anisotropy energy density, we expand it in Taylor series at ε_{ij} as

$$\mathcal{E}_{\mathrm{an}} = \mathcal{E}_{\mathrm{an}}(\mathbf{m}, 0) + \sum_{ij} \frac{\partial \mathcal{E}_{\mathrm{an}}(\mathbf{m}, 0)}{\partial \varepsilon_{ij}} \varepsilon_{ij} \tag{2.30}$$

The second term on the rhs of Eq. (2.30) shows the change of the magneto-crystalline anisotropy energy due to the mechanical strain contribution. From Eq. (2.30), the magnetoelastic energy density can be expressed as

$$\mathcal{E}_{\mathrm{mel}} = \sum_{ij} \sum_{kl} B_{ijkl} \left(\mathbf{e}_i \cdot \mathbf{m}\right) \left(\mathbf{e}_j \cdot \mathbf{m}\right) \varepsilon_{kl} \tag{2.31}$$

where we used $\partial_{\varepsilon_{ij}} \mathcal{E}_{\mathrm{an}}(\mathbf{m}, 0) = \sum_{ij} \sum_{kl} B_{ijkl} \left(\mathbf{e}_i \cdot \mathbf{m}\right) \left(\mathbf{e}_j \cdot \mathbf{m}\right)$ as an expansion coefficient with B_{ijkl} being the magnetoelastic coupling tensor and $\mathbf{e}_i$ is the unit vector along the strain direction. Considering cubic symmetry, the magnetoelastic energy density reduces to [85]

$$\mathcal{E}_{\mathrm{mel}} = \sum_{i=x,y,z} B_1 \varepsilon_{ii} m_i^2 + \sum_{i,j=x,y,z} B_2 \varepsilon_{ij} m_i m_j \tag{2.32}$$

where $B_1 = B_{1111}$ and $B_2 = B_{2323}$ are the magnetoelastic coupling tensor components in Voigt notation [86–88].

When magnetized along a specific direction, a magnetostrictive ferromagnet deforms. Its elastic energy reads [89, 90]

$$\mathcal{E}_{\mathrm{el}} = \frac{1}{2} \sum_{ij} \sum_{kl} c_{ijkl} \varepsilon_{ij} \varepsilon_{kl} \tag{2.33}$$

where c_{ijkl} is the elastic stiffness tensor. Assuming cubic symmetry, Eq. (2.33) reads

$$\mathcal{E}_{\text{el}} = \sum_{i=x,y,z} \frac{c_{11}}{2}\varepsilon_{ii}^2 + \sum_{i,j=x,y,z} c_{12}\varepsilon_{ii}\varepsilon_{jj} + \sum_{i,j=x,y,z} 2c_{44}\varepsilon_{ij}^2 \tag{2.34}$$

where $c_{11} = c_{1111}$, $c_{12} = c_{1122}$ and $c_{44} = c_{2323}$ are the elastic tensor component in Voigt notation.

For a uniformly magnetized ferromagnet with a free surface boundary, the spontaneous magnetostrictive deformation can be found by minimizing the sum of Eq. (2.31) and Eq. (2.33) with respect to ε_{ij}. This minimization yields the so-called spontaneous strain tensor $\varepsilon_{ij}^{\text{eq}}$, whose components read

$$\varepsilon_{ii}^{\text{eq}} = B_1 \frac{c_{12} - m_i^2(c_{11} + 2c_{12})}{(c_{11} - c_{12})(c_{11} + 2c_{12})} \tag{2.35a}$$

$$\varepsilon_{ij}^{\text{eq}} = -\frac{B_2}{2c_{44}} m_i m_j \quad \text{for } i \neq j \tag{2.35b}$$

which presents the spontaneous deformation as a function of the magneto-elastic coupling constant and the elastic stiffness constants. On the other hand, the conventional equations used to characterize experimentally the spontaneous magnetostrictive deformation for cubic crystals reads [90]

$$\varepsilon_{ii}^{\text{eq}} = \frac{3}{2}\lambda_{100}(m_i^2 - \frac{1}{3}) \tag{2.36a}$$

$$\varepsilon_{ij}^{\text{eq}} = \frac{3}{2}\lambda_{111} m_i m_j \quad \text{for } i \neq j \tag{2.36b}$$

where λ_{100} and λ_{111} are the magnetostriction constants along the $[100]$ and $[111]$ crystallographic directions, respectively. Note that for an isotropic material $\lambda_{100} = \lambda_{111} = \lambda_s$, with λ_s being the saturation magnetostriction constant.

Comparing the coefficients in Eqs. (2.35) and Eqs. (2.36), we can get the expression of the magnetoelastic coupling constants as

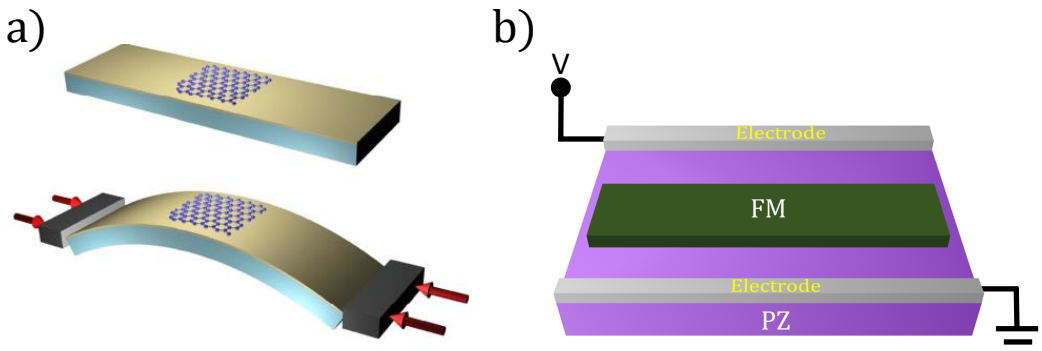

Fig. 2.4.: Illustration depicting two methods of inducing strain in ferromagnetic materials: a) Mechanical bending, where a magnetic thin film adheres to a flexible holder under compression. Adapted from [91]. b) Sketch of a FM/PZ heterostructure, strain in this case is generated by applying a voltage to the piezoelectric layer, which is transmitted to the ferromagnet on top.

$$B_1 = -\frac{3}{2}\lambda_{100}(c_{11} - c_{12}) \tag{2.37a}$$

$$B_2 = -3\lambda_{111}c_{44} \tag{2.37b}$$

Note that the unit of B_1 and B_2 is $\mathrm{J\,m^{-3}}$.

A common method to manipulate the magnetization of ferromagnetic systems is based on applying external strain. This strain can be generated through mechanical bending or by using a piezoelectric (PZ) material, as sketched in Fig. 2.4. It has been demonstrated that in PZ/magnetic heterostructures, a strain as high as 1% can be achieved by applying appropriate potential differences [92]. This strain is significantly larger than the magnetic-induced deformation typically exhibited by a ferromagnet, which is usually around 0.01% [85, 93]. Let us consider an externally strained ferromagnetic system with cubic symmetry. We will disregard the magnetic-induced deformation, as it is usually negligible compared to the externally induced one. This simplification allows us to express the magnetoelastic energy in the continuum approximation by integrating Eq. (2.32) as

$$E_{\mathrm{mel}} = \int_V \left[\sum_{i=x,y,z} B_1 \varepsilon_{ii} (\mathbf{e}_i \cdot \mathbf{m})^2 + \sum_{i,j=x,y,z} B_2 \varepsilon_{ij} (\mathbf{e}_i \cdot \mathbf{m})(\mathbf{e}_j \cdot \mathbf{m}) \right] \mathrm{d}V \tag{2.38}$$

For uniaxial strain ε_{ii} this energy contribution is formally equivalent to the anisotropy one Eq. (2.15), whereas a more complex dependency is found when shear strain ε_{ij} $(i \neq j)$ is present.

As mentioned in Sec. 2.4, to obtain the effective field related to an arbitrary energy contribution its variation over $\mathbf{m}$ should be computed. Following the same procedure in Sec. 2.4 the variational of the magnetoelastic energy reads

$$\delta E_{\mathrm{mel}}(\delta\mathbf{m}) = \int_V \left[\sum_{i=x,y,z} 2B_1\varepsilon_{ii}(\mathbf{e}_i \cdot \mathbf{m})\mathbf{e}_i + \sum_{i,j=x,y,z} B_2\varepsilon_{ij}\left(\mathbf{e}_j \cdot \mathbf{m}\right)\mathbf{e}_i \right. \\ \left. + \sum_{i,j=x,y,z} B_2\varepsilon_{ij}(\mathbf{e}_i \cdot \mathbf{m})\mathbf{e}_j \right] \cdot \delta\mathbf{m}\mathrm{d}V \quad (2.39)$$

The effective field due to the magnetoelastic coupling reads

$$\mathbf{H}_{\mathrm{mel}} = \sum_{i=x,y,z} 2B_1\varepsilon_{ii}(\mathbf{e}_i \cdot \mathbf{m})\mathbf{e}_i + \sum_{i,j=x,y,z} B_2\varepsilon_{ij}\left[(\mathbf{e}_j \cdot \mathbf{m})\,\mathbf{e}_i + (\mathbf{e}_i \cdot \mathbf{m})\mathbf{e}_j\right] \quad (2.40)$$

By adding Eq. (2.40) to Eq. (2.26), we can study the effect of strain on magnetization dynamics, which is the main goal of the present thesis. It is noteworthy, that the magnetoelastic energy does not modify the micromagnetic boundary conditions.

2.6 Magnetization dynamics

As anticipated in Sec. 2.1, in the presence of a uniform magnetic field, magnetic moments experience a torque that triggers their precession around it, as evidenced by Eq. (2.4). The same equation can be used to describe the dynamics of the magnetization vector, but the latter will precess around the local effective field originating from the various interaction involved in the system. However, due to the interaction with the physical environment, the magnetization dynamic is modified and instead of continuous precession the magnetization relaxes progressively and aligns with $\mathbf{H}_{\mathrm{eff}}$ due to energy dissipation [94, 95]. Within continuum micromagnetic theory, this mechanism is phenomenologically described by the Landau-Lifshitz (LL) equation [96], which characterizes the spatially resolved magnetization dynamics in presence of an effective field $\mathbf{H}_{\mathrm{eff}}$. The LL equation was later modified by adding a

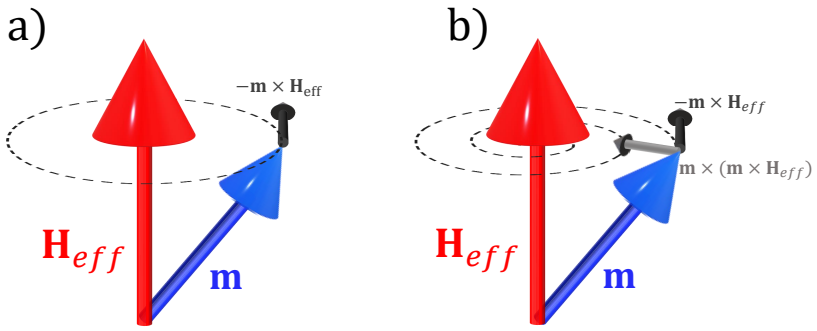

Fig. 2.5.: Schematic representation the magnetization dynamics mechanism. a) Magnetization presession around the effective field due to the precessional torque. c) The magnetization trajectory under the additional action of the damping torque.

phenomenological damping term incorporated by Gilbert [97]. Both formulations are entirely equivalent when appropriate parameter transformations are applied. However, the commonly used equation is the so-called Landau-Lifshitz-Gilbert (LLG) equation, which reads

$$\frac{\mathrm{d}\mathbf{m}}{\mathrm{d}t} = -\gamma_0 \mathbf{m} \times \mathbf{H}_{\mathrm{eff}} + \alpha \mathbf{m} \times \frac{\mathrm{d}\mathbf{m}}{\mathrm{d}t} \tag{2.41}$$

where is $\gamma_0 = |\gamma|\mu_0$ with μ_0 being the vacuum permeability, and α the phenomenological damping constant.

Eq. (2.41) can be written in explicit form if we multiply both sides by $\mathbf{m}$, which yields $\mathbf{m} \times \frac{\mathrm{d}\mathbf{m}}{\mathrm{d}t} = -\gamma_0 \mathbf{m} \times (\mathbf{m} \times \mathbf{H}_{\mathrm{eff}}) - \alpha \frac{\mathrm{d}\mathbf{m}}{\mathrm{d}t}$. Substituting this in Eq. (2.41) gives the Landau-Lifshitz equation mentioned in the beginning of this section

$$\frac{\mathrm{d}\mathbf{m}}{\mathrm{d}t} = -\frac{\gamma_0}{1+\alpha^2} \mathbf{m} \times \mathbf{H}_{\mathrm{eff}} + \frac{\alpha\gamma_0}{1+\alpha^2}\, \mathbf{m} \times (\mathbf{m} \times \mathbf{H}_{\mathrm{eff}}) \tag{2.42}$$

To gain a better understanding of magnetization dynamics and relaxation, let us consider a simplified scenario where all the spins in a magnetic system move together coherently. In this case, we can treat the magnetization as a single spin, also known as a macrospin [98]. Eq. (2.42) describes the behavior of this macrospin subject to the action of an effective field $\mathbf{H}_{\mathrm{eff}}$. The first term on the right-hand side represents a precessional torque. This torque causes the macrospin to undergo a continuous rotation around $\mathbf{H}_{\mathrm{eff}}$ as shown in Fig. 2.5(a). On the other hand, the second term is a damping torque. This torque acts perpendicular to the precessional torque and tends to align the macrospin parallel to the effective field, as shown in Fig. 2.5(b).

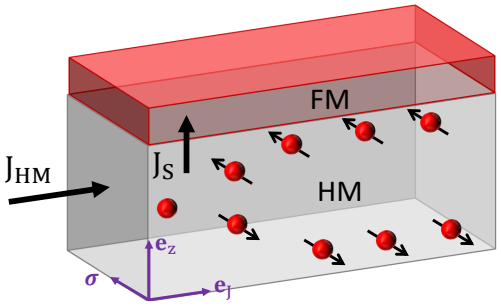

Fig. 2.6.: Schematics of spin Hall effect. A longitudinal charge current, J_{HM}, in heavy metal (HM) is converted into a transverse spin current by spin-orbit scattering. The spin current leads to a spin accumulation at the HM/FM interface that diffuses across the interface into the FM and exerts a torque on the magnetization.

To take into account the contribution of spin-polarized currents on magnetization dynamics, the LLG equation Eq. (2.41) needs to be augmented with external torques. In this thesis, we will limit our discussion to the spin-orbit torque (SOT), which originates from the spin Hall effect (SHE) in FM/HM systems. The spin Hall effect, initially discovered by Mikhail I. Dyakonov in 1971 [99], has been experimentally observed in FM/HM systems with different HM materials. SHE manifests itself when a flow of electric charges traverse through a HM layer with a strong SOC. It leads to a spin accumulation on the surfaces perpendicular to the current direction, that subsequently diffuses into the FM layer exerting a torque on its magnetization, as shown in Fig. 2.6. This torque is called SOT, and expressed as

$$\boldsymbol{\tau}_{\mathrm{SOT}} = \frac{|g_e|}{2}\frac{\mu_{\mathrm{B}} \mathrm{J}_{\mathrm{HM}} \theta_{\mathrm{sh}}}{M_{\mathrm{s}}|e|t_{\mathrm{FM}}}[\mathbf{m} \times (\mathbf{m} \times \sigma) - \mathbf{m} \times \sigma] \tag{2.43}$$

where θ_{sh} is the spin Hall angle, J_{HM} is the charge current density injected to the HM layer and $\boldsymbol{\sigma} = \mathbf{e}_J \times \mathbf{e}_z$ is the spin current polarization with $\mathbf{e}_J$ being the unit vector along the charge current direction as sketched in Fig. 2.6.

The SOT can be added to the LLG equation as an external torque, which become

$$\frac{\mathrm{d}\mathbf{m}}{\mathrm{d}t} = -\gamma_0 \mathbf{m} \times \mathbf{H}_{\mathrm{eff}} + \alpha \mathbf{m} \times \frac{\mathrm{d}\mathbf{m}}{\mathrm{d}t} + \boldsymbol{\tau}_{\mathrm{SOT}} \tag{2.44}$$

2.7 Numerical micromagnetics

As mentioned before in this chapter, micromagnetic theory deals with the behavior of magnetic materials at the nanoscale, typically focusing on magnetic domains,

domain walls and other magnetic textures. Numerical methods play a crucial role in understanding and simulating these complex phenomena. These methods provide means to solve the mathematical equations that govern the magnetic behavior, namely LLG Eq. (2.41). Several numerical methods were used to solve micromagnetic problems, such as finite difference (FDM) and finite element (FEM) methods. While FEM are more suitable for investigating magnetic systems with curved and non-regular shapes such as nanotubes or deformed systems, FDM shows satisfying results in the case of regular systems, particularly for thin films and multilayers. In this work, we used Mumax3 [100], an open-source micromagnetic solver that uses FDM method, to solve LLG equation. Mumax offers built-in energy minimization algorithms, different numerical integration schemes for solving LLG, a friendly user interface and other custom-tailored features to add contributions to the effective field. Mumax3 is based on the FDM methods where the simulated system is discretized in a regular mesh of cuboid cells. To avoid numerical errors, it is essential to chose a cell size smaller than the exchange length $\ell_{\mathrm{ex}} = \sqrt{\frac{A_{\mathrm{ex}}}{\mu_0 M_{\mathrm{s}}^2}}$ or the wall width $\delta_{\mathrm{W}} = \sqrt{\frac{A_{\mathrm{ex}}}{K_{\mathrm{u}} - \mu_0 M_{\mathrm{s}}^2/2}}$ in PMA systems.

In numerical micromagnetics, the magnetostatic contribution is the most time consuming part of the simulation. Mumax takes advantage of the periodic nature of the FDM discretization and evaluates the demagnetizing field as a discrete convolution of the magnetization with the demagnetizing tensor $\bar{N}$ as $\mathbf{H}_{\mathrm{d}\,i} = \bar{N}_{ij} * \mathbf{M}_i$ with $i, j = 1, ..., n$ being the cell number and $(*)$ the convolution product. Mumax uses direct and inverse Fourier transforms together with the convolution theorem to accelerate the demagnetizing field computation [100]. Additionally, the simulations are made using graphical processing units (GPUs) instead of central ones (CPUs), which make mumax a very efficient micromagnetic tool.

2.8 Magnetic textures

2.8.1 Magnetic domain walls

Typically, a bulk ferromagnetic specimen splits into multiple regions known as domains. The magnetization orientation changes from one domain to the next, and the boundaries separating these domains are called magnetic domain walls (DWs). To understand the physical mechanisms involved in the magnetization switching of a ferromagnetic material, it is essential to grasp both the static and dynamic aspects of magnetic DWs. In the context of this thesis, our focus will be primarily on DWs in perpendicularly magnetized thin ferromagnetic strips.

In a thin ferromagnetic strip with PMA, two DW types can appear. On one hand, the so-called Bloch DWs, which typically appear in single FM layers where iDMI is not involved [85]. In a Bloch DW the magnetization rotates gradually about the axis perpendicular to it. On the other hand, the so-called Néel DWs, which usually stabilize in HM/FM thin layers with significant iDMI [67]. Contrary to Bloch DWs, the magnetization in a Néel DW rotates along the axis parallel to it. Fig. 2.7(a) and (b) shows micromagnetic simulation snapshots of the two DW types.

In this section, we will discuss the static and dynamic features of magnetic DWs using a one-dimensional (1D) model. This model maps LLG equation Eq. (2.41) into the DW parameters, namely the DW position q and angle φ, and assumes that the DW profile is one-dimensional [101]. In the derivation of the model we will write LLG in spherical coordinates assuming $\mathbf{m} = (\sin\theta\cos\phi, \sin\theta\sin\phi, \cos\theta)$, with θ and ϕ being the spherical coordinates as sketched in Fig. 2.7(c).

Static properties of a magnetic DW

Let us first examine the static properties of a magnetic DW, namely its width Δ and its internal angle φ (defined as the angle with respect to $x-$axis), which implicitly defines the DW type. We assume that the magnetization changes only along x-axis, and that the DW profile is given by the so-called Walker ansatz (see Appendix. A.1 for detailed derivation of the ansatz) [101, 102], which reads

$$\theta(x,t) = 2\tan^{-1} e^{Q\frac{x-q(t)}{\Delta}}(t) \tag{2.45a}$$

$$\phi(x,t) = \varphi(t) \tag{2.45b}$$

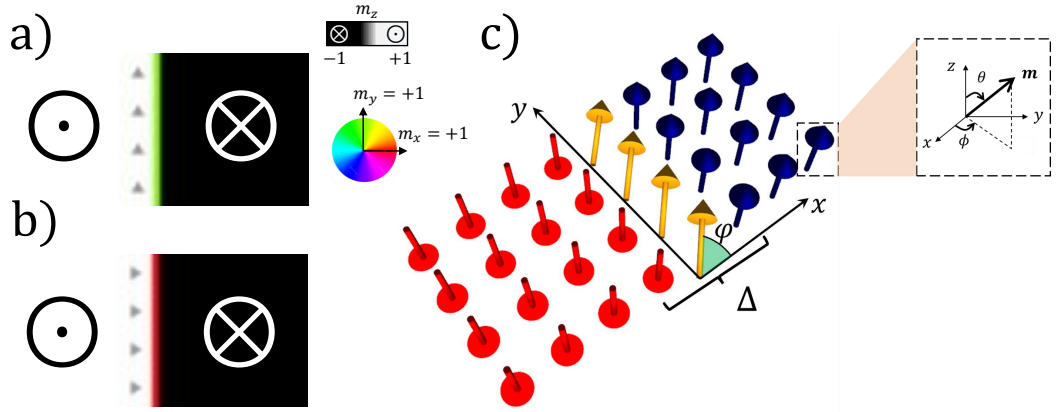

Fig. 2.7.: Micromagnetic snapshot of: a) Bloch DW structure, b) Néel DW structure. c) Schematic representation of the DW parameters within the one-dimensional (1D) approach used in this section. Δ is the DW width, φ is the internal DW angle, θ is the polar magnetization angle and ϕ is its azimuthal angle.

where $Q = \pm 1$ is a parameter that defines the DW configuration, $Q = +1(-1)$ for up-down(down-up) configuration starting from the left to the right of the ferromagnetic strip along x-axis. Then we express the full micromagnetic energy per unit volume, including DMI (see Eq. (2.22)) using the spherical coordinate of the magnetization (see Appendix. A.1 for further details)

$$\mathcal{E} = A_{\text{ex}} \left[\left(\frac{\partial \theta}{\partial x} \right)^2 + \sin^2\theta \left(\frac{\partial \phi}{\partial x} \right)^2 \right] + K_{\text{eff}} \sin^2\theta + K_{\text{sh}} \sin^2\theta \sin^2\phi + D \left[\cos\phi \frac{\partial \theta}{\partial x} + \sin\theta \cos\theta \left(\sin\phi \frac{\partial \phi}{\partial x} \right) \right] \quad (2.46)$$

where $K_{\text{eff}} = K_{\text{u}} - \frac{1}{2}\mu_0 M_{\text{s}}^2 N_z$ and $K_{\text{sh}} = \frac{1}{2}\mu_0 M_{\text{s}}^2 (N_y - N_x)$ with N_x, N_y, and N_z being the demagnetizing factors (see Eq. (2.21)), whose detailed expressions can be found in [61].

Using Eq. (2.45a) and Eq. (2.45b), and integrating the energy density Eq. (2.46) along x-axis yields the DW energy per unit surface

$$\mathcal{U}_{\text{DW}} = \int_{-\infty}^{+\infty} \mathcal{E} \mathrm{d}x = \frac{2A_{\text{ex}}}{\Delta} + 2\Delta(K_{\text{eff}} + K_{\text{sh}} \sin^2\varphi) + \pi Q D \cos\varphi \quad (2.47)$$

The DW surface energy depends on both Δ and φ. Minimizing Eq. (2.47) with respect to them yields

$$0 = \frac{\partial \mathcal{U}_{\mathrm{DW}}}{\partial \varphi} = 2\Delta K_{\mathrm{sh}} \sin 2\varphi - \pi Q D \sin \varphi \tag{2.48a}$$

$$0 = \frac{\partial \mathcal{U}_{\mathrm{DW}}}{\partial \Delta} = -\frac{2A_{\mathrm{ex}}}{\Delta} + 2K_{\mathrm{sh}} \sin^2 \varphi \tag{2.48b}$$

Solving Eq. (2.48a) and Eq. (2.48b), we obtain the expression for φ and Δ at equilibrium. These expressions allows us to gain insight into the factors that determine the specific type of DW configuration (i.e. Bloch or Néel) and its width.

The DW internal angle at equilibrium reads

$$\varphi_0 = \begin{cases} 0 & |\pi D| > |4\Delta K_{\mathrm{sh}}|, QD > 0 \\ \pi & |\pi D| > |4\Delta K_{\mathrm{sh}}|, QD < 0 \\ \cos^{-1}\left[\frac{\pi Q D}{4\Delta K_{\mathrm{sh}}}\right] & |\pi D| < |4\Delta K_{\mathrm{sh}}| \end{cases} \tag{2.49}$$

which shows that DMI favours a pure Néel DW structure if it is dominant in the system.

Eq. (2.49) shows explicitly that the competition between shape anisotropy and DMI defines the type of stabilized DWs. Let us suppose that $K_{\mathrm{sh}} \gg D$, then the argument in the $\cos^{-1}$ tends to zero, leading to $\varphi_0 = \frac{\pi}{2}$, which represents a pure Bloch DW structure. A mixed DW configuration is also possible when both shape anisotropy and DMI are comparable. In Fig. 2.8, we present micromagnetic simulations results plotted together with the 1D model prediction (Eq. (2.49)) for the equilibrium DW angle versus the iDMI constant. It can be observed that the 1D model provides a good prediction for the DW type at equilibrium, as it shows a good quantitative agreement with the simulation results.

From Eq. (2.48b) the DW width in equilibrium is found as

$$\Delta_0 = \sqrt{\frac{A_{\mathrm{ex}}}{K_{\mathrm{eff}} + K_{\mathrm{sh}} \sin^2 \varphi_0}} \tag{2.50}$$

It is worth highlighting that, in the case of of thin FM layers with strong PMA ($K_{\mathrm{eff}} \gg K_{\mathrm{sh}}$), the DW width at rest reduces to $\Delta_0 \approx \sqrt{\frac{A_{\mathrm{ex}}}{K_{\mathrm{eff}}}}$.

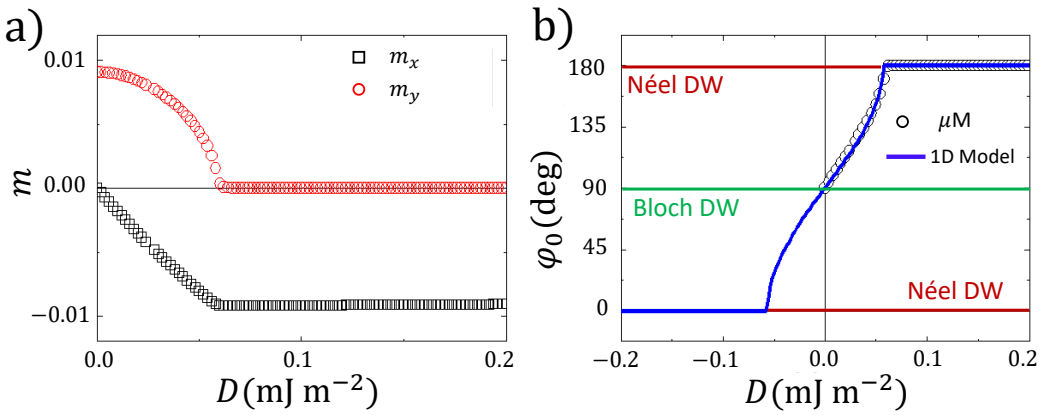

Fig. 2.8.: a) Equilibrium DW in-plane magnetization components versus DMI constant D computed from μM simulations. b) DW equilibrium internal angle φ_0 versus DMI constant D computed from both 1D model (Eq. (2.49)) and μM simulations. Adapted from [103].

Field-driven magnetic DW dynamics within the 1D-model

As previously explained in Sec. 2.3.4, under the effect of a magnetic field, the magnetization of the ferromagnet tends to align parallel to the direction of the applied field. Thus, when a DW is present, the domain that aligns parallel to the external field expands, while the antiparallel domain contracts, as shown in Fig. 2.9. This dynamic interplay leads to the translation of the DW along the length of the ferromagnetic strip. Let us now focus on understanding the field-driven DW dynamics using the 1D model. To do so, we add Zeeman energy to Eq. (2.46) accounting for a field applied along the z-axis and integrate it along the x-axis, which gives the DW surface energy density as

$$\mathcal{U}_{\mathrm{DW}} = \frac{2A_{\mathrm{ex}}}{\Delta} + 2\Delta(K_{\mathrm{eff}} + K_{\mathrm{sh}}\sin^2\varphi) + \pi Q D\cos\varphi - 2Q\mu_0 M_{\mathrm{s}} q H_{\mathrm{ext}} \tag{2.51}$$

The differential of the the DW surface energy density can be expressed in terms of q, φ, and Δ as

$$d\mathcal{U}_{\mathrm{DW}} = \frac{\partial \mathcal{U}_{\mathrm{DW}}}{\partial q}\mathrm{d}q + \frac{\partial \mathcal{U}_{\mathrm{DW}}}{\partial \varphi}\mathrm{d}\varphi + \frac{\partial \mathcal{U}_{\mathrm{DW}}}{\partial \Delta}\mathrm{d}\Delta \tag{2.52}$$

and

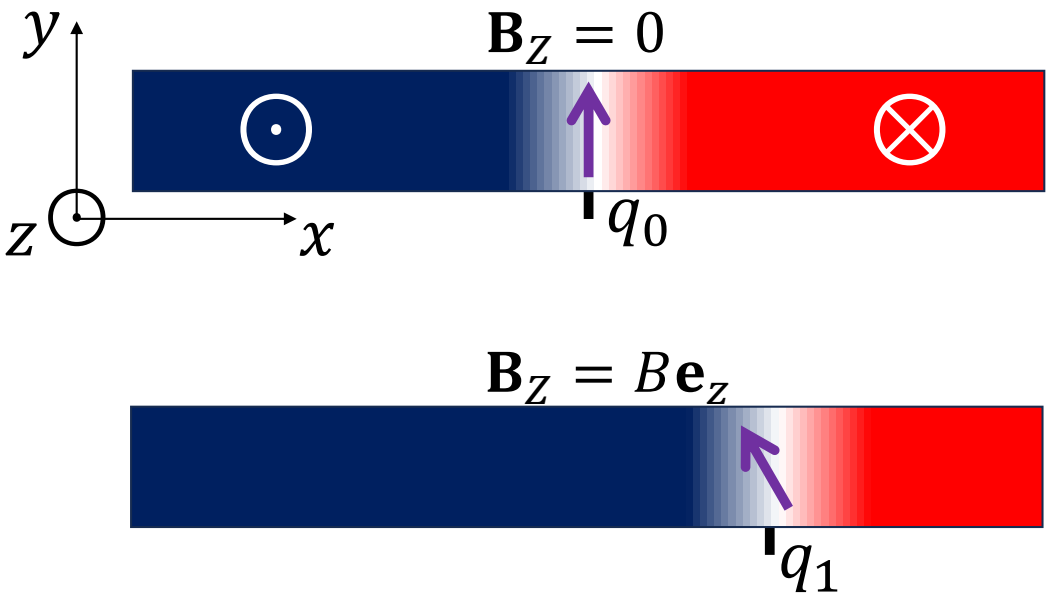

Fig. 2.9.: Schematic representation of the DW behaviour under externally applied field along $+z$ directions indicating the initial DW position q_0 and its position q_1 after applying the field.

$$\frac{\partial \mathcal{U}_{\mathrm{DW}}}{\partial q} = -2Q\mu_0 M_{\mathrm{s}} H_{\mathrm{ext}}$$
$$\frac{\partial \mathcal{U}_{\mathrm{DW}}}{\partial \varphi} = 2\Delta K_{\mathrm{sh}} \sin 2\varphi - \pi Q D \sin\varphi$$
$$\frac{\partial \mathcal{U}_{\mathrm{DW}}}{\partial \Delta} = -\frac{2A_{\mathrm{ex}}}{\Delta^2} + 2\left(K_{\mathrm{eff}} + K_{\mathrm{sh}} \sin^2\varphi\right)$$

Expressing Eq. (2.41) in spherical coordinates we obtain

$$\frac{\delta \mathcal{E}}{\delta \phi} = -\frac{\mu_0 M_{\mathrm{s}} \sin\theta}{\gamma_0}\left(\dot{\theta} + \alpha \sin\theta\, \dot{\phi}\right) \tag{2.54a}$$
$$\frac{\delta \mathcal{E}}{\delta \theta} = \frac{\mu_0 M_{\mathrm{s}}}{\gamma_0}\left(\sin\theta\, \dot{\phi} - \alpha\, \dot{\theta}\right) \tag{2.54b}$$

where we used $\mathrm{d}\mathbf{m} = \mathrm{d}\theta\, \mathbf{e}_\theta + \sin\theta \mathrm{d}\varphi\, \mathbf{e}_\varphi$ and $\mathbf{H}_{\mathrm{eff}} = -\frac{1}{\mu_0 M_{\mathrm{s}}}\frac{\delta \mathcal{E}}{\delta \theta}\, \mathbf{e}_\theta - \frac{1}{\mu_0 M_{\mathrm{s}} \sin\theta}\frac{\delta \mathcal{E}}{\delta \varphi}\, \mathbf{e}_\varphi$.

Therefore, the variation of the micromagnetic energy density can be expressed as

$$\delta\mathcal{E} = \frac{\delta\mathcal{E}}{\delta\theta}\delta\theta + \frac{\delta\mathcal{E}}{\delta\phi}\delta\phi = \frac{\mu_0 M_\mathrm{s}}{\gamma_0}\left(\sin\theta\,\dot{\phi} - \alpha\,\dot{\theta}\right)\delta\theta - \frac{\mu_0 M_\mathrm{s}\sin\theta}{\gamma_0}\left(\dot{\theta} + \alpha\sin\theta\,\dot{\phi}\right)\delta\phi \tag{2.55}$$

Integrating Eq. (2.55) along x we get an expression for $\mathrm{d}\mathcal{U}_\mathrm{DW}$ from LLG, which reads (see Appendix. A.1 for further details)

$$\mathrm{d}\mathcal{U}_\mathrm{DW} = \int_{-\infty}^{+\infty}\delta\mathcal{E}\;\mathrm{d}x = -\frac{2\mu_0 M_\mathrm{s}}{\gamma_0}\left[\left(\alpha\frac{\dot{q}}{\Delta} + Q\dot{\varphi}\right)\mathrm{d}q + (Q\dot{q} - \alpha\Delta\dot{\varphi})\,\mathrm{d}\varphi + \left(\alpha\frac{\pi^2}{12}\frac{\dot{\Delta}}{\Delta}\right)\mathrm{d}\Delta\right] \tag{2.56}$$

By comparing Eq. (2.51) with Eq. (2.56) we obtain the coupled equations describing the DW dynamics in presence of a perpendicular external magnetic field as

$$(1+\alpha^2)\frac{\dot{q}}{\Delta} = -\alpha\,\Gamma_\mathrm{A} + Q\Gamma_\mathrm{B} \tag{2.57a}$$

$$(1+\alpha^2)\dot{\varphi} = -Q\Gamma_\mathrm{A} - \alpha\Gamma_\mathrm{B} \tag{2.57b}$$

$$\dot{\Delta} = \frac{12\gamma_0}{\alpha\mu_0 M_\mathrm{s}\pi^2}\left[\frac{A_\mathrm{ex}}{\Delta} - \Delta\left(K_\mathrm{eff} + K_\mathrm{sh}\sin^2\varphi\right)\right] \tag{2.57c}$$

where

$$\Gamma_\mathrm{A} = -\gamma_0 Q H_\mathrm{ext}$$
$$\Gamma_\mathrm{B} = \gamma_0\frac{H_\mathrm{sh}}{2}\sin 2\varphi - \gamma_0\frac{\pi}{2}QH_\mathrm{DMI}\sin\varphi$$

with $H_\mathrm{sh} = M_\mathrm{s}(N_y - N_x)$ and $H_\mathrm{DMI} = \frac{D}{\mu_0 M_\mathrm{s}\Delta}$. Eq. (2.57a), Eq. (2.57b) and Eq. (2.57c), describe the time evolution of the DW position, the DW internal angle, and the DW width, respectively.

Eqs. (2.57a) and (2.57b) shed light on the complexity of DW dynamics under the influence of a magnetic field, extending beyond simple translation as discussed earlier in this section. In fact, additionally to the translational motion described by Eq. (2.57a), the DW also undergoes a rotational dynamics associated with its internal magnetic moment, described by Eq. (2.57b). When an external magnetic field is applied, it contributes two distinct torques to the DW. The first torque, known

as the damping field torque ($\alpha\Gamma_{\mathrm{A}}$), triggers the translational motion of the DW along the x-axis. The second one, referred to as the precessional field torque ($Q\Gamma_{\mathrm{A}}$), induces rotational motion of the DW internal magnetic moment around the z-axis. In addition to the torques due to the external field, other torques from shape anisotropy and DMI also come into play. Consequently, the DW dynamics is governed by the interplay of these toques as sketched in Fig. 2.10(a). This interplay gives different regimes, which will be explored and explained in the following.

As shown in Eq. (2.57b), the torques involved in the dynamics of φ are the field precessional torque $Q\Gamma_{\mathrm{A}}$, the DMI damping torque $\alpha\Gamma_{\mathrm{DMI}} = \alpha\gamma_0\frac{\pi}{2}QH_{\mathrm{DMI}}\sin\varphi$ and the shape anisotropy damping torque $\alpha\Gamma_{\mathrm{sh}} = \alpha\gamma_0\frac{H_{\mathrm{sh}}}{2}\sin 2\varphi$. In the case of negligible DMI, an applied magnetic field tilts the internal DW angle away from its equilibrium orientation (Bloch, $\varphi = \pm\frac{\pi}{2}$) via the precessional torque ($Q\Gamma_{\mathrm{A}}$). This tilting of φ activates the damping torque due to the shape anisotropy, which tries to bring φ back to its equilibrium value. As long as the applied field is below a certain threshold, the DW angle φ reaches a terminal value and eventually $\alpha\Gamma_{\mathrm{sh}}$ balances $Q\Gamma_{\mathrm{A}}$ leading to the DW moving with a constant velocity along the x-axis as illustrated in Fig. 2.10(b). Increasing the external magnetic field strength further ($|Q\Gamma_{\mathrm{A}}| > \alpha|\Gamma_{\mathrm{sh}}|$) leads the DW internal angle to rotate continuously, which initiates an oscillatory motion of the DW as shown in Fig. 2.10(b). This oscillatory dynamics of the DW is called Walker regime and was described theoretically by Walker in 1974 [101]. The threshold field at which the DW transits to the oscillatory behavior is the so-called Walker field H_{W}.

In presence of DMI, similar dynamics takes place with the peculiarity that the DW at equilibrium is Néel $\varphi = 0(\pi)$, and the damping torque is the DMI one ($\alpha\Gamma_{\mathrm{DMI}}$). The DW internal angle dynamics in this case relies on the interplay between the $Q\Gamma_{\mathrm{A}}$ and $\alpha\Gamma_{\mathrm{DMI}}$. As long as these torques can balance each other, the DW moves rigidly with a constant velocity. Above the Walker field, oscillatory DW motion takes place as explained in the preceding paragraph.

To quantify the field around which the DW dynamics transits from steady to oscillatory dynamics (Walker field), we need to explore the steady state from Eqs. (2.57a) and (2.57b). In fact, the steady state is reached when $\lim_{t\to+\infty}\dot{\varphi} = 0$. Using this condition, we can calculate the DW angle at the steady state for two cases.

First, for negligible DMI (Bloch DWs are favored), the DW angle in the steady regime reads

$$\varphi_{\mathrm{s}} = \frac{1}{2}\sin^{-1}\left(\frac{2H_{\mathrm{ext}}}{\alpha H_{\mathrm{sh}}}\right) \tag{2.59}$$

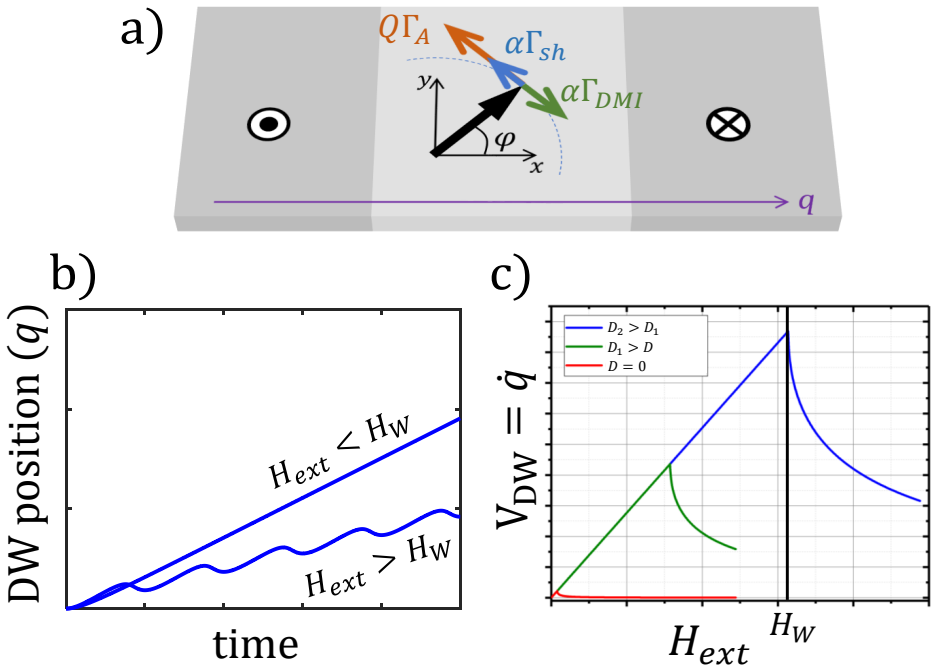

Fig. 2.10.: a) Schematic representation of different torque contributions on DW dynamics. b) Temporal evolution of the DW motion for $H_{\mathrm{ext}} < H_{\mathrm{W}}$ and $H_{\mathrm{ext}} > H_{\mathrm{W}}$ from the 1D model. c) DW velocity versus applied magnetic field for different values of iDMI constant (D).

where Walker field could be determined from this equation as $H_{\mathrm{W}} = \left|\frac{\alpha H_{\mathrm{sh}}}{2}\right|$. Hence, if $H_{\mathrm{ext}} < H_{\mathrm{W}}$ the DW moves rigidly with a constant velocity given by

$$v_{\mathrm{s}} = \frac{\Delta\gamma_0 Q H_{\mathrm{ext}}}{\alpha} \tag{2.60}$$

If DMI is dominant ($H_{\mathrm{DMI}} \gg \frac{H_{\mathrm{sh}}}{2}$), the DW angle in the steady state reads

$$\varphi_{\mathrm{s}} = \sin^{-1}\left[\frac{2H_{\mathrm{ext}}}{\alpha Q \pi H_{\mathrm{DMI}}}\right] \tag{2.61}$$

and the Walker field in this case is $H_{\mathrm{W}} = \left|\frac{\pi}{2}\alpha Q H_{\mathrm{DMI}}\right|$.

The presence of DMI allows for larger DW velocities due to the increase in the Walker field. By examining Eq. (2.59) and Eq. (2.61), we can observe that in the absence of DMI oscillatory motion occurs when $\varphi_{\mathrm{s}} = \pm\frac{\pi}{4}$, whereas if DMI is present, this happens when $\varphi_{\mathrm{s}} = \pm\frac{\pi}{2}$. The presence of DMI allows for reaching higher magnetic fields before the velocity breakdown. This ultimately leads to larger DW velocities, as illustrated in Fig. 2.10(c).

SOTs driven magnetic DW dynamics

External magnetic fields have traditionally been considered the primary means for driving DW dynamics in ferromagnets. However, from an application standpoint, they are not well-suited since adjacent DWs are driven towards each other and eventually are annihilated. This is a limitation to driving several DWs along ferromagnetic racetracks. In contrast, electric currents offer a more favorable approach as they drive magnetic DWs in the same direction. This opens up possibilities for moving trains of DWs collectively, which is advantageous for applications involving data transport [104–106].

Now, let us focus on the case of SOT-driven DWs, where the spin current is injected into the ferromagnet through the spin-Hall effect (see Fig. 2.6). To incorporate the effect of SOTs we add the torque expression in Eq.(2.43) to the LLG equation as shown in Sec. 2.6. Following the same integration method used for field-driven DW dynamics (see Appendix. A.1), we can derive the dynamic equations governing the motion of DWs under SOTs. These dynamic equations can be expressed as

$$(1+\alpha^2)\frac{\dot{q}}{\Delta} = -\alpha\,\Gamma_{\mathrm{A}} + Q\Gamma_{\mathrm{B}} \tag{2.62a}$$

$$(1+\alpha^2)\dot{\varphi} = -Q\Gamma_{\mathrm{A}} - \alpha\Gamma_{\mathrm{B}} \tag{2.62b}$$

where now

$$\Gamma_{\mathrm{A}} = Q\gamma_0\frac{\pi}{2}H_{\mathrm{SOT}}\cos\varphi$$

$$\Gamma_{\mathrm{B}} = \gamma_0\frac{H_{\mathrm{sh}}}{2}\sin 2\varphi - \gamma_0\frac{\pi}{2}QH_{\mathrm{DMI}}\sin\varphi$$

with $H_{\mathrm{SOT}} = \frac{\hbar\theta_{\mathrm{sh}}\mathrm{J}_{\mathrm{HM}}}{2|e|\mu_0 M_{\mathrm{s}} t_{\mathrm{FM}}}$ is a constant linked to the SOT field magnitude.

The peculiarity of SOT-driven DW dynamics is manifested in the dependency of both the precessional and the damping torques on the DW internal angle as $\Gamma_{\mathrm{A}} \propto \cos\varphi$. This leads to a cancellation of SOT if $\cos\varphi \approx 0$, which explains why Bloch DWs are insensitive it [107].

Considering that iDMI is strong enough $H_{\mathrm{DMI}} \gg \frac{H_{\mathrm{sh}}}{2}$, the DW angle at the steady state reads

$$\varphi_{\mathrm{s}} = \tan^{-1}\left[\frac{QH_{\mathrm{SOT}}}{\alpha H_{\mathrm{DMI}}}\right] \tag{2.64}$$

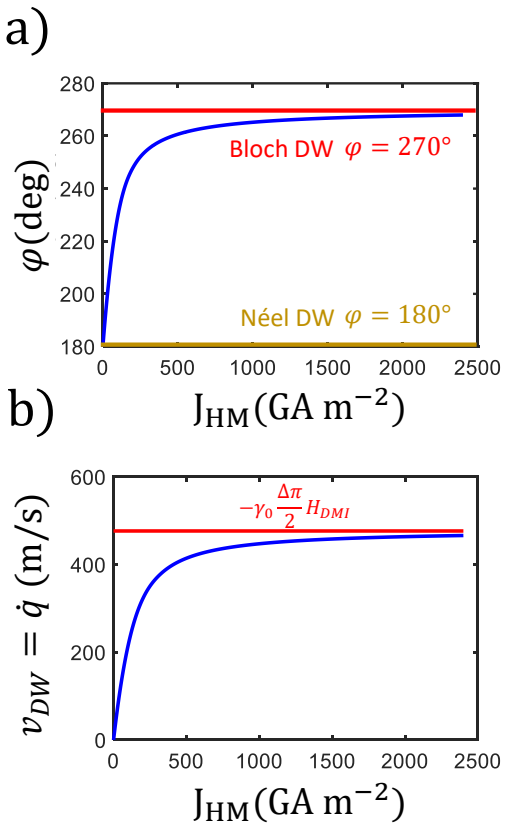

Fig. 2.11.: a) DW angle φ versus applied electric current for an SOT-driven DW. b) Terminal velocity versus applied electric current for an SOT-driven DW, the figure shows also the limiting velocity of the system calculated from Eq. (2.66). The material parameters used are: $M_\mathrm{s} = 0.58\,\mathrm{MA\,m^{-1}}$, $A_\mathrm{ex} = 20\,\mathrm{pJ\,m^{-1}}$, $K_\mathrm{u} = 0.9\,\mathrm{MJ\,m^{-3}}$, $D = 1\,\mathrm{mJ\,m^{-2}}$, $\alpha = 0.08$, and $t_\mathrm{FM} = 1\,\mathrm{nm}$.

Then, the DW velocity in the steady state can be expressed as

$$v_\mathrm{s} = -\frac{\Delta\pi\gamma_0 Q H_\mathrm{SOT}}{2\alpha}\cos\varphi = -\frac{\Delta\pi\gamma_0 Q H_\mathrm{SOT}}{2\alpha}\frac{1}{\sqrt{\left(\frac{Q H_\mathrm{SOT}}{\alpha H_\mathrm{DMI}}\right)^2 + 1}} \tag{2.65}$$

Eq. (2.64) shows that increasing the SOT current continuously leads the DW angle asymptotically to $\pm\frac{\pi}{2}$, which makes SOT less efficient as shown in Fig. 2.11(a). The DW velocity then saturates and its value at saturation depends only on DMI field as

$$v_\mathrm{s} = -\gamma_0\frac{\Delta\pi}{2}H_\mathrm{DMI} \tag{2.66}$$

Note that the DW velocity relies on both spin Hall angle and DMI constant. A detailed discussion about SOT driven DW dynamics could be found in [103].

2.8.2 Magnetic skyrmions

Similarly to magnetic DWs, skyrmions, come in two main types: Bloch and Néel. Bloch skyrmions (shown in Fig. 2.12(a)), mainly form in bulk ferromagnetic materials with a B20 crystal structures. They result from a combined action of dipolar and exchange interactions, along with bulk DMI [25]. Néel skyrmions, are typically observed in thin film multilayers and primarily emerge due to the interface Dzyaloshinskii-Moriya interaction [108]. Néel skyrmions feature a distinct chiral profile and a spin configuration reminiscent of a hedgehog-like structure as shown in Fig. 2.12(b).

From a topological point of view, skyrmions have a non-vanishing topological charge, which is given as [109]

$$Q_{\mathrm{sk}} = \frac{1}{4\pi} \iint \mathbf{m} \cdot \left(\frac{\partial \mathbf{m}}{\partial x} \times \frac{\partial \mathbf{m}}{\partial y} \right) \mathrm{d}x\mathrm{d}y \tag{2.67}$$

To evaluate Q_{sk} it is better to express Eq. (2.67) in polar coordinates, which reads

$$Q_{\mathrm{sk}} = \frac{1}{4\pi} \int_0^{\infty} \int_0^{2\pi} \sin\theta(\rho) \left(\frac{\partial \theta(\rho)}{\partial \rho} \frac{\partial \phi(\Phi)}{\partial \Phi} \right) \mathrm{d}\Phi\mathrm{d}\rho = -\frac{1}{4\pi} \left[\cos\theta(\rho)\right]_0^{\infty} \left[\phi(\Phi)\right]_0^{2\pi} = p\mathcal{W} \tag{2.68}$$

where p is the skyrmion polarity and $\mathcal{W}$ is the winding number.

The orientation of the skyrmion core defines its polarity p: a skyrmion core oriented along $+z(-z)$ yields $p = +1(-1)$. The winding number $\mathcal{W}$ is related to the angle by which the magnetization rotates when completing a full 2π rotation around the skyrmion core. A skyrmion possesses a winding number $\mathcal{W} = 1$, while an antiskyrmion is characterized by $\mathcal{W} = -1$, which represents the antiparticle of a skyrmion in the standard model [110]. Hence, the topological charge of a skyrmion is quantified and solely determined by its core polarity: $Q_{\mathrm{sk}} = p = \pm 1$ ($Q_{\mathrm{sk}} = \mp 1$ for an antiskyrmion). Due to its unique topology, a skyrmion (or an antiskyrmion) cannot be easily unwound through continuous transformations. This implies that transitioning from a skyrmion state to a uniform ferromagnetic state with $Q_{\mathrm{sk}} = 0$ requires overcoming a large energy barrier. This property of magnetic skyrmions is

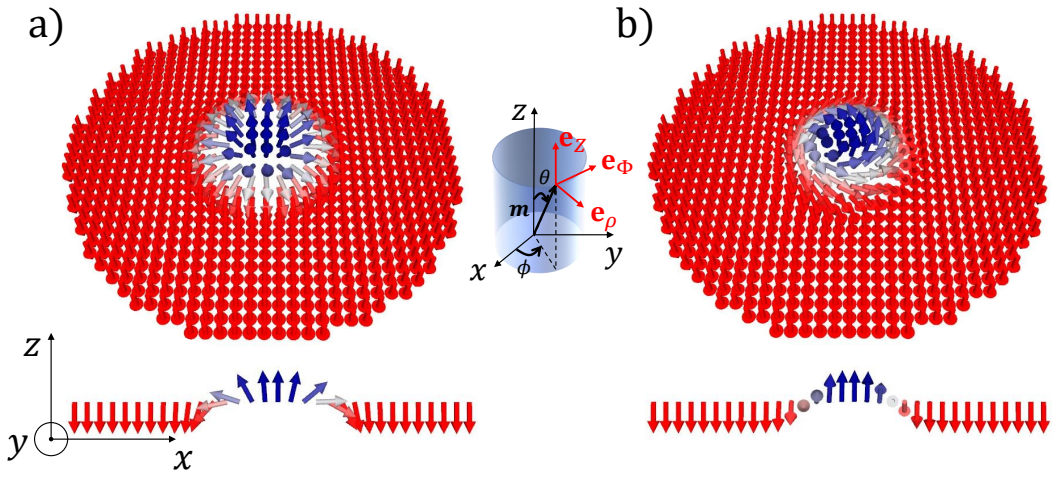

Fig. 2.12.: a) Representation of a Néel magnetic skyrmion. The type of the DW in such a skyrmion is Néel as can be seen in the bottom of the figure where we represent the magnetization transition in a string a long the skyrmion diameter. b) Representation of a Bloch magnetic skyrmion. The type of the DW in such a skyrmion is Bloch as can be seen in the bottom of the figure. The inset of the figure shows the definition of the coordinates base that we will adopt for our skyrmion chapter. The inset illustrates the spherical base first $(|\mathbf{m}|, \phi, \theta)$ and the cylindrical base with (ρ, Φ, Z).

referred to as topological protection. However, it is noteworthy to mention that this description holds for vector fields in the continuum limit. In real magnetic systems, however, a skyrmion doesn't exhibit this topological protection due to the fact that the spins are discrete objects.

Magnetic skyrmion dynamics

As mentioned previously in this section, skyrmions are highly stable topological structures. Within the micromagnetic continuum approximation, it has been shown that the energy required for skyrmions destruction diverges [111, 112]. On the other hand, experimental studies showed that skyrmions are very stable at room temperature [108]. Furthermore, they are less sensitive to deformations, unless under extreme conditions where their annihilation could take place [113, 114]. This features legitimate the treatment of magnetic skyrmion as rigid quasi-particle structures [115–118]. On the other hand, in presence of external forces that tend to drive them in a certain direction, skyrmions exhibit a deflection orthogonal to the force. This effect was labeled as the skyrmion Hall effect (SkHe) [119]. In this section, we will use Thiele's model to explore the physical mechanism behind

the skyrmion deflection. This model assumes the skyrmion as a moving point-like quasi-particle, neglecting its internal degrees of freedom [115].

The dynamic equation describing magnetic skyrmion motion within Thiele's model framework reads (see Appendix. A.2 for detailed derivation)

$$\mathbf{G} \times \mathbf{v} - \alpha \bar{\bar{\mathcal{D}}} \cdot \mathbf{v} = \mathbf{F}_{\mathrm{ext}} \tag{2.69}$$

where $\mathbf{G} = |\mathbf{G}|\mathbf{e}_z$ with

$$|\mathbf{G}| = -\frac{\mu_0 M_{\mathrm{s}} t_{\mathrm{FM}}}{\gamma_0} \iint \mathbf{m} \cdot \left(\frac{\partial \mathbf{m}}{\partial x} \times \frac{\partial \mathbf{m}}{\partial y} \right) \mathrm{d}x\mathrm{d}y \tag{2.70}$$

being the gyrovector, which reads $|\mathbf{G}| = \frac{-\mu_0 M_{\mathrm{s}} t_{\mathrm{FM}}}{\gamma_0} Q_{\mathrm{sk}}$ for any arbitrary magnetic texture that has a non-vanishing topological charge Q_{sk} [115]. The second-rank tensor $\bar{\bar{\mathcal{D}}}$ is the so-called dissipation tensor, whose components are

$$\mathcal{D}_{ij} = \frac{\mu_0 M_{\mathrm{s}} t_{\mathrm{FM}}}{\gamma_0} \iint \left(\frac{\partial \mathbf{m}}{\partial x_i} \cdot \frac{\partial \mathbf{m}}{\partial x_j} \right) \mathrm{d}x\mathrm{d}y \tag{2.71}$$

$\mathbf{F}_{\mathrm{ext}}$ is the external force applied to the skyrmion and $\mathbf{v}$ is the skyrmion velocity.

The Eq. (2.69) is the general form for Thiele's equation describing the motion of a magnetic texture under the effect of an arbitrary external force. This equation was widely used to investigate the dynamics of several exotic magnetic structures such as skyrmion, vortices, skyrmioniums, bimerons, ... [120–122]. The two terms in the rhs of Eq. (2.69) describe the rotation of the skyrmion around its own axis and the friction effects on the skyrmion upon its motion, respectively. Hence, if the skyrmion moves in an arbitrary direction due to the external force $\mathbf{F}_{\mathrm{ext}}$, it will experience a force due to the gyrovector $\mathbf{G}$ that tends to make it move orthogonal to the force direction. Then, the dissipative term $\alpha \bar{\bar{\mathcal{D}}} \cdot \mathbf{v}$ counteracts the gyrotropic term, pushing the skyrmion to move along a tilted path with a given angle θ_{SkHE} as schematized in Fig. 2.13.

To provide a quantitative description based on the preceding analysis, we can perform algebraic manipulation of Eq. (2.69) for deriving expressions for the skyrmion velocity. Let us examine a specific skyrmion configuration under the assumption that: $\mathbf{G} = |\mathbf{G}|\,\mathbf{e}_z$, $\bar{\bar{\mathcal{D}}} = \begin{pmatrix} \mathcal{D}_{xx} & \mathcal{D}_{xy} \\ \mathcal{D}_{yx} & \mathcal{D}_{yy} \end{pmatrix}$; with $\mathcal{D}_{xx} = \mathcal{D}_{yy} = |\mathcal{D}|$ and $\mathcal{D}_{xy} = \mathcal{D}_{yx} = 0$; and $\mathbf{F} = F_x \mathbf{e}_x$. The skyrmion velocity components in this case read

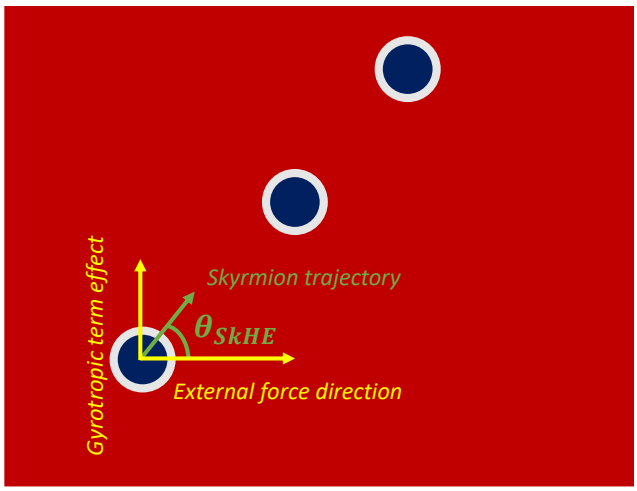

Fig. 2.13.: Schematic representation of the skyrmion motion mechanism. Under an external applied force the skyrmion tends to follow a tilted path with a given angle θ_{SkHE}.

$$v_x = \frac{\mathrm{d}X}{\mathrm{d}t} = \frac{\alpha \left|\mathcal{D}\right| F_x}{\alpha^2 \left|\mathcal{D}\right|^2 + \left|\mathbf{G}\right|^2} \tag{2.72a}$$

$$v_y = \frac{\mathrm{d}Y}{\mathrm{d}t} = \frac{\left|\mathbf{G}\right| F_x}{\alpha^2 \left|\mathcal{D}\right|^2 + \left|\mathbf{G}\right|^2} \tag{2.72b}$$

where X, Y are the generalized skyrmion coordinates.

The skyrmion Hall angle reads

$$\theta_{\mathrm{SkHE}} = \tan^{-1}\left(\frac{v_y}{v_x}\right) = \frac{\left|\mathbf{G}\right|}{\alpha|\mathcal{D}|} \tag{2.73}$$

The velocity formulas Eq. (2.72a) and Eq. (2.72b), reveal that the skyrmion deflection is an intrinsic feature and does not depend on the external force. It emerges from the gyrotropic nature of magnetization dynamics and the topological characteristics ingrained within the skyrmion structure. Moreover, Thiele's model offers insights into the dynamic translation of skyrmions, illustrating that it is driven by energy dissipation within the system, akin to the motion of magnetic domain walls. In Figure 2.14, we present micromagnetic simulation results alongside experimental Kerr microscopy images from [123], illustrating the motion of skyrmions in FM/HM layers under the influence of SOT. Consistent with the description of skyrmion dynamics provided by the Thiele model, skyrmions under the influence of SOT tend to follow a tilted trajectory, exhibiting the skyrmion Hall effect. This phenomenon has been confirmed through both simulation and experiments [119, 123, 124].

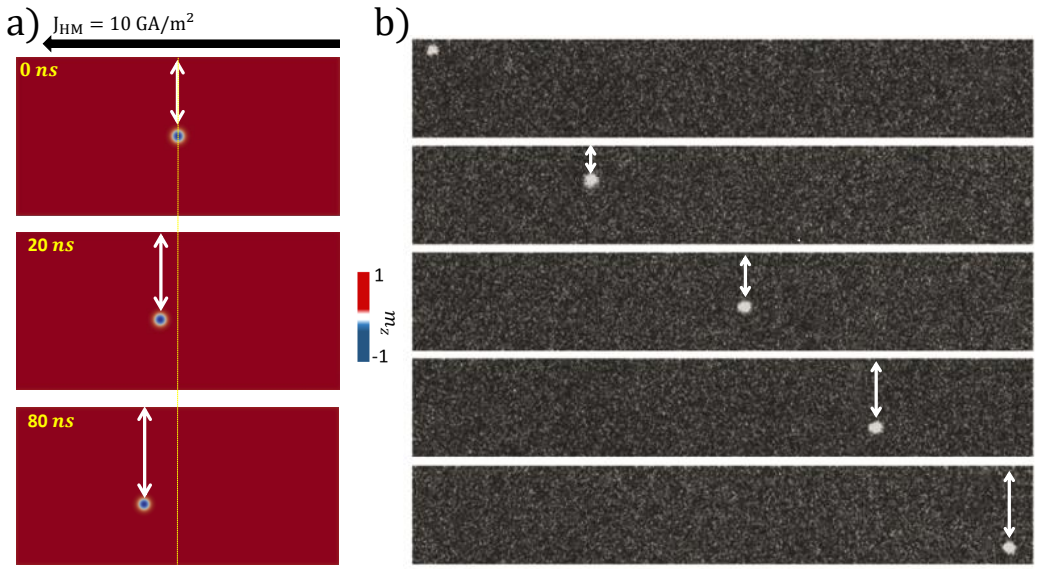

Fig. 2.14.: a) Micromagnetic snapshots of the skyrmion motion under spin-orbit torques. b) Kerr microscopy images for a skyrmion moving under electric current from the work by Fert et al [123].

2.9 Conclusion

Within this chapter we presented the theoretical background required for our research. We delved into the micromagnetic theory, which offers a framework for studying magnetic systems by considering continuous magnetization vector fields rather than individual magnetic moments. Subsequently, we explored the diverse contributions to the overall micromagnetic energy originating from various interactions. After that, we investigated the minimization of this energy as well as the boundary conditions resulting from different contributions. Furthermore, we discussed magnetization dynamics and introduced the Landau-Lifshitz-Gilbert equation augmented with the spin-orbit torque. This chapter has also examined both the static and dynamic properties of DWs and skyrmions from the perspective of micromagnetic theory. This theoretical framework will serve as the cornerstone for the subsequent modeling and analytical investigations discussed within this thesis.

3 Electric field control of current-driven skyrmion dynamics

In this chapter, we propose a method to control the trajectory of current-driven skyrmions using electric fields in hybrid piezoelectric/magnetic systems. By applying a voltage between two lateral electrodes, a transverse strain gradient is created as a result of the non-uniform electric field profile in the piezoelectric. Due to magnetoelastic coupling, this transverse gradient leads to a lateral force on the skyrmions that can be used to suppress the skyrmion Hall angle for any given current density if a proper voltage is applied. We show that this method works under realistic conditions, such as the presence of disorder in the ferromagnet, and that skyrmion trajectories can be controlled with moderate voltages. Moreover, our method allows for increasing the maximum current density that can be injected before the skyrmion is annihilated at the nanostrip edge, which leads to an increase in the maximum achievable velocities. This chapter is an adapted version of the author's publication [125].

3.1 Introduction

Since their observation in 2009 [25], magnetic skyrmions have attracted a lot of attention, not only from the point of view of fundamental research but also because they present some features, such as small size, topological protection, or being sensitive to moderate current densities, that make them attractive for the development of the next generation of spintronic devices. In this sense, different skyrmion-based devices have been proposed, such as logic gates [14, 35–37], magnetic memories [40, 41], artificial neuron spikes [38, 39] or microwave detectors [126]. The potential success of these devices relies on our capacity for nucleating, stabilizing, and controlling the motion of skyrmions in an energy-efficient way.

Magnetic skyrmions can be moved using spin-polarized electrical currents [26], anisotropy gradients [127], strain gradients [128], surface acoustic waves [129],

magnetic field gradients [130], spin waves [131], temperature gradients [132], etc. Regardless of the nature of the driving force, the skyrmion trajectory is not parallel to the direction of this force but it deviates a certain angle from it, as explained in Sec. 2.8.2, a phenomenon usually referred to as the skyrmion Hall effect (SkHE) [118, 119, 124]. This universal phenomenon is due to the gyrotropic nature of magnetization dynamics, which leads to the appearance of a force on the skyrmion perpendicular to the driving one, the so-called Magnus force [133]. This is detrimental to the design of skyrmion-based devices, such as racetrack memories, where skyrmions are intended to follow a straight path along the nanostrip. Consequently, different approaches have been proposed to avoid it. For example, SkHE should not be present in antiferromagnets [134, 135] because the skyrmion's gyrovector cancels out but, as far as we are concerned, the nucleation of isolated skyrmions in antiferromagnets is still challenging. The SkHE is also absent in synthetic antiferromagnets [136] because the two interlayer-coupled skyrmions exhibit antiparallel Magnus forces that cancel each other, but, although isolated skyrmions have been stabilized in SAF [137], their controlled motion by electrical current or by any other means is still in a premature state [138]. Other more exotic textures, like magnetic Skyrmioniums, should also move without SkHE, since their topological charge is roughly zero [139, 140].

Tuning the skyrmion gyrovector is not the only way to suppress the SkHE. An alternative approach is based on inducing an external force to compensate the Magnus force. Different methods have been proposed along this line. In fact, in narrow strips, the skyrmion is repelled by the edges, and this repulsive transverse force is useful to maintain the skyrmion moving straight along the track [32]. On the other hand, it was shown that, by engineering Rashba and Dresselhaus spin-orbit couplings, it is possible to suppress the skyrmion Hall angle for both Neel skyrmions and Bloch antiskyrmions [34]. Heavy metal layers with reduced symmetry in chiral multilayers are also a route to minimize the skyrmion Hall angle and to maximize its speed via partial current polarization [33]. In any case, other methods providing more freedom and versatility to manipulate skyrmion motion are desirable to develop new technologies. In this chapter, we propose an approach for this purpose. It is based on a transverse voltage-induced mechanical excitation of a piezoelectric layer attached to the ferromagnetic nanostrip which, due to magnetoelastic coupling, creates a transverse force on the skyrmion that can be used to totally suppress the skyrmion Hall angle and to increase its velocity.

In the following, we present and discuss the results on which our proposal is based. We will first study the electromechanical response of our system and characterize the strain profile transferred to the ferromagnetic nanostrip along which the skyrmions

move. Secondly, we use both micromagnetic simulations and Thiele's model to show that this strain profile creates a transverse force on the skyrmion that can be used to correct its trajectory when driven by a current flowing parallel to the nanostrip. Moreover, we derive the condition to suppress the skyrmion Hall angle for any given value of the current density. In the last part, we show that our approach works under realistic conditions, such as the presence of disorder in the sample, and that it can be used to increase the maximum achievable skyrmion velocities.

3.2 Results and Discussions

3.2.1 Electro-mechanical characterization

The device proposed in our work is sketched in Fig. 3.1(a) where skyrmions move along a perpendicularly magnetized ferromagnetic racetrack driven by a current passing through an adjacent heavy metal. The HM/FM/Oxide trilayer is grown on top of a thick piezoelectric (PZ) film with two extended lateral electrodes on top of it, as shown in the Fig. 3.1(a). The basic idea of our proposal is that, due to magneto-elastic coupling, the strain created in the system when a voltage is applied between these two electrodes leads to a force on the skyrmions that can be used to control their lateral motion.

Electromechanical simulations were performed using COMSOL [141]. As piezoelectric material we used PZT-4 (Lead Zirconate Titanate) of dimensions $\ell_{\mathrm{PZ}} = 1200\ \mathrm{nm}, w_{\mathrm{PZ}} = 1000\ \mathrm{nm}$ and $t_{\mathrm{PZ}} = 100\ \mathrm{nm}$ (see Fig. 3.1(a)), whereas for the HM/FM/Oxide we considered $\mathrm{Pt}[2\ \mathrm{nm}]/\mathrm{CoFeB}[1\ \mathrm{nm}]/\mathrm{MgO}[1\ \mathrm{nm}]$ with lateral dimensions $\ell_{\mathrm{FM}} = 1024\ \mathrm{nm}, w_{\mathrm{FM}} = 500\ \mathrm{nm}$ and the following values for Young modulus and Poisson ratio: $\mathcal{Y}_{\mathrm{Pt}} = 154\,\mathrm{GPa}$, $\nu_{\mathrm{Pt}} = 0.385$ [142], $\mathcal{Y}_{\mathrm{CoFeB}} = 162\,\mathrm{GPa}$, $\nu_{\mathrm{CoFeB}} = 0.3$ [143], $\mathcal{Y}_{\mathrm{MgO}} = 270\,\mathrm{GPa}$ and $\nu_{\mathrm{MgO}} = 0.35$ [144]. When calculating the electromechanical response, we assume that the PZ bottom surface is clamped to the substrate, and we consider the conductive nature of both FM and HM layers. Fig. 3.1(b) shows the electric field lines in the PZ in the device cross section. As can be observed, the field lines leak into the HM layer due to its conductive nature, yielding a highly non-uniform field pattern. In particular, we note the profile of the out-of-plane component E_z along the PZ/HM interface in the transversal direction, which is plotted in Fig. 3.1(c) for an applied voltage of $10\ \mathrm{V}$ between the electrodes. As can be noticed, the field strength is maximum at the edges, but it points in opposite directions, and a gradual non-linear transition between these two extreme values is obtained as we move from one edge to the other. The profile along the

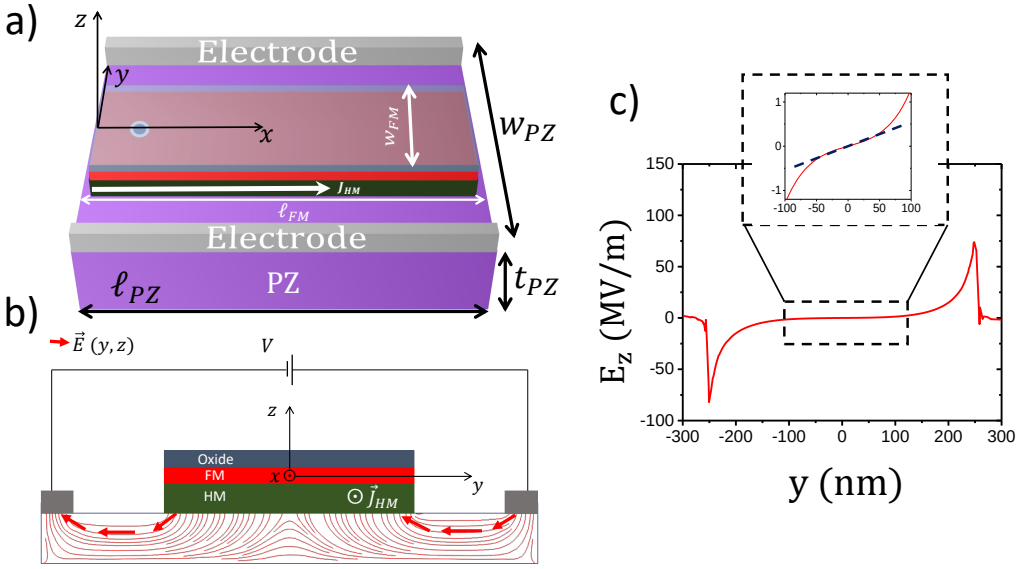

Fig. 3.1.: a) Schematic representation of the simulated device. (b) Device cross section showing the electric field lines in the PZ substrate. c) Profile of the vertical component E_z along the PZ/HM interface. The inset zooms out the profile in the central region of the nanostrip.

central region, shown in the inset of Fig. 3.1(c), is approximately linear with a slope $\frac{\mathrm{d}E_z}{\mathrm{d}y} \sim 10\ \mathrm{V}/\mu\mathrm{m}^2$.

The strain distribution in the device as a response of the PZ substrate to the electric field is also calculated with COMSOL [141]. In particular, Fig. 3.2(a) shows the profile of the strain component ε_{yy} transferred from the PZ to the FM for different widths of the PZ substrate. As can be observed, a smooth quasi-linear profile changing sign across the central point of FM is obtained in all cases. This strain profile can be understood by looking at the electric field in Fig. 3.1(c) and considering that, in the absence of external stress, we have $\varepsilon_{yy} = d_{13}E_z$, where $d_{13} = -1.23 \times 10^{-10}\mathrm{C\,N}^{-1}$ in our case. Other factors, such as residual stresses due to substrate clamping, also affect the strain, but their contribution is small. In Fig. 3.2(b), the strain gradient at the center ($y = 0$) as a function of w_{PZ} is plotted. The gradual decrease is a consequence of the electric field scaling with the inverse of the distance between electrodes $({w_{\mathrm{PZ}}}^{-1})$.

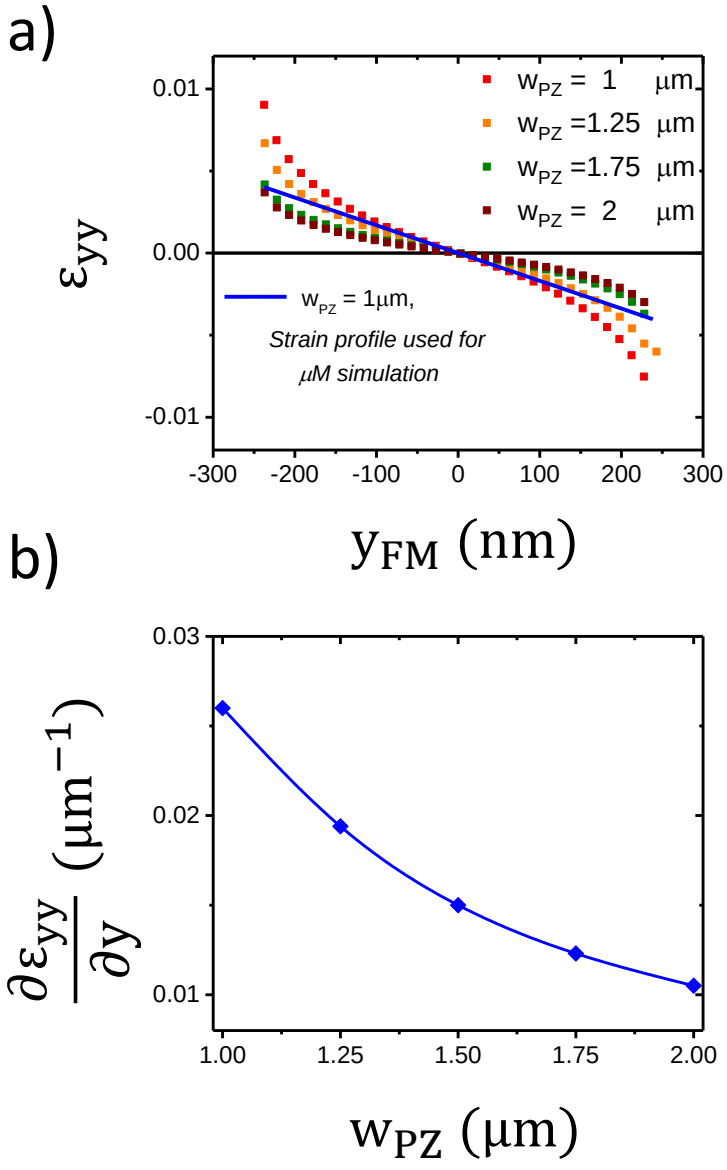

Fig. 3.2.: a) Elastic strain (ε_{yy}) profile transferred to the FM layer across the central region for different PZ layer widths. The blue line represents a linear profile obtained by extrapolating the slope at the origin ($y = 0$) for $w_{\mathrm{PZ}} = 1\,\mu\mathrm{m}$. b) Strain gradient in the center of the FM ($y = 0$) for different PZ layer widths w_{PZ}. A voltage $V = 10$ V between the electrodes is applied in all cases.

To sum up, our electromechanical simulations show that by applying moderate voltages between the electrodes, it is possible to create strain gradients in the central region of the FM racetrack in the order $10^{-2}\,\mu\mathrm{m}^{-1}$. Moreover, the magnitude of the gradient can be controlled by the applied voltage and the distance between the electrodes.

3.2.2 Strain-control of the skyrmion Hall effect

In the previous section, we characterized the mechanical response of the device, showing the creation of a transverse strain gradient due to the spacial electric field profile. Let us now investigate how this strain gradient can be used to control the lateral motion of skyrmions in our system. To do that, we perform micromagnetic simulations of a skyrmion driven by a current flowing through the HM layer (Fig. 3.1(a)) in the presence of a transverse strain gradient $\frac{\partial \varepsilon_{yy}}{\partial y}$. Simulations are carried out using a GPU-based in-home modified version of Mumax[3] [100] that includes a magneto-elastic contribution to the effective field as introduced in Sec. 2.5 and given by

$$\mathbf{H}_{\mathrm{mel}} = \frac{1}{\mu_0 M_{\mathrm{s}}} \sigma_{ij} \frac{\delta \varepsilon_{ij}^{m}}{\delta \mathbf{m}} \tag{3.1}$$

where σ_{ij} and ε_{ij}^{m} are the stress and magnetic strain tensors, respectively, M_{s} is the saturation magnetization, μ_0 the vacuum permeability, and $\mathbf{m}(\mathbf{r},t) = \frac{\mathbf{M}(\mathbf{r},t)}{M_{\mathrm{s}}}$ the reduced magnetization. The Landau-Lifshitz-Gilbert dynamic equation is augmented with Slonczewski-like spin-orbit torque that takes into account the contribution of the current flowing through the HM, as shown in Sec. 2.6 [145]. The following material parameter values, typical of Oxide/CoFeB/HM multilayers [146–150], were used in the micromagnetic simulations: $A_{\mathrm{ex}} = 20\,\mathrm{pJ\,m^{-1}}$ (exchange stiffness), $M_{\mathrm{s}} = 1\,\mathrm{MA\,m^{-1}}$ (saturation magnetization), $K_{\mathrm{u}} = 0.8\,\mathrm{MJ\,m^{-3}}$ (uniaxial anisotropy), $D = 1.8\ \mathrm{mJ\,m^{-2}}$ (interfacial Dzyaloshinskii-Moriya), $\lambda_{\mathrm{s}} = 3.7 \times 10^{-5}$ (magnetostriction), $\alpha = 0.3$ (damping constants), and $\theta_{\mathrm{sh}} = -0.33$ (spin Hall angle).

Fig. 3.3 shows the effect of the transversal strain gradient on the skyrmion dynamics. In Fig. 3.3(b), we plot the skyrmion trajectory for an applied current density $10\,\mathrm{GA\,m^{-2}}$ and different values of the strain gradient $\frac{\partial \varepsilon_{yy}}{\partial y}$. As can be observed, the skyrmion Hall angle decreases as the strain gradient is increased. This trend is confirmed in Fig. 3.3(c), where the skyrmion Hall angle is plotted as a function of the strain gradient for three different applied current densities, showing a monotonous decrease in all cases. The strain gradient, therefore, creates a force that pushes

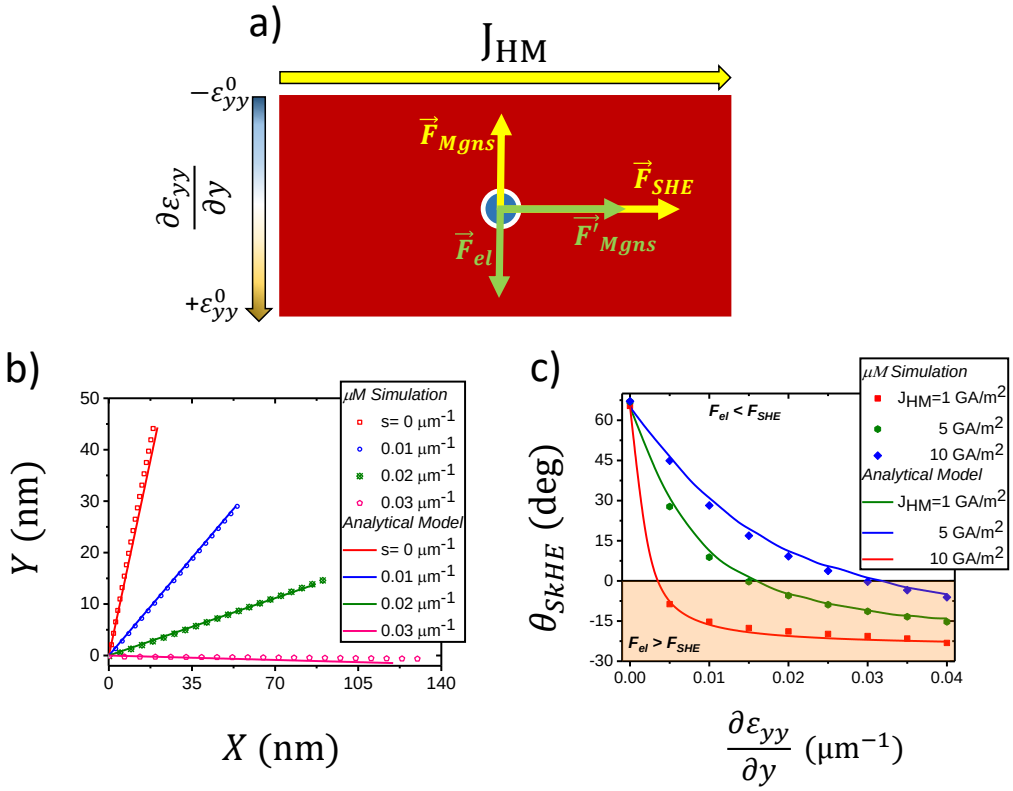

Fig. 3.3.: a) Schematic representation of the force contributions on the skyrmion dynamics. b) Skyrmion trajectories obtained from micromagnetic simulations (dots) and analytical calculations (lines) for a current density $J_{HM} = 10\,GA/m^2$ and different strain gradients. In the legend, "s" stands for "strain gradient", $s \equiv \frac{\partial \varepsilon_{yy}}{\partial y}$. c) Evolution of the skyrmion Hall angle with the strain gradient for different current density values.

the skyrmion towards regions of higher strain. The origin of this force, which was analyzed in [128], relies on the fact that the skyrmion energy is reduced as the strain increases. This force, F_{el}, is schematically represented in Fig. 3.3(a) (green) together with the driving force exerted by the current F_{SHE} (yellow). Their associated skyrmion Magnus forces, F_{Mgns} and F'_{Mgns}, are also represented. Skyrmion dynamics in our system can be understood in terms of these four forces acting on it.

In addition to micromagnetic simulations, the well-known Thiele's model [115] (presented in Sec. 2.8.2), can also give us useful information. In particular, analytical expressions for the forces involved can be derived. Using Thiele's equation Eq. (2.69) with the forces due to the spin-polarized current $\mathbf{F}_{SHE}$ and the strain gradient $\mathbf{F}_{el}$, the equation describing the skyrmion dynamics can be expressed as

$$\mathbf{G} \times \mathbf{V} - \alpha \bar{\bar{\mathcal{D}}} \cdot \mathbf{V} = \mathbf{F}_{SHE} + \mathbf{F}_{el} \tag{3.2}$$

where $\mathbf{G} = -4\pi\left(Q_{\rm sk}\right)\frac{\mu_0 M_{\rm s}}{\gamma_0}t_{\rm FM}\mathbf{e}_z$ is the gyrovector with $Q_{\rm sk} = -1$ the skyrmion topological charge, $\mathbf{V}$ is the skyrmion velocity, and $\bar{\bar{\mathcal{D}}} = \begin{pmatrix} \mathcal{D}_{xx} & \mathcal{D}_{xy} \\ \mathcal{D}_{yx} & \mathcal{D}_{yy} \end{pmatrix}$ is the dissipation tensor with $|\mathcal{D}| = \mathcal{D}_{xx} = \mathcal{D}_{yy} = \frac{\mu_0\pi M_{\rm s}}{2\gamma_0}t_{\rm FM}\left(\pi^2 - {\rm Ci}(2\pi) + \gamma_E + \log(2\pi)\right)$, and $\mathcal{D}_{xy} = \mathcal{D}_{yx} = 0$, with Ci and γ_E being the cosine integral function and Euler constant, respectively. The force due to the Spin-Hall effect is given by $\mathbf{F}_{\rm SHE} = \frac{\hbar\theta_{\rm sh}{\rm J}_{\rm HM}}{2|e|}\pi^2\eta\frac{\Delta}{2}\mathbf{e}_x$, where $\theta_{\rm sh}$ is the spin Hall angle, ${\rm J}_{\rm HM}$ is the current density flowing through the HM, $\Delta = 31$ nm is the skyrmion wall width, e is the electron charge, and η is a fitting parameter. On the other hand, the force due to the strain gradient is given by $\mathbf{F}_{\rm el} = \frac{3\pi\Delta^2\lambda_{\rm s}}{8}t_{\rm FM}\left(C_{11}+C_{12}\right)\frac{\partial\varepsilon_{yy}}{\partial y}\mathbf{e}_y$, where $\lambda_{\rm s}$ is the magnetostriction, $C_{11} = \frac{\mathcal{Y}(1-\nu)}{(1+\nu)(1-2\nu)}$ and $C_{12} = \frac{\nu\mathcal{Y}}{(1+\nu)(1-2\nu)}$ are the elastic constants, and $t_{\rm FM}$ is the ferromagnetic layer thickness. All these terms were calculated using the zero-radius skyrmion ansatz described in [128].

From Eq. (3.2) the longitudinal and transversal components of the skyrmion velocity are given by

$$V_x = \frac{\alpha|\mathcal{D}|F_{\rm SHE} + GF_{\rm el}}{\alpha^2|\mathcal{D}|^2 + G^2} \tag{3.3a}$$

$$V_y = \frac{-GF_{\rm SHE} + \alpha|\mathcal{D}|F_{\rm el}}{\alpha^2|\mathcal{D}|^2 + G^2} \tag{3.3b}$$

so that the skyrmion Hall angle is

$$\theta_{\rm SkHE} = \tan^{-1}\left(\frac{-GF_{\rm SHE} + \alpha|\mathcal{D}|F_{\rm el}}{\alpha|\mathcal{D}|F_{\rm SHE} + GF_{\rm el}}\right) \tag{3.4}$$

In Fig. 3.3(b) and Fig. 3.3(c), we show the predictions of the model (solid lines) together with the results of micromagnetic simulations (symbols). The same parameter values have been used in both of them, with $\eta = 1.05$ as the only fitted parameter in Thiele's model. As can be observed, good quantitative agreement is found, which indicates that Thiele's model captures the most relevant features of skyrmion dynamics in our system. The discrepancies between the simulations and the model are mainly attributed to the fact that the skyrmion diameter depends on the strain [151] and, therefore, it changes as the skyrmion moves in the presence of a strain gradient, a feature not considered in Thiele's model. Moreover, we can extract from the model the condition that needs to be satisfied for the skyrmion to move straight along the nanostrip without transversal deflection. By making either $V_y = 0$ in Eq. (3.3b) or $\theta_{\rm SkHE} = 0$ in Eq. (3.4) we obtain

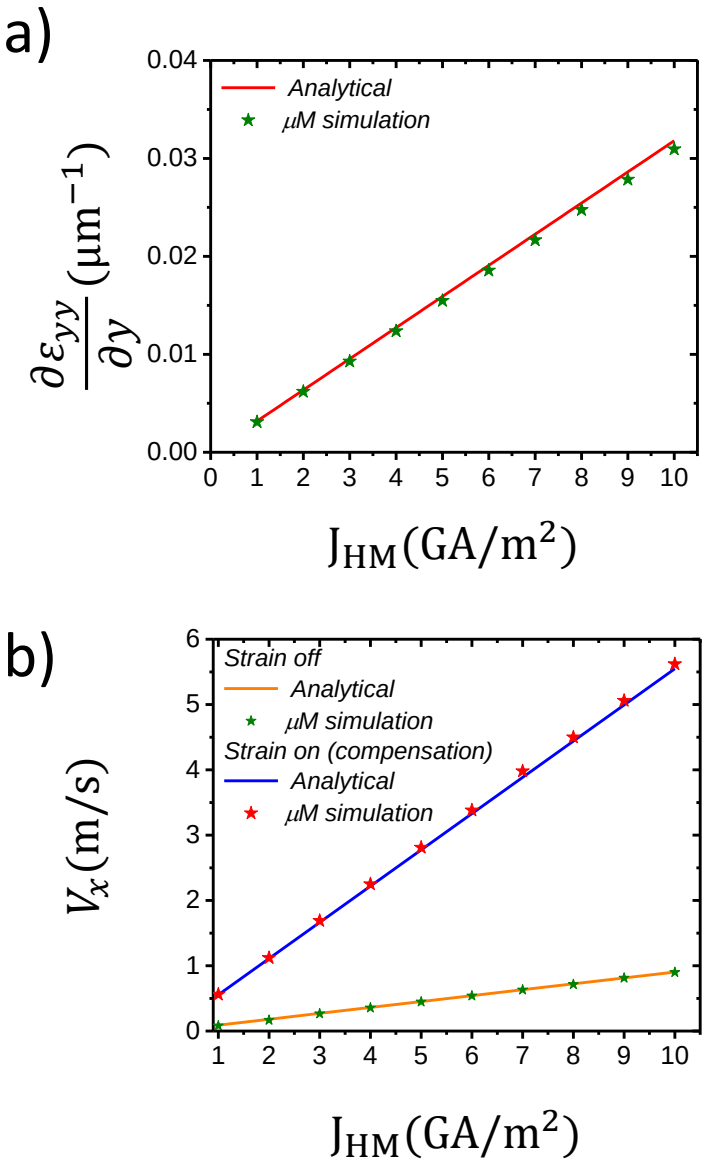

Fig. 3.4.: a) Strain gradient slope required to compensate the skyrmion Hall angle for each current density value J_{HM}. b) Skyrmion speed versus applied current in the absence of strain and in presence of a strain compensating the skyrmion Hall angle.

$$F_{\mathrm{el}} = \frac{G}{\alpha|\mathcal{D}|} F_{\mathrm{SHE}} \tag{3.5}$$

as the condition that guarantees the suppression of the skyrmion Hall effect. Using Eq. (3.5) and the expressions of F_{SHE} and F_{el} given above, we can obtain, for any given current density $\mathrm{J_{HM}}$, the value of the strain gradient $\frac{\partial \varepsilon_{yy}}{\partial y}$ needed to cancel the SkHE

$$\frac{\partial \varepsilon_{yy}}{\partial y} = \frac{2\pi\eta G\hbar\theta_{\mathrm{sh}}}{3\alpha|\mathcal{D}||e|\Delta\lambda_{\mathrm{s}} t_{\mathrm{FM}}\left(C_{11}+C_{12}\right)} \mathrm{J_{HM}} \tag{3.6}$$

Fig. 3.4(a) shows the value of the strain gradient that cancels the skyrmion Hall effect for different values of the applied current density as obtained from micromagnetic simulations (green symbols) and from Eq.(3.6) (red line). Again, an excellent agreement is found between them. The discrepancies are even smaller than in Figs. 3.3(b) and (c) because now the skyrmion moves horizontally, perpendicularly to the strain gradient and, therefore, its diameter does not change during motion.

On the other hand, in Fig. 3.4(b), we plot the skyrmion speed as a function of the current density obtained from micromagnetic simulations, both without strain gradient (green symbols) and with the strain gradient that cancels the skyrmion Hall effect (red symbols). The corresponding values obtained from Thiele's model are also shown with solid lines (orange and blue, respectively). As can be observed, a linear increase in the longitudinal velocity (V_x) is obtained in both cases, but the speed values are remarkably higher when the strain gradient is included. This can be understood by considering that $\mathbf{F}'_{\mathrm{Mgns}}$, the Magnus force associated with $\mathbf{F}_{\mathrm{el}}$, points along the positive x-axis (see Fig. 3.3(a) and Eq. (3.3a) and, as a result, it adds up to $\mathbf{F}_{\mathrm{SHE}}$, increasing the total force pushing the skyrmion along the nanostrip. Therefore, by choosing the appropriate value of the strain gradient, which depends linearly on the applied voltage, it is possible not only to suppress the skyrmion Hall effect but also to increase its velocity significantly.

Up to now, we have shown that our scheme for tuning the skyrmion Hall angle works for idealized samples, but it remains to be shown whether it would also work under realistic conditions, where intrinsic pinning due to structural disorder is known to play an important role in skyrmion dynamics [152]. With that goal in mind, we carried out simulations with the same geometry and material parameter values described before but now including disorder [153]. Disorder is modeled via a Voronoi tessellation of the film in polygonal regions of average diameter $d = 5\ \mathrm{nm}$, where both anisotropy constant and easy-axis orientation are different for each grain

following a Gaussian distribution around their nominal values, $K_{\mathrm{u}} = 0.8\,\mathrm{MJ\,m^{-3}}$ and $\mathbf{e}_k = \{0, 0, 1\}$, with standard deviation $\sigma = 2\%$. The results are shown in Fig. 3.5 together with those carried out in the absence of disorder for an applied current density $\mathrm{J_{HM}} = 30\,\mathrm{GA\,m^{-2}}$. This value is well above the range investigated in Fig. 3.3 because we are mainly interested in the flow regime.

Both the skyrmion speed (Fig. 3.5(a)) and skyrmion Hall angle (Fig. 3.5(b)) as a function of the strain gradient are plotted. In the simulations with disorder (red squares), the results are obtained by averaging over 10 realizations, each one with a different grain distribution. As can be observed in Fig. 3.5(a), the increase in the skyrmion speed with the strain gradient remains in the presence of disorder. On the other hand, disorder leads to a reduction in the skyrmion Hall angle (Fig. 3.5(b)) [116, 154, 155], but also a monotonous decrease with the strain gradient is obtained, as in the case without disorder. Although the results shown in this chapter were carried out without considering thermal fluctuations in the simulations, some trials were made at a finite temperature, and the results did not show a significant effect on the skyrmion Hall angle for the current density range considered. In a recent publication [156], it was shown that the skyrmion Hall angle is not significantly affected by temperature unless a high-flow regime is reached where some distortion on the skyrmion structure takes place. A previous computational study [157] showed that the effect of temperature on the skyrmion Hall angle is most pronounced at small drives where thermally-induced depinning occurs, whereas in the flow regime it slightly increases with temperature.

3.2.3 Strain-enhanced skyrmion dynamics in narrow magnetic racetrack systems

As pointed out in Sec. 3.1, in narrow nanostrips, the edges exert a repulsive force on the skyrmions that affect their dynamics. In particular, this force increases as the skyrmion deviates from the center $(y = 0)$ and, at some point, it compensates the Magnus force due to the current, and the skyrmion ends up in a horizontal trajectory at a given distance y_{term} from the nanostrip central axis. However, for current densities above a certain critical value $\mathrm{J_c}$, the edge repulsion is not strong enough to compensate the magnus force, and the skyrmion is annihilated at the edge. This critical value, which depends on the nanowire width, limits the current range of the device operability. In the last part of this chapter, we explore how our approach can be used to increase this critical current. To do that, we simulate a nanostrip of dimensions $1024 \times 128 \times 1\ \mathrm{nm^3}$, narrower but with the same material parameter

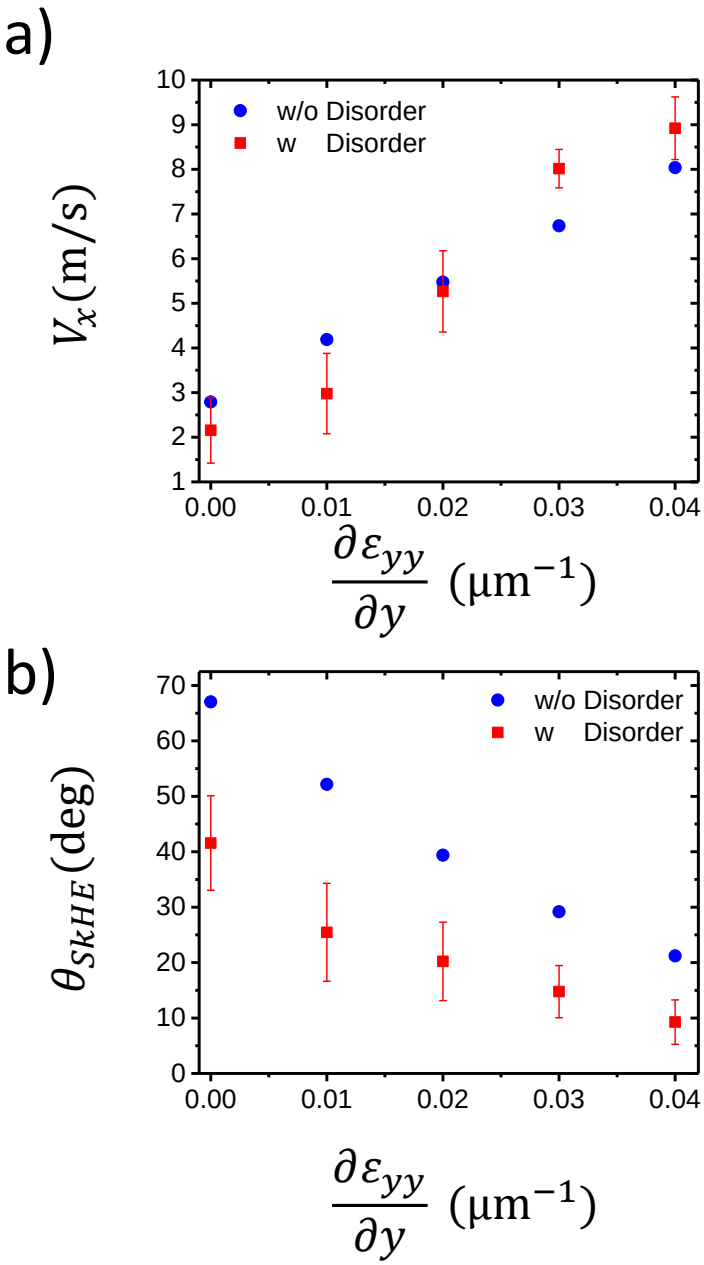

Fig. 3.5.: a) Skyrmion speed versus strain gradient for a disordered FM film (red dots) and for an ideal FM film (blue dots). b) Skyrmion Hall angle evolution versus the strain gradient for a disordered FM film (red dotes) and for an ideal FM film (blue dots). The graphs show a comparison between a disordered and ideal film in presence of a current density $J_{HM} = 30\,GA\,m^{-2}$.

values as the ones considered before (Fig. 3.1(a)). Thiele's model was also used by including an additional force in Eq. (3.2) that considers the repulsion from the edges, $\mathbf{F}_{\mathrm{rep}}$. Following previous works [59], it is modeled as $\mathbf{F}_{\mathrm{rep}} = kY(t)\mathbf{e}_y$, where $k = 3.610^{-5}\ \mathrm{N\,m^{-1}}$ is an elastic constant estimated from micromagnetic simulations, and $Y(t)$ is the skyrmion's transversal position. The dynamic equation Eq. (3.2) with the new term $\mathbf{F}_{\mathrm{rep}}$ can be solved analytically, yielding

$$X(t) = \frac{F_{\mathrm{SHE}}}{\alpha|\mathcal{D}|}t + \frac{G^2F_{\mathrm{SHE}} + G\alpha|\mathcal{D}|F_{\mathrm{el}}}{\alpha^2|\mathcal{D}|^2k}\left(1 - e^{-\frac{t}{\tau}}\right) \tag{3.7}$$

$$Y(t) = \frac{GF_{\mathrm{SHE}} - \alpha|\mathcal{D}|F_{\mathrm{el}}}{\alpha|\mathcal{D}|k}\left(1 - e^{-\frac{t}{\tau}}\right) \tag{3.8}$$

where $\tau = \frac{G^2+\alpha^2|\mathcal{D}|^2}{\alpha|\mathcal{D}|k}$ is the characteristic time for the skyrmion response to the edge force.

In Fig. 3.6, we show the skyrmion trajectory for a time window of $25\ \mathrm{ns}$ and different values of the applied current density without strain gradient (Fig. 3.6(a)) and for a strain gradient of $\frac{\partial\varepsilon_{yy}}{\partial y} = 0.08\,\mu\mathrm{m}^{-1}$ (Fig. 3.6(b)). The trajectories obtained from both micromagnetic simulations and Thiele's model are shown. As can be observed in Fig. 3.6(a), the terminal vertical displacement of the skyrmion increases with the current density and, for the largest one, $\mathrm{J_{HM}} = 60\,\mathrm{GA\,m^{-2}}$, the skyrmion is annihilated when it hits the boundary ($Y = \frac{w_{\mathrm{FM}}}{2} = 64\ \mathrm{nm}$). This terminal displacement is significantly reduced when the strain gradient is applied (Fig. 3.6(b)), up to the point that for the smallest current density values it is negative. This makes it possible for a current of $\mathrm{J_{HM}} = 60\,\mathrm{GA\,m^{-2}}$ and higher to be injected without the skyrmion being annihilated. Micromagnetic simulation and Thiele's model predict very similar behavior. The discrepancies between them are mainly attributed to the fact that the skyrmion radius changes as it moves vertically, as shown in the insets of Figs. 3.6(a) and (b), and also to the fact that the repulsion from the edges is not accurately described with an elastic force when the skyrmion is close to the edge [158]. In Fig. 3.6(c), we show the maximum current $\mathrm{J_c}$ that can be injected without the skyrmion being annihilated at the edge of the nanostrip for different values of $\frac{\partial\varepsilon_{yy}}{\partial y}$. As can be observed, $\mathrm{J_c}$ increases with the strain gradient, which proves that our approach can be used to inject higher currents in the nanostrip, with the consequent increase in speed and operating range of the devices.

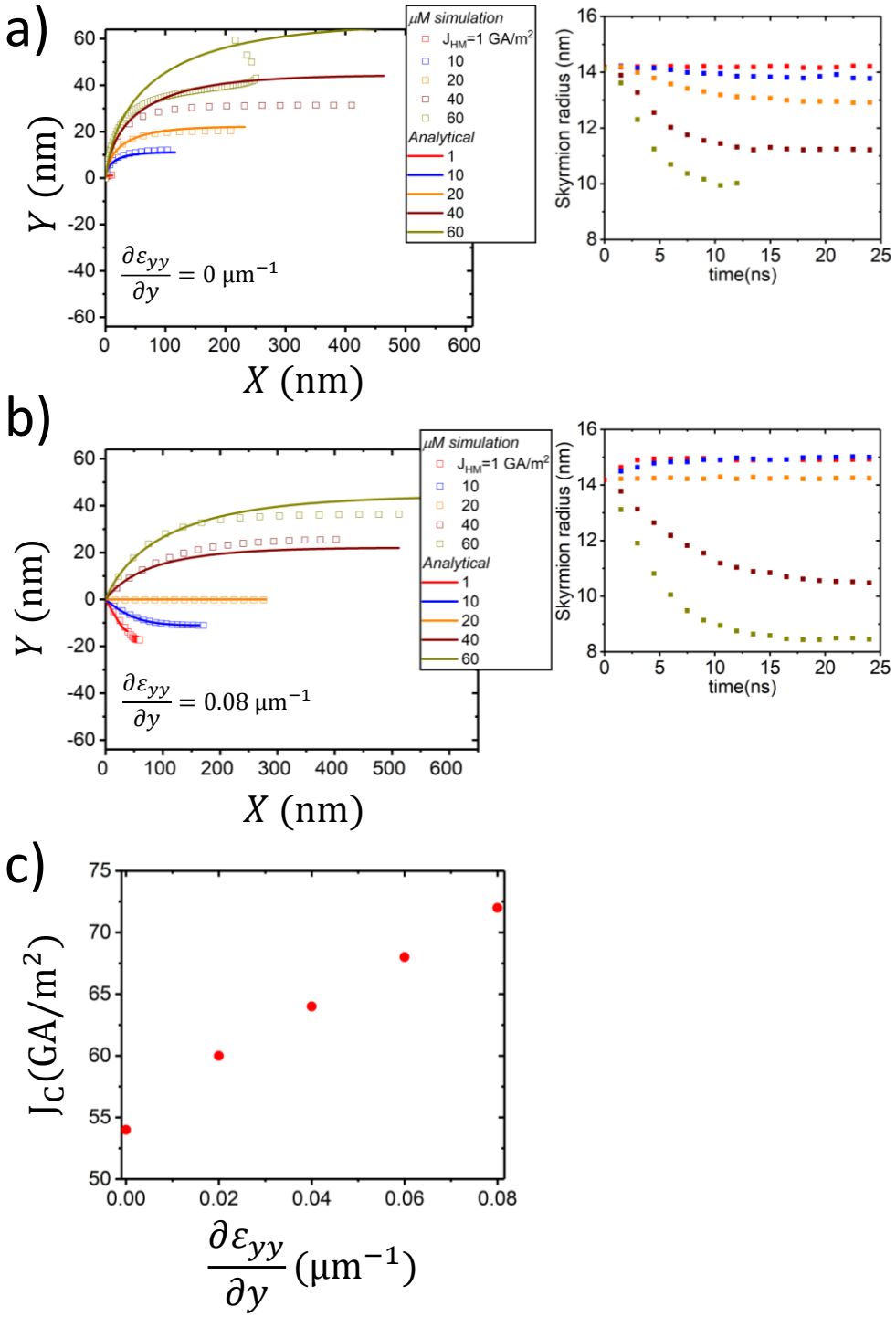

Fig. 3.6.: Skyrmion trajectory for different applied current densities: a) without, and b) in presence of a strain gradient. Both the results of micromagnetic simulations (symbols) and Thiele's model (lines) are shown. The time evolution of the skyrmion radius is shown in the insets. c) Threshold current for skyrmion annihilation as a function of the strain gradient.

3.3 Conclusion

To conclude, we showed in this chapter a new method to control the skyrmion trajectory and cancel out the skyrmion Hall effect via electric field in hybrid piezoelectric/magnetic multilayers. We investigated the electromechanical response of the device when a voltage is applied between two lateral electrodes, finding a transversal strain gradient in the central part of the ferromagnetic layer, the amplitude of which is linear with the applied voltage and with the inverse of the distance between the electrodes. Micromagnetic simulations show that such a strain gradient leads to a transverse force on the skyrmion that can have a sizable effect on its trajectory when driven by a current. In particular, the skyrmion Hall effect can be cancelled for any given current density if proper voltage is applied. Moreover, the strain gradient contributes to increasing the longitudinal velocity and in narrow nanostrips, it allows for an increase of the maximum current density that can be injected before the skyrmion is annihilated at the nanostrip edge. Our approach works under realistic conditions, in particular in the presence of structural disorder in the ferromagnet. From a broader perspective, we believe that the applicability of our approach goes beyond the possibility of canceling the skyrmion Hall angle but it provides additional degrees of freedom to control skyrmion motion, which could have a strong impact in the design of skyrmion-based memories, logic and neuromorphic computing devices.

4

Absence of Walker breakdown in the dynamics of chiral Néel domain walls driven by in-plane strain gradients

In this chapter, the influence of mechanical strain on the static and dynamic properties of chiral domain walls in perpendicular magnetized strips is investigated using micromagnetic simulations and an extended one-dimensional model. While uniform strain allows to reversibly switch the DW configuration at rest between Bloch and Néel patterns, strain gradients are suggested as an energy-sustainable manner to drive DW motion without the need for magnetic fields nor electrical currents. It is shown that an in-plane strain gradient creates a force on the DW that drives it towards regions of higher tensile (compressive) strain for materials with positive (negative) magnetostriction. Moreover, due to the dependence of the DW internal energy on in-plane strain, a damping torque proportional to the local strain arises during motion that opposes the precessional torque due to the driving force, which is proportional to the strain gradient. After a transient period, where both the internal DW angle and the velocity change non-monotonically, reaching their maximum values asynchronously, both torques balance each other. This compensation prevents the onset of turbulent DW dynamics, and steady DW motion with constant velocity is asymptotically reached for any arbitrarily large strain gradient. Despite these complex dynamics, our work points out that averaged DW velocities in the range of 500 m/s can be obtained using voltage-induced strain in piezoelectric/ferromagnetic devices under realistic conditions. This chapter is an adaptation of the author's publication [159].

4.1 Introduction

Reliable, fast, and efficient DW motion in perpendicularly magnetized media is a key aspect in the development of new spintronic devices for a variety of applications, such as memory [160], sensing [161], logic [162, 163], or neuromorphic computing [164, 165]. As discussed in Sec. 2.8.1, when driven by an external force, such as an out-of-plane field, the DW changes its internal structure due to the precessional component of the driving force, which rotates it away from its orientation at rest [85]. For low values of the driving force, a terminal DW angle is reached, for which this precessional torque is counterbalanced by the restoring torque that tries to bring it back to its equilibrium orientation, leading to the DW moving rigidly at a constant velocity. Above a certain threshold value, however, this balance is no longer possible, and continuous internal DW precession takes place during its motion, with the consequent reduction in speed. This phenomenon is Walker breakdown[166] explained already in chapter 2, and it is present, for example, when the driving force is an out-of-plane field [167] or a spin-polarized current via the spin-transfer torque [168]. It is not present, however, when Néel DWs move due to the spin Hall effect (SHE) [169], but in this case the DW is tilted towards the Bloch configuration as the current density increases, which reduces the efficiency of the SHE and leads to a saturation in the maximum velocity achievable. It is also absent in systems that exhibit antiferromagnetic coupling, such as antiferromagnets [170], ferrimagnets at angular momentum compensation [171], or synthetic antiferromagnets [172], since DW tilting is virtually suppressed due to strong exchange coupling.

Alternative ways to move DWs in perpendicularly magnetized media that do not require external fields nor charge currents are being explored. Some of them are based on using spatially variable physical quantities, such as anisotropy [173–176] or temperature [177, 178]. Others are based on geometry engineering and curvature effects [179]. Although the detailed mechanism that drives the DW in each case is different, all of them are based on the fact that DW energy depends on the spatially variable quantity, and consequently, a force appears that pushes the DW towards regions where its energy is lowered. This force is typically dependent on the local gradient of the spatially variable quantity [175], its effect is essentially equivalent to that of an external magnetic field, and, as such, WB occurs when the gradient exceeds a certain threshold value.

Recently, the effect of strain on magnetic DW dynamics has been reported in several theoretical and experimental studies. It was shown that by optimizing the spatial profile of the strain, one can trigger magnetic DWs motion along in-plane magnetized

strips[180–183]. Besides, other works showed that strain could be a useful tool to manipulate DW dynamics along perpendicularly magnetized films while being driven by other means such as magnetic fields [184].

Here we investigate the possibility of moving Néel DWs in perpendicularly magnetized media using an in-plane strain gradient. The main difference with the approaches mentioned before is that now not only DW energy but also its equilibrium orientation depend on in-plane strain. As it will be shown, this leads to substantial changes in DW dynamics with respect to the standard field-driven case. In particular, the interplay between the different torques involved keeps the internal DW angle bounded, preventing the appearance of precessional dynamics inside DW for any arbitrary strain gradient.

In the rest of this chapter, we will first explore the static properties of a DW in presence of a uniform strain. Later on we investigate the DW dynamics in presence of space-dependent profiles of either in-plane or/and perpendicular strain based on the extended one-dimensional model. Thereafter, the model predictions are tested by micromagnetic simulations under realistic conditions and finally, we present the main conclusions of this chapter and the perspectives of the work.

4.2 Results and Discussion

4.2.1 Static properties of a domain wall under uniform strain

Efficient control of the DW static properties is required for better manipulating them during the dynamic regime. Hence, here we first analyze the effect of a uniform strain on the DW features at rest. To do so, we rely on both micromagnetic simulation and a reduced 1D model. We consider a system that consists of a Néel DW located at the center of an infinite nanostrip subject to a uniform uniaxial strain ε_{ii} (where ii refers to strain direction $i : x, y, z$) as shown in Fig. 4.1(a). Although not shown in the figure, we assume that this ferromagnetic nanostrip is in contact with a heavy metal layer and that the Néel configuration is favored over the Bloch one due to the interfacial Dzyaloshinskii-Moriya interaction (DMI) [169]. As mentioned in chapter 2, within the 1D model approach, the magnetization is assumed to change only along the longitudinal x-axis ($\mathbf{M} = \mathbf{M}(x, t)$) [67, 101, 103, 185], and similarly to Eq.(2.46) the DW energy per unit area considering the magnetoelastic contribution reads

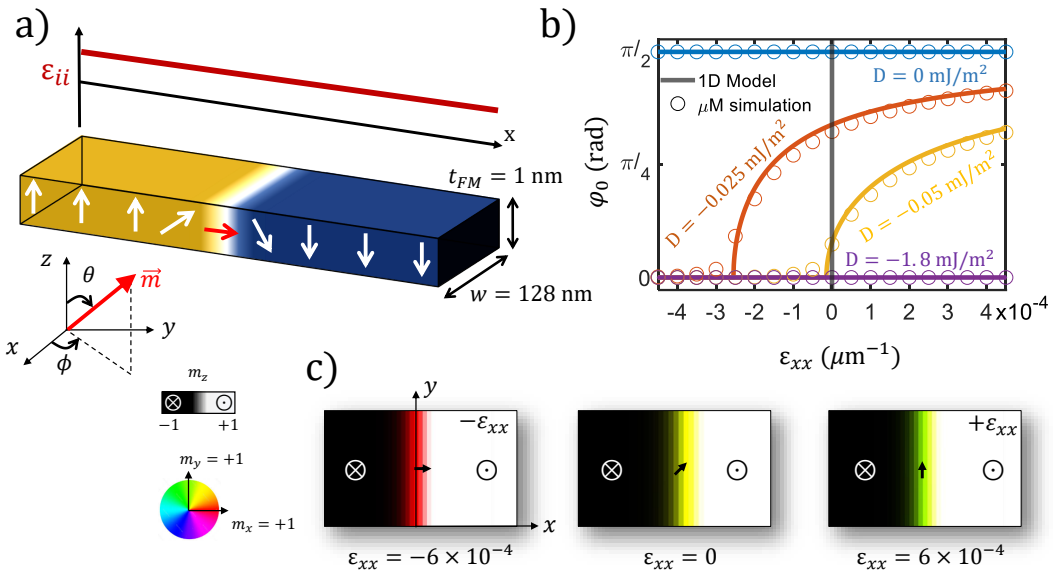

Fig. 4.1.: a) Schematic representation of the system under study. A Néel DW is located at the center of an ferromagnetic nanostrip subject to a uniform strain. b) DW equilibrium angle φ_0 as a function of the in-plane strain (ε_{xx}) for different values of interface DMI constant D as computed from both micromagnetic simulations (dots) and the 1D model (lines). c) Micromagnetic snapshots of down-up DW equilibrium patterns under different values of the in-plane strain (ε_{xx}) for a system with $D = -0.025\,\mathrm{mJ/m^2}$.

$$\mathcal{U}_{\mathrm{DW}} = \int_{-\infty}^{+\infty} [A_{\mathrm{ex}}(\nabla \mathbf{m})^2 - K_{\mathrm{u}} m_z^2 - \frac{\mu_0 M_s}{2} \mathbf{m} \cdot \mathbf{H}_{\mathrm{d}} + D(m_z \nabla \mathbf{m} - (\mathbf{m} \cdot \nabla) m_z) + B_1\, \varepsilon_{xx}\, m_x^2 + B_1\, \varepsilon_{zz}\, m_z^2]\, \mathrm{d}x \quad (4.1)$$

where $\mathbf{m}(\mathbf{x}, \mathbf{t}) = \frac{\mathbf{M}(\mathbf{x},\mathbf{t})}{M_s}$ is the normalized magnetization, $\mathbf{H}_{\mathrm{d}}$ is the self-magnetostatic field, and A_{ex}, K_u, D, and B_1 are the exchange, anisotropy, DMI, and first magnetoelastic constants, respectively. We assume that the longitudinal in-plane ε_{xx} and perpendicular ε_{zz} are the only components of the strain tensor present in the system, and $B_1 = -\frac{3}{2}\lambda_{\mathrm{s}}(C_{11} - C_{12})$, with λ_{s} being the saturation magnetostriction and C_{11} and C_{12} the elastic constants [186]. We use the standard 1D ansatz for the DW profile [67, 101, 102], $\theta(x,t) = 2\tan^{-1}[\exp\left(Q\frac{x-q(t)}{\Delta}\right)]$, $\phi(x,t) = \varphi(t)$ where $\theta(x,t)$ and $\phi(x,t)$ are the spherical coordinates of the magnetization as shown in Fig. 4.1, and q, Δ, and φ are the DW position, width, and angle, respectively, whereas the factor Q refers to up-down ($Q = +1$) or down-up ($Q = -1$) DW configurations.

By integrating Eq. (4.1) using the 1D ansatz and assuming that strain is uniform over the system we obtain

$$\mathcal{U}_{\text{DW}} = \frac{2A_{\text{ex}}}{\Delta} + 2\Delta(K_{\text{eff}} + K_{\text{sh}}\sin^2\varphi + B_1\varepsilon_{xx}\cos^2\varphi - B_1\varepsilon_{zz}) + \pi QD\cos\varphi \quad (4.2)$$

with $K_{\text{eff}} = K_{\text{u}} - \frac{1}{2}\mu_0 M_{\text{s}}^2$ and $K_{\text{sh}} = \frac{1}{2}\mu_0 M_{\text{s}}^2(N_y - N_x)$ being the effective and shape anisotropy constants, respectively. The internal DW angle at rest φ_0 is obtained by minimizing Eq. (4.2) with respect to φ. The resulting angle is

$$\varphi_0 = \cos^{-1}\left[\frac{\pi QD}{4\Delta(K_{\text{sh}} - B_1\varepsilon_{xx})}\right] \quad (4.3)$$

if $\pi|D| < 4\Delta|K_{\text{sh}} - B_1\varepsilon_{xx}|$. Otherwise, $\varphi_0 = 0$ (π) for $D < 0$ (> 0). As the term proportional to ε_{zz} in Eq. (4.2) is independent on φ, the equilibrium internal DW angle [Eq. (4.3)] is not affected by perpendicular strain. On the contrary, Eq. (4.3) shows that the DW internal angle is dependent on in-plane strain ε_{xx}. Fig. 4.1(b) shows the equilibrium angle φ_0 as a function of in-plane strain for different values of D as computed from the 1D model (lines) and from micromagnetic simulations (dots). Typical material parameter values for Pt/Co were adopted for both the 1D model and micromagnetic simulations, which were performed using the GPU-accelerated code MuMax3 [100]: $M_{\text{s}} = 0.58\,\text{MA}\,\text{m}^{-1}$, $A_{\text{ex}} = 30\,\text{pJ}\,\text{m}^{-1}$, $K_{\text{u}} = 0.9\,\text{MJ}\,\text{m}^{-3}$, $B_1 = 1.2\,\text{MJ}\,\text{m}^{-3}$ ($\lambda_{\text{s}} = -5\times10^{-5}$, $C_{11} = 298\,\text{GPa}$, $C_{12} = 133\,\text{GPa}$). Bloch walls ($\varphi_0 = \frac{\pi}{2}$) are found in the absence of DMI (for our nanowire dimensions $N_y \ll N_x$ and, therefore, $K_{\text{sh}} < 0$), whereas large DMI ($D = -1.8\,\text{mJ}/\text{m}^2$) stabilizes the Néel DWs with right-handed chirality ($\varphi_0 = 0$). For intermediate values of DMI, Fig. 4.1(b) shows that it is possible to sizably tune the equilibrium angle towards Bloch (Néel) configuration by applying moderate positive (negative) strain ($|\varepsilon_{xx}| < 5\times10^{-4}$). This effect is also evident in Fig. 4.1(c), where micromagnetic snapshots are shown for three different values of the in-plane strain (ε_{xx}). This is consistent with a recent work[187] that showed how an in-plane anisotropy modulation can be used to transform between Bloch and Néel DWs. Indeed, our analysis shows that this can be done using in-plane strain. Namely, tensile (compressive) strain favors Néel DWs for materials with $B_1 < 0$ (> 0). Besides, for a given material, changing the strain type (from tensile to compressive) can induce a transition from Bloch to Néel DW under realistic strain magnitudes. These results suggest that the current-driven DW dynamics under spin-orbit torques could also be also controlled with the assistance of uniform in-plane strain [188].

4.2.2 Strain-driven domain wall dynamincs

After proving the dependence of the equilibrium DW configuration on the in-plane strain, let us now focus on its dynamics in presence of a space-dependent one. To do so, we consider the same system as in Fig. 4.1(a), but with a DW subject to an in-plane uniaxial strain ε_{xx} that changes linearly along the longitudinal coordinate as shown in Fig. 4.2(a). To highlight the peculiarities of DW dynamics under such in-plane strain, we compare it with that of a perpendicular strain ε_{zz} with the same linear profile (Fig. 4.2(a)) but with a positive slope since, as it will be shown later, the two gradients need to have opposite signs to produce DW motion along the same direction. We keep the same material parameters as in Sec. 4.2.1 along with a Gilbert damping constant $\alpha = 0.05$. To understand the strain-driven DW mechanism, we develop the one-dimensional (1D) model [67, 101, 103] by considering that the strain varies linearly along the longitudinal x-axis as

$$\varepsilon_{ii}(x) = \frac{\partial \varepsilon_{ii}}{\partial x}\, x = \varepsilon'_{ii} x \tag{4.4}$$

By substituting Eq. (4.4) in Eq. (4.1) and integrating, the DW energy density now reduces to

$$\mathcal{U}_{\mathrm{DW}} = \frac{2A}{\Delta} + 2\Delta(K_{\mathrm{eff}} + K_{\mathrm{sh}} \sin^2\varphi - B_1 \varepsilon'_{zz}\, q + B_1 \varepsilon'_{xx}\, q \cos^2\varphi) + \pi Q\, D \cos\varphi \tag{4.5}$$

which indicates that the term proportional to ε'_{zz} does not depend on the DW angle φ, whereas the one proportional to ε'_{xx} does. Using Eq. (4.5), the equations describing the DW dynamics within the 1D approach can be obtained following the conventional procedure [189], which is detailed in Sec. 2.8.1, yielding

$$(1+\alpha^2)\frac{\dot{q}}{\Delta} = -\alpha\, \Gamma_{\mathrm{A}}(\varphi) + Q\, \Gamma_{\mathrm{B}}(q,\varphi) \tag{4.6a}$$

$$(1+\alpha^2)\dot{\varphi} = -Q\, \Gamma_{\mathrm{A}}(\varphi) - \alpha\, \Gamma_{\mathrm{B}}(q,\varphi) \tag{4.6b}$$

with

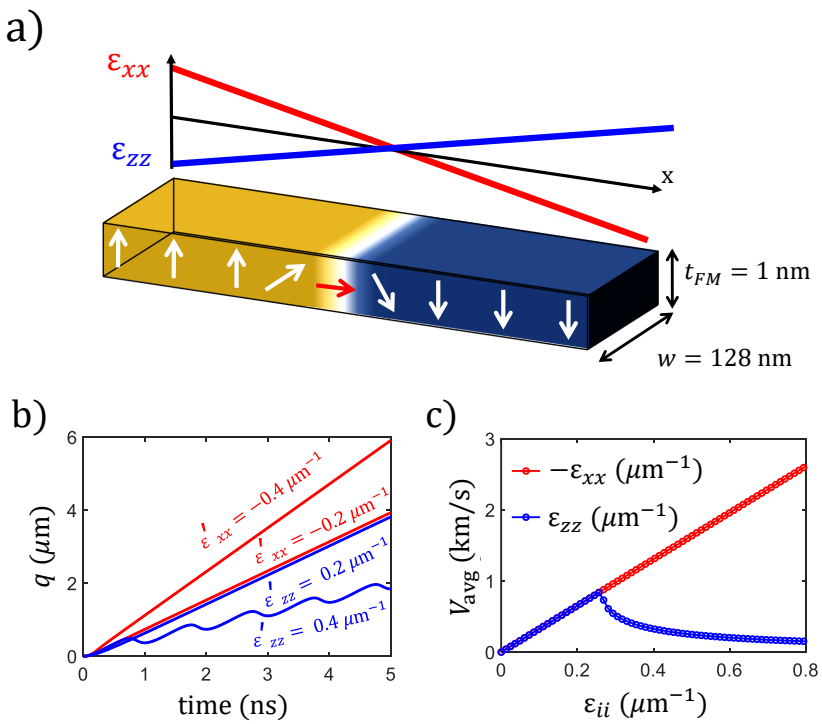

Fig. 4.2.: a) Schematic representation of the system under study. A Néel DW is initially located at the center of a ferromagnetic nanostrip subject to a strain gradient. In-plane and perpendicular strain profiles are shown by red and blue colors respectively. b) DW position (q) versus time as driven by two different in-plane (red) and perpendicular (blue) strain gradients. c) Average DW velocity versus strain slope for the in-plane (red) and perpendicular (blue) cases.

$$\Gamma_{\mathrm{A}}(\varphi) = \gamma_0 \Delta H_{\mathrm{mel}} (\varepsilon'_{xx} \cos^2 \varphi - \varepsilon'_{zz}) \tag{4.7a}$$

$$\Gamma_{\mathrm{B}}(\varphi, q) = \gamma_0 \left[\left(\frac{H_{\mathrm{sh}}}{2} - H_{\mathrm{mel}} \varepsilon'_{xx} q \right) \sin 2\varphi - \frac{\pi}{2} Q H_{\mathrm{DMI}} \sin \varphi \right] \tag{4.7b}$$

where $H_{\mathrm{mel}} = {}^{B_1}/_{\mu_0 M_{\mathrm{s}}}$, $H_{\mathrm{sh}} = {}^{2K_{\mathrm{sh}}}/_{\mu_0 M_s}$ and $H_{\mathrm{D}} = {}^{D}/_{\mu_0 M_{\mathrm{s}} \Delta}$ are magnetoelastic, shape anisotropy and DMI fields, respectively. In what follows, we will refer to the in-plane strain gradient case when $\varepsilon'_{xx} \neq 0$ and $\varepsilon'_{zz} = 0$, and to the perpendicular strain gradient case when $\varepsilon'_{xx} = 0$ and $\varepsilon'_{zz} \neq 0$.

In analogy with the conventional field-driven case [67, 190], the term $-\alpha\, \Gamma_{\mathrm{A}}$ in Eq. (4.6a) can be considered as the driving agent that pushes the DW along the direction of decreasing energy, i.e. increasing tensile (compressive) strain if $B_1 < 0$ (> 0) for the in-plane strain gradient case and increasing compressive (tensile) strain if $B_1 < 0$ (> 0) for the perpendicular one. On the other hand, the two terms on the RHS of Eq. (4.6b) can be viewed as the precessional $(-Q\, \Gamma_{\mathrm{A}})$ and damping $(-\alpha\, \Gamma_{\mathrm{B}})$ in-plane torques that govern the internal DW angle dynamics. Two main differences can be readily noticed between the in-plane and perpendicular cases. First, the contribution of ε'_{xx} to the precessional torque $(-Q\, \Gamma_{\mathrm{A}})$ is modulated by a factor $\cos^2 \varphi$, which is not the case for ε'_{zz}. Second, ε'_{xx} contributes to the damping torque $(-\alpha\, \Gamma_{\mathrm{B}})$, whereas ε'_{zz} does not. Moreover, this contribution also depends on the DW position q [see Eq. (4.7b)]. As we show below, this term has a strong impact on the response of the DW to the in-plane strain gradient.

Fig. 4.2(b) shows the time evolution of the DW position q predicted from the 1D model for two representative values of in-plane (red) and perpendicular (blue) strain gradients. Note that the dependence of the DW energy on ε'_{xx} and ε'_{zz} is of opposite sign [see Eq. (4.5)] and, therefore, to produce DW motion along the same direction the sign of the gradient also needs to be opposite. In our case $B_1 > 0$, so $\varepsilon'_{xx} < 0$ and $\varepsilon'_{zz} > 0$ lead to DW motion along the positive direction $(+x)$. As can be observed in Fig. 4.2(b), for small strain-gradients $(|\varepsilon'_{ii}| = 0.2\, \mu\mathrm{m}^{-1})$, steady DW motion with similar velocity is achieved in both in-plane and perpendicular cases. However, if the strain gradient increases $(|\varepsilon'_{ii}| = 0.4\, \mu\mathrm{m}^{-1})$ the response is very different. For perpendicular strain $(|\varepsilon'_{zz}| = 0.4\, \mu\mathrm{m}^{-1})$, the DW displays turbulent motion with a low averaged velocity, typical when the system exceeds the WB limit. On the contrary, the DW moves steadily with a higher velocity for the in-plane case $(|\varepsilon'_{xx}| = 0.4\, \mu\mathrm{m}^{-1})$. Fig. 4.2(c) shows the averaged DW velocity over a temporal window of $5\,\mathrm{ns}$ as a function of the strain gradient for both in-plane (red) and perpendicular (blue)

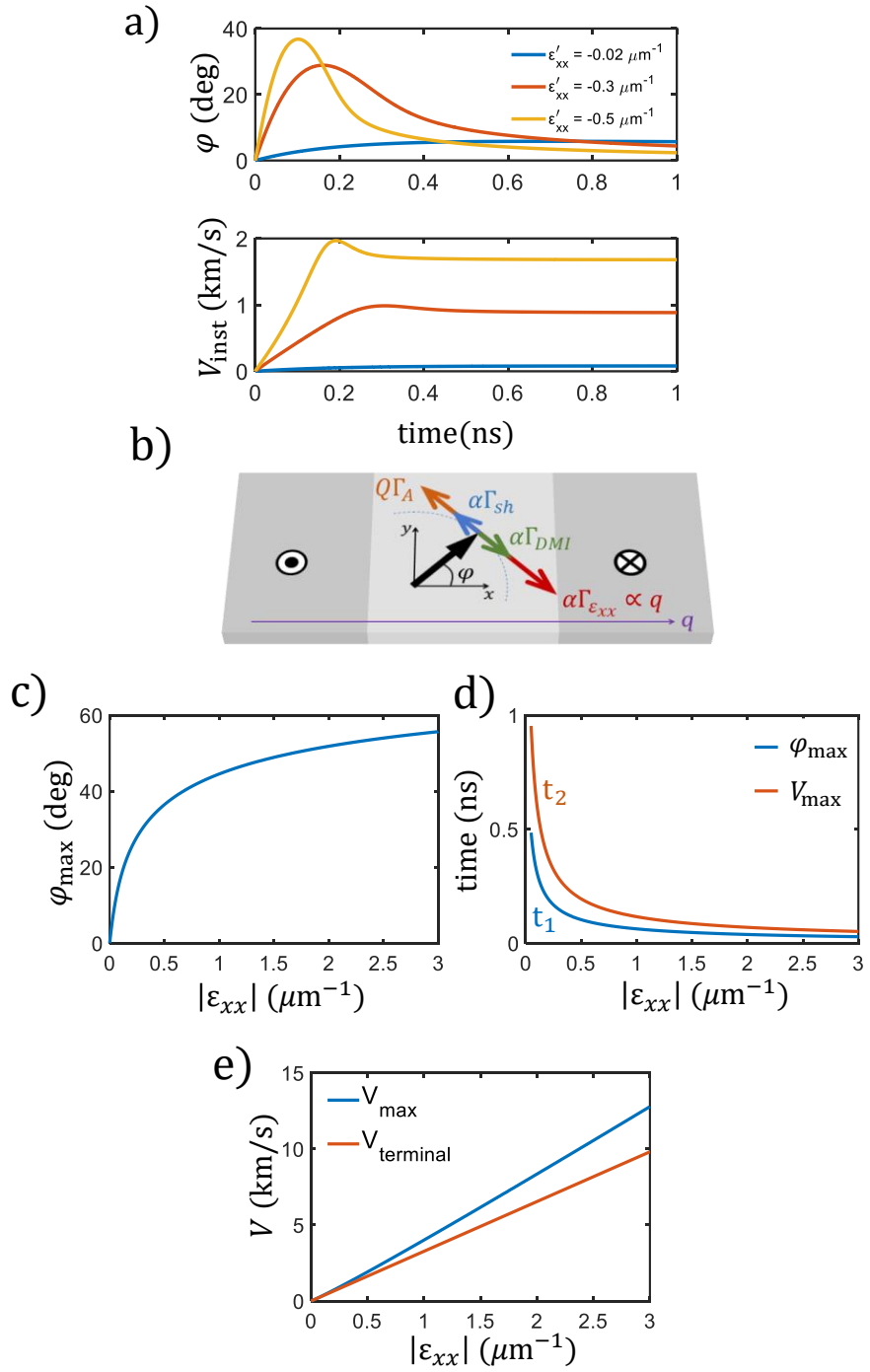

Fig. 4.3.: a) Temporal evolution of the DW angle and instantaneous velocity time as driven by an in-plane strain gradient ($\varepsilon'_{xx} \neq 0$ and $\varepsilon'_{zz} = 0$). b) Schematic representation of different torque contributions on the studied DW dynamics. c) Maximum tilting of the DW angle versus strain gradient. d) Characteristic time needed to reach the maximum angle (blue) and maximum velocity (orange). e) Maximum (blue) and terminal (orange) velocities versus strain gradient.

cases. For perpendicular strain, we observe WB at $\varepsilon'_{zz,\mathrm{WB}} = \frac{\alpha\pi H_{\mathrm{DMI}}}{2H_{\mathrm{mel}}\Delta} \approx 0.26\,\mu\mathrm{m}^{-1}$ as one would expect considering that the effect of a perpendicular strain gradient is equivalent to that of an external magnetic field $H_{\mathrm{eq}} = H_{\mathrm{mel}}\varepsilon'_{zz}\Delta$. Below WB limit, the DW moves rigidly and reaches a terminal velocity proportional to the strain gradient ($V = \frac{\gamma_0\Delta^2}{\alpha}H_{\mathrm{mel}}\varepsilon'_{zz}$), whereas above it the DW undergoes continuous internal precession, the velocity is no longer uniform and DW mobility is significantly reduced. For the in-plane case, however, no WB is observed and the DW mobility remains constant for arbitrarily high values of the strain gradient. This absence of WB in DW motion driven by an in-plane strain gradient is the main result of this chapter, in what follows, we will focus on explaining the mechanism that makes it possible.

Fig. 4.3(a) shows the time evolution of the DW angle φ (top) and its instantaneous velocity V_{inst} (bottom) for different values of the in-plane strain gradient ε'_{xx}. As it can be observed, a transient period, where both φ and V_{inst} change non-monotonically, takes place before the DW asymptotically reaches a steady velocity and the angle goes back towards its initial value ($\varphi = 0$). In order to shed light on this process, we analyze the different in-plane torques that govern the dynamics of the DW angle in Eq. (4.6b). On the one hand, we have the precessional component of the driving force, $-Q\Gamma_{\mathrm{A}}$, which drives the angle away from its equilibrium orientation. On the other hand, the damping torque ($-\alpha\Gamma_{\mathrm{B}}$) has three contributions, i.e. $\alpha\Gamma_{\mathrm{sh}} = -\alpha\gamma_0\frac{H_{\mathrm{sh}}}{2}\sin 2\varphi$, $\alpha\Gamma_{\mathrm{DMI}} = \alpha\gamma_0\frac{Q\pi H_{\mathrm{DMI}}}{2}\sin\varphi$ and $\alpha\Gamma_{\varepsilon'_{xx}}(q) = \alpha\gamma_0 H_{\mathrm{mel}}\varepsilon'_{xx}q\sin 2\varphi$. The first two of them are the standard shape anisotropy and DMI in-plane damping torques, and they are always present, regardless of the nature of the force that moves the DW. The third one, $\alpha\Gamma_{\varepsilon'_{xx}}(q)$, is specific to the in-plane strain gradient case, and, unlike the rest of them, its strength depends explicitly on the DW position q. These four in-plane torques are schematically represented in Fig. 4.3(b), where their corresponding signs are consistent with an up-down right-handed ($Q = +1$) DW moving along the $x > 0$ direction.

As soon as the DW starts moving due to the driving torque $-\alpha\Gamma_{\mathrm{A}}$, the corresponding precessional component $-Q\Gamma_{\mathrm{A}}$ tilts its angle away from the equilibrium orientation, and a restoring torque appears, trying to bring it back to its orientation at rest. When the driving force is an external field or a perpendicular strain gradient, the total restoring torque is given by $\alpha\Gamma_{\mathrm{sh}} + \alpha\Gamma_{\mathrm{DMI}}$ and if the driving force exceeds a certain threshold value, such restoring torque cannot balance the precessional one, and WB takes place. However, for an in-plane strain gradient, the third term, $\alpha\Gamma_{\varepsilon'_{xx}}(q)$, which opposes the precessional torque, also comes into play, with the peculiarity that its strength increases as the DW moves along the strain gradient (Fig. 4.3(b)), therefore contributing to bringing the angle closer to its value at rest. In fact, this

term guarantees that the DW angle remains bounded during motion regardless of the magnitude of the driving force, since its strength, like that of the precessional torque, is proportional to the strain gradient ε'_{xx} [Eq.(4.7.b)].

With this idea in mind, the transient behavior observed in Fig. 4.3(a) can be understood as follows: As the DW starts moving and the angle deviates from equilibrium value, the strength of the in-plane precessional torque $-Q\Gamma_{\mathrm{A}}$ decreases, whereas the in-plane damping torque $-\alpha\Gamma_{\mathrm{B}}$ increases. Since they have opposite signs, the total in-plane torque is gradually reduced up to a point where both terms balance out ($Q\Gamma_{\mathrm{A}} + \alpha\Gamma_{\mathrm{B}} = 0$) and the tilting angle reaches its maximum deviation ($\varphi_{\max}$). As shown in Fig. 4.3(c), this maximum deviation $\varphi_{\max}$ increases with the strain gradient ε'_{xx} but it saturates around $\frac{\pi}{3}$, proving our finding that the angle remains bounded no matter how large the strain gradient is. After $\varphi_{\max}$ is reached at a certain time t_1, the total in-plane torque changes sign ($|\alpha\Gamma_{\mathrm{B}}| > |Q\Gamma_{\mathrm{A}}|$) and φ starts decreasing, whereas the DW velocity continues increasing and up to reaching its maximum value $V_{\max}$ at a later time t_2. Fig. 4.3(d) shows how the two characteristic times of this transient dynamics, t_1 and t_2, depend on the strain gradient. As can be observed, they decrease in a similar fashion. As the DW moves further into the region of increasing strain, the term $\alpha\Gamma_{\varepsilon'_{xx}}$ becomes dominant ($|\Gamma_{\varepsilon'_{xx}}| \gg |\Gamma_{\mathrm{DMI}}|, |\Gamma_{\mathrm{sh}}|$) and the DW angle gradually goes back to its initial Néel orientation according to $\varphi(q) = \tan^{-1}\left(\frac{Q\Delta}{2\alpha q}\right)$. The DW velocity, meanwhile, asymptotically reaches a terminal value given by

$$V_{\text{term}} = \frac{\gamma_0 H_{\text{mel}} \Delta^2}{\alpha} \varepsilon'_{xx} \tag{4.8}$$

Fig. 4.3(e) shows both the terminal and maximum velocities as a function of the in-plane strain gradient. While the first one displays a perfectly linear trend, the second one has a slightly stronger dependence so that the difference between them increases with ε'_{xx}.

Up to now, we have investigated DW motion in presence of separate in-plane or perpendicular strain gradients. Although this assumption could be applied to some piezoelectric/magnetic systems, depending on the cut directions of the piezoelectric substrate, it is also possible to find that both in-plane and perpendicular strains are present in the system [191]. Therefore, investigating their joint effect on DW motion is also relevant. Thus, we consider the system in Fig. 4.2(a) with both $\varepsilon'_{xx} \neq 0$ and $\varepsilon'_{zz} \neq 0$. We parameterize them as $\varepsilon'_{zz} = -\beta\varepsilon'_{xx}$ with $\beta = |\frac{\varepsilon'_{zz}}{\varepsilon'_{xx}}|$ being the ratio between them. Considering that they should have opposite signs to produce DW motion in the same direction, the expression in Eq. (4.7.a) becomes

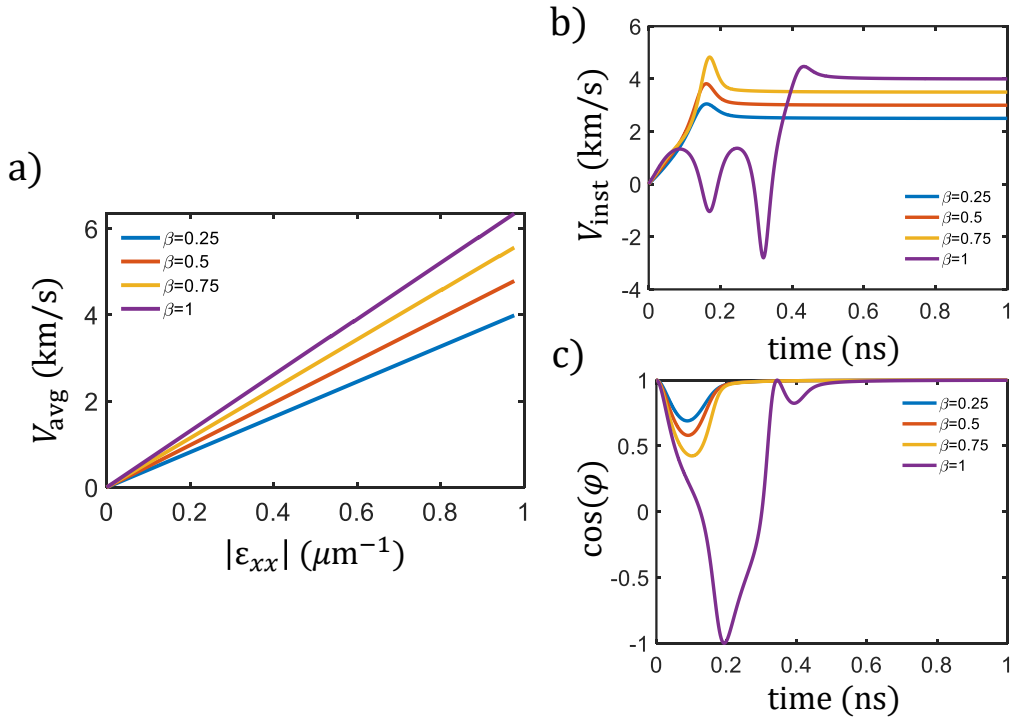

Fig. 4.4.: a) Average DW velocity as a function of the strain gradient for different $\beta = |\varepsilon'_{zz}/\varepsilon'_{xx}|$. b) Instantaneous DW velocity as a function of time for different values β and $\varepsilon'_{xx} = -0.61\,\mu\text{m}^{-1}$. c) Time evolution of the longitudinal component of the internal DW magnetization ($m_x = \cos\varphi$) for different ratios β and $\varepsilon'_{xx} = -0.61\,\mu\text{m}^{-1}$.

$\Gamma_{\text{A}}(\varphi) = \gamma_0 \Delta H_{\text{mel}} \varepsilon'_{xx}(\cos^2\varphi + \beta)$, whereas the $\Gamma_{\text{B}}(\varphi, q)$ remains the same as in Eq. (4.7.b).

Fig. 4.4 shows the dynamics of DWs for different values of the ratio β. As it can be noticed from Fig. 4.4(a), where the average DW velocity is plotted versus the strain gradient, the system does not depict any WB for any value of β. However, when we look at the instantaneous velocity plotted in Fig. 4.4(b) for a relatively high strain gradient ($\varepsilon'_{xx} = -0.61\,\mu\text{m}^{-1}$) two regimes are depicted. On the one hand, when $\beta < 1$ the system behaves similarly to the pure in-plane strain gradient case explained before, where no instabilities are found. On the other hand, when $\beta \geq 1$ the instantaneous DW velocity exhibits a nonlinear behavior during the transient dynamics. After reaching a maximum, the DW velocity decreases towards its terminal value. To shed more light on this complex transient dynamics, Fig. 4.4(c) shows the longitudinal component of the DW internal magnetization $m_x = \cos\varphi$ as a function of time for different values of β. It can be seen from Fig. 4.4(c) that the DW internal magnetization oscillates during the transient period for $\beta \geq 1$ leading to the onset of turbulent motion. Afterwards, it reaches an equilibrium value, and the

DW recovers a steady motion. We note that the behavior shown in Fig. 4.4 depends on both β and ε'_{xx}, and therefore, for larger values of ε'_{xx} than the ones shown here, the transient period of unstable DW motion appears for $\beta < 1$ as well.

We can interpret the results of Fig. 4.4 similarly to those obtained for in-plane strain gradients in terms of the action of the involved torques. In fact, by adding the contribution of ε'_{zz}, the strength of the precession torque ($-Q\Gamma_{\mathrm{A}}$) increases, while the damping torque ($-\alpha\Gamma_{\mathrm{B}}$) remains unaffected. This leads to a local breakdown of the compensation scheme explained before, and consequently, turbulent motion can take place if ε'_{zz} is large enough. On the other hand, as the DW moves, the damping torque $-\alpha\Gamma_{\mathrm{B}} \propto q$ gains strength and is eventually able to compensate the precession torque $-Q\Gamma_{\mathrm{A}}$. Then, the DW angle goes back towards its equilibrium configuration ($\varphi = 0$), and the DW recovers the steady motion with a constant terminal velocity given by

$$V_{\text{term}} = \frac{\gamma_0 H_{\text{mel}} \Delta^2}{\alpha} \varepsilon'_{xx}(1+\beta) \tag{4.9}$$

which shows that adding the contribution of the perpendicular strain gradient enhances significantly the DW motion in the steady regime.

Thus far, we have theoretically shown the absence of WB for a DW driven by in-plane strain gradients based on the 1D model. In doing so, we explored high-strain situations to prove that steady DW dynamics could be reached regardless of the strength of the driving force. However, in practice, there are limitations to the magnitude of the strain gradient that can be applied and the distance over which it can be maintained. Not only a large strain gradient can introduce mechanical damage in the device, but if strain is large enough to compete with perpendicular anisotropy ($|B_1 \varepsilon_{xx}| \sim K_{\text{eff}}$), which in our case happens when $\varepsilon_{xx} \sim 0.06$, the nucleation of in-plane domains starts taking place, and the system depicted in Fig. 4.2(a), with a DW separating two antiparallel domains, is no longer stable. Therefore, to explore the plausibility of our proposal under realistic conditions, micromagnetic simulations (μM) were performed using the same material parameters given before and a strain gradient over the strip length, which is fixed to $1\,\mu$m. Fig. 4.5(a) shows the time evolution of the DW angle φ for different values of ε'_{xx} as computed from both micromagnetic simulations (dots) and the 1D model (lines). As it can be observed, the simulations support the 1D results shown in Fig. 4.3. Indeed, the internal angle remains bounded even for the highest values of the strain gradient. To get a good agreement between the 1D model and the μM results, it was necessary to take into account in the former the sizable variations of the DW width [167] as

it goes deeper into the highly strained region and its effect on the demagnetizing factors[192]. Using the same method as for the (q, φ) 1D dynamic equations [103, 189], the following additional dynamic equation for the DW width is obtained (refer to Appendix. A.3 for further details)

$$\dot{\Delta} = \frac{12\gamma_0}{\alpha\mu_0 M_\mathrm{s}\pi^2}\Big[\frac{A_\mathrm{ex}}{\Delta} - \Delta\Big(K_\mathrm{eff} + K_\mathrm{sh}\sin^2\varphi - B_1\varepsilon'_{zz}\,q + B_1\varepsilon'_{xx}\,q\cos^2\varphi\Big)\Big] \quad (4.10)$$

Fig. 4.5(b) shows the average DW velocity V_avg as a function of the in-plane strain gradient for different values of α obtained from micromagnetic simulations (dots) and from the 1D model (lines). Due to the limitations mentioned before, the terminal velocity predicted by the 1D model Eq. (4.8) is not accessible in a $1\,\mu$m long strip. On the other hand, the non-linear dependence with ε'_{xx} observed for all values of α is due to the fact that the velocity is averaged over a short time interval in which the DW velocity is highly non-uniform, unlike in Fig. 4.1(c), where the time interval ($5\,$ns) is significantly larger than this transient period so that $V_\mathrm{avg} \approx V_\mathrm{term}$. In any case, Fig. 4.5(b) confirms that the absence of WB revealed from our 1D model remains true under realistic modeling. In Fig. 4.5(c), we show the average DW velocity versus strain gradient for different widths of ferromagnetic strip. As it can be seen, the average velocity is not affected by the strip width, and good agreement with the 1D model is found. This confirms that the physics underlying DW motion under strain demonstrated by the 1D model is valid not only for narrow strips but for wide ones as well.

Fig. 4.5(d) shows the average DW velocity for the case where in-plane and perpendicular strain gradients are applied simultaneously to the system with a ratio $\beta = |\frac{\varepsilon'_{zz}}{\varepsilon'_{xx}}|$. As can be observed, micromagnetic simulation confirms the onset of turbulent DW motion at $\varepsilon'_{xx} = -0.077\mu\mathrm{m}^{-1}$ if both strain gradients are of the same magnitude ($\beta = 1$). However, the additional contribution of the ε'_{zz} increases the average DW velocity. The dynamics after the transient period explained in the previous section with the 1D model (where the DW recovers the steady motion) are not accessible via micromagnetic simulation because of the limitations to the strain magnitude explained above.

To sum up, our simulations show that high DW velocities can be achieved under realistic conditions, especially if we take into account that, as shown in our previous publications [125, 128], in-plane strain gradients in the order of $10^{-2}\,\mu\mathrm{m}^{-1}$ can be realized in hybrid ferromagnetic/piezoelectric devices by applying moderate voltages between conveniently located electrodes over the piezoelectric substrate.

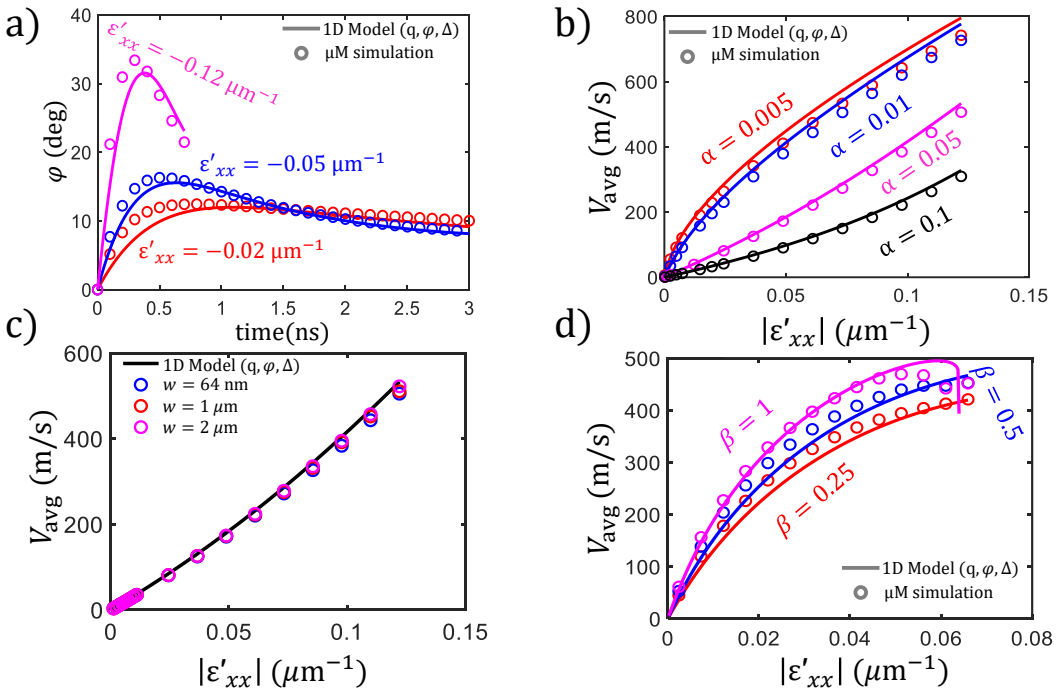

Fig. 4.5.: a) Time evolution of the DW angle φ for different values of the in-plane strain gradient (ε'_{xx}). b) Average DW velocity as a function ε'_{xx} for different values of the damping constant α. c) Average DW velocity for different strip widths under in-plane strain gradients and $\alpha = 0.05$. d) Average DW velocity as a function of the strain gradient for different values of the ratio between perpendicular an in-plane strain gradients $\beta = |\frac{\varepsilon'_{zz}}{\varepsilon'_{xx}}|$. In all graphs, micromagnetic results and the 1D results are shown by dots and lines respectively.

4.3 Conclusion

We studied the influence of strain on the statics and dynamics of DWs in ferromagnetic strip with perpendicular anisotropy. Our theoretical study shows that uniform strain can be used to tune the DW internal angle between Bloch and Neel configuration. It is also shown that DW dynamics driven by an in-plane strain gradient is qualitatively different from the response to other driving forces, such as external field, spin-polarized current or perpendicular strain gradients. In particular, such dynamics occurs without Walker breakdown and, ideally, a DW velocity proportional to the strain gradient is obtained regardless of the strain gradient magnitude. We show that the origin of this phenomenon lies in the fact that the DW internal angle in equilibrium depends on strain. This leads to a dynamic torque that opposes its tilting and whose strength increases as the DW moves towards increasingly strained regions, and prevents the onset of internal DW oscillations. On the other hand, the maximum DW velocity achievable with our approach is not limited by their intrinsic dynamic properties but on the feasibility of keeping perpendicularly magnetized domains stable in regions of high in-plane strain. In any case, our micromagnetic simulations show that averaged velocities in the order of $500\,\mathrm{m/s}$ can be achieved under realistic conditions easily achievable in experimental setups. These velocities are in the range of spin-orbit torques driven DW motion but they are reached with much less energy dissipation since Joule heating is absent. Furthermore, our system reveals complex dynamics where DW angle and, therefore, also its inertia, are not uniquely determined by its velocity but they can largely be tuned with strain, which opens a new avenue to explore dynamic phenomena.

5 Internal dynamics of domain walls driven by spin-orbit torques under uniform strain

In this chapter, we investigate the SOT-driven dynamics of Néel DWs stabilized via uniform in-plane (IP) mechanical strain using micromagnetic simulations and analytical models. We start by examining how DWs in narrow strips respond to an external current in the presence of uniform strain. We observe that, at a critical current value, the DW stops moving completely, remaining static even if we keep increasing the current. This phenomenon is linked to the effect of the precessional component of the SOT, which causes a gradual transition in the DW configuration from Néel to Bloch. With the aim of confirming whether these effects hold true in broader systems, we expand our study to wider strips. In this case, we again find that the DW stops moving beyond a certain threshold current, but this time its internal magnetization displays non-uniform patterns and non-linear dynamical regimes. To better understand the underlying physics governing this intricate DW behavior, we extend the 1D model to account for spatial variations of the DW components. We identify an internal twist with a $180°$-kink form, where the kink width depends on the ratio between exchange and magnetoelastic anisotropy. Simultaneously, we note distortions in the DW structure due to the competition between SOTs and exchange torque. We also delve into the factors influencing DW motion cessation. We found that this behavior originates from a balance between non-linear and dispersive effects in the system. The content of this chapter is the subject of a manuscript under preparation, which will be submitted in the next few months.

5.1 Introduction

We start this chapter reviewing some aspects of DWs already discussed in chapter 2 and introducing Vertical Bloch lines. As mentioned in Sec. 2.8.1, in presence of external stimuli such as spin-polarized currents or magnetic fields, DWs depict two dynamical regimes according to Walker's model [101]. The first one is called the

steady regime, where the DW moves with a constant velocity proportional to the external force strength. However, if this force exceeds a certain threshold value, the DW dynamics transits to a precessional regime where its internal magnetic moments oscillate continuously with a frequency proportional to the external force.

It has been shown that one-dimensional DWs in narrow strips depict uniform precessional dynamics where their internal magnetic moments oscillate coherently. In wide strips, however, the magnetic moments inside the DW oscillate non-uniformly, leading to highly nonlinear behaviors where the formation of complex space-dependent structures such as vertical Bloch lines (VBLs) typically takes place [193–196]. VBLs, which have been reported in both Bloch and Néel DWs, are curling structures characterized by a twist of the DW internal magnetization along its length [197]. In the absence of DMI, VBLs exhibit a four-fold degeneracy where four states with different chiralities $\left(C = \pm\frac{1}{2}\right)$ and magnetic charge $(Q = \pm 1)$ belong to the same energy level and exist with the same probability, as represented in Fig. 4.1. In this context, the magnetic charge (Q) quantifies the polarity of the domains surrounding the VBL. Specifically, a magnetic charge $Q = +1$ means a head-to-head VBL, while $Q = -1$ signifies a tail-to-tail one as sketched in Fig. 4.1. Additionally, positive chirality corresponds to a clockwise rotation of the magnetization, whereas negative chirality corresponds to an anticlockwise one. In absence of DMI, VBLs nucleate successively in pairs and propagate with the same velocity, leading to a pure precessional behavior similar to one-dimensional DWs. When DMI comes into play, the VBL energy level with 4-fold degeneracy splits into two distinct levels with 2-fold degeneracy each, which leads to the nucleation of VBLs with different energies along the DW. These structures subsequently move at different velocities and annihilate by collision, leading the DW to maintain a constant velocity above the threshold external magnetic field [198].

In this chapter, we investigate the dynamics of achiral Néel DWs stabilized via in-plane strains under SOTs in both narrow and wide strips. In the following, we will explore the dynamics of such DWs in narrow strips using both the 1D model and micromagnetic simulations. Then we will check these dynamics in a wider system by using an extended model that allows for the DW position and internal angle to vary along the width of the strip. Finally, we will summarize the findings of our work and present our conclusions.

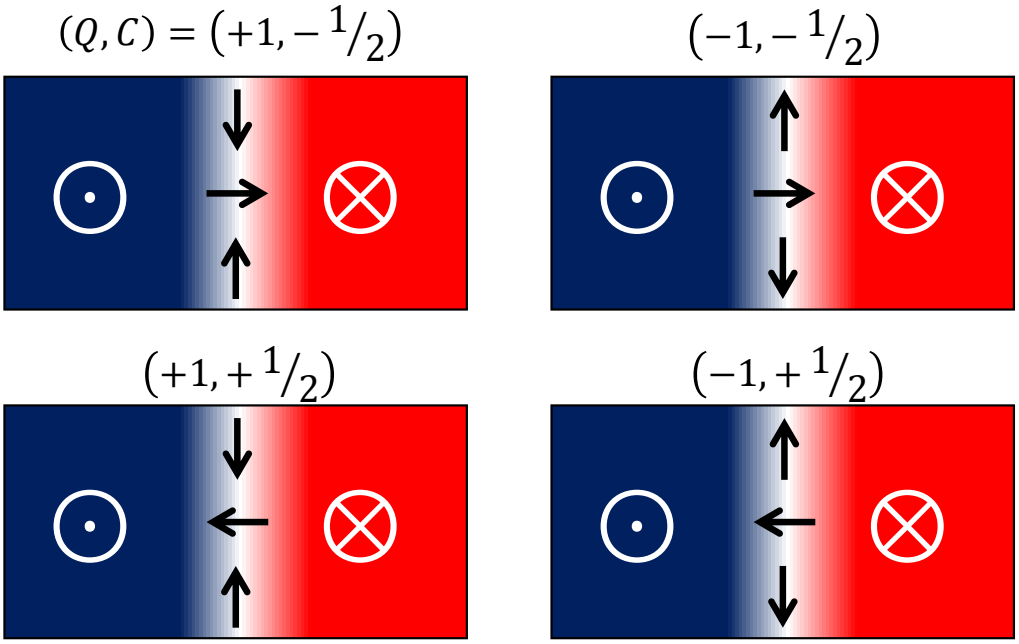

Fig. 5.1.: Four VBL structures with different magnetic charges Q and chiralities C.

5.2 SOT driven achiral Néel DW dynamics in narrow strips

The system under study is schematically represented in Fig. 5.2(a). It consists of a very long nanostrip of width W and thickness t_{FM} made of a ferromagnet with strong perpendicular anisotropy and a Néel DW located at the center. The ferromagnet is subject to a longitudinal uniform strain ε_{xx} strong enough to favor the Néel configuration over the Bloch one in the DW. Certainly, it was recently shown [187] that by inducing a sufficiently strong in-plane anisotropy, it is possible to stabilize Néel DWs in absence of interfacial DMI and we demonstrated in chapter 4 that this can be achieved using longitudinal strain ε_{xx} [159]. As indicated in Fig. 5.2(a), our DW is also subject to a SOT induced by an electric current density J_{HM} flowing through an adjacent heavy metal underneath that pushes the DW along the $+x$ direction.

Micromagnetic simulations are carried out with mumax3 [100] for a nanostrip of length $L = 1024\,\mathrm{nm}$, thickness $t_{\mathrm{FM}} = 1\,\mathrm{nm}$ and variable width W using $1\,\mathrm{nm}$ cubic cells for the discretization. The following magnetic and elastic material parameters were used in our study: $A_{\mathrm{ex}} = 20\,\mathrm{pJ/m}$ (exchange stiffness), $M_{\mathrm{s}} = 0.58\,\mathrm{MA/m}$ (saturation magnetization), $K_{\mathrm{u}} = 0.9\,\mathrm{MJ/m^3}$ (uniaxial anisotropy),

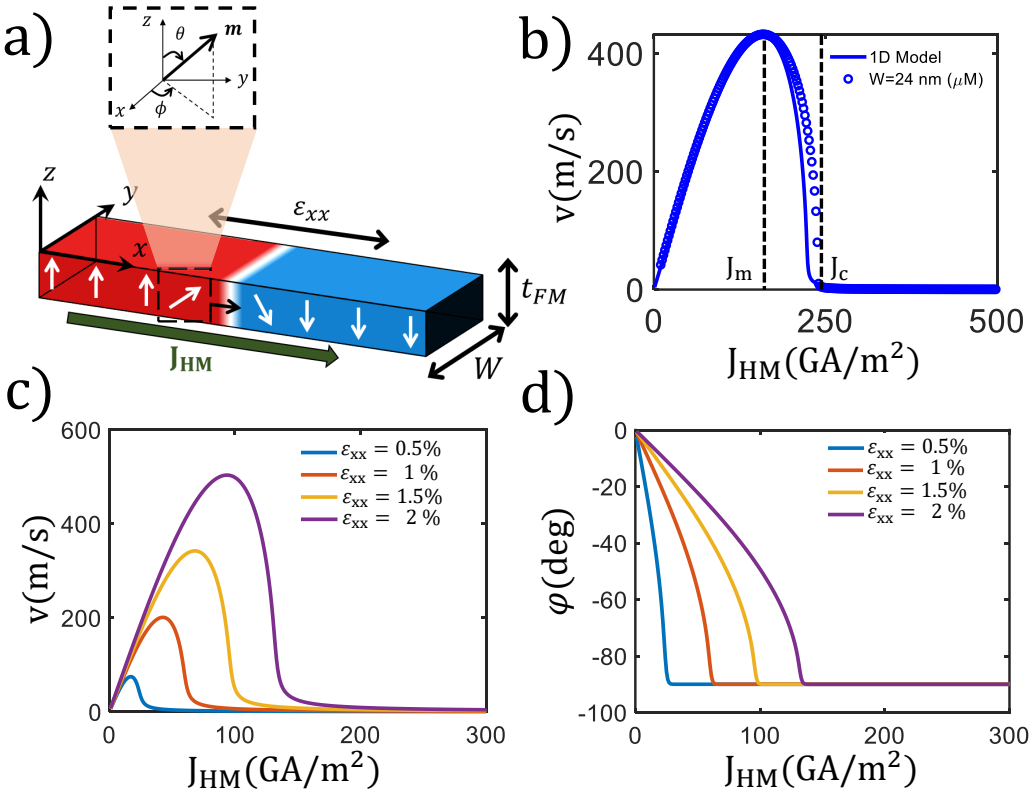

Fig. 5.2.: a) Schematic representation of the system under study. A Néel DW is located at the center of an ferromagnetic nanostrip subject to a uniform strain and a spin-curent generated through spin-Hall effect. b) DW average velocity versus applied current computed after a 50 ns time window from both μM simulations (dots) and the 1D model (solid line). c) DW average velocity versus applied current computed after a 50 ns time window from the 1D model under different IP strains ε_{xx}. d) Steady state DW angle versus applied current for different values of the IP strain ε_{xx}.

$\alpha = 0.08$ (Gilbert damping), $\theta_{\rm sh} = -0.33$ (spin Hall angle), $D = 0$ (DMI constant), $\lambda_{\rm s} = -5 \times 10^{-5}$ (magnetostrictive coefficient), $C_{11} = 218\,\mathrm{GPa}$ and $C_{12} = 133\,\mathrm{GPa}$ (elastic constants).

Let us first focus on the SOT dynamics of our Néel DWs in narrow strips. We consider the ferromagnet in Fig. 5.2(a) with $W = 24\,\mathrm{nm}$ and we develop a 1D model using a similar approach as presented in Sec. 2.8.1. The dynamic equations in this case read

$$\frac{\dot{q}}{\Delta} = -\alpha\Gamma_{\rm SOT} + \Gamma_{\rm AN} \tag{5.1}$$

$$\dot{\varphi} = -\Gamma_{\rm SOT} - \alpha\Gamma_{\rm AN} \tag{5.2}$$

with

$$\Gamma_{\rm SOT} = \frac{\gamma_0}{1+\alpha^2}\frac{\pi}{2}H_{\rm SOT}\cos\varphi$$
$$\Gamma_{\rm AN} = \frac{\gamma_0}{1+\alpha^2}H_{\rm AN}\sin 2\varphi$$

Eq.(5.1) and (5.2) describe the evolution of the DW position q and its internal angle φ over time, respectively. The functions $\Gamma_{\rm SOT}(\varphi(t))$ and $\Gamma_{\rm AN}(\varphi(t))$ denote the torques associated with the spin current and the in-plane anisotropy, respectively, where $H_{\rm SOT} = \frac{\hbar\theta_{\rm sh}\mathrm{J_{HM}}}{2e\mu_0 M_{\rm s}\ell_z}$ and $H_{\rm AN} = \frac{H_{\rm sh}}{2} - H_{\rm mel}\varepsilon_{xx}$, with $H_{\rm sh} = M_{\rm s}\,(N_y - N_x)$ being the shape anisotropy field and $H_{\rm mel} = \frac{B_1}{\mu_0 M_{\rm s}}$ the magnetoelastic anisotropy field.

Fig. 5.2(b) shows the average DW velocity computed over a time window of $50\,\mathrm{ns}$ from both micromagnetic simulations (μM) and the 1D model. It can be observed that, below a certain threshold current density ($\mathrm{J_m}$), the DW velocity scales quasi-lineally with the applied current. However, beyond $\mathrm{J_m}$, the DW velocity starts decreasing gradually until it fully vanishes at a certain current density $\mathrm{J_c}$ and remains unchanged if the current density keeps increasing. In Fig. 5.2(c), we show the average DW velocity versus current for different values of the strain ε_{xx}. It can be noted that the threshold current above which the DW velocity vanishes is gradually increased while raising the strain value. This increase allows for enhanced maximum DW velocity since one can inject higher currents before the DW stops.

In the same context, the 1D model allows us to quantify the DW angle and velocity at the steady state, as well as the threshold currents over which the DW velocity starts decreasing and stops. Solving Eq. (5.1) for $\dot{\varphi} = 0$ yields

$$\varphi_{\mathrm{s}} = \arcsin\left[\frac{\pi\hbar\theta_{\mathrm{sh}}\mathrm{J_{HM}}}{8\,\alpha\,e\,t_{\mathrm{FM}}(\frac{K_{\mathrm{sh}}}{2} - B_1\varepsilon_{xx})}\right] \tag{5.3}$$

if the current is smaller then the critical one ($\mathrm{J_{HM}} < \mathrm{J_c}$). Above this critical current a Bloch wall is found ($\varphi = \pm\frac{\pi}{2}$). Note that $K_{\mathrm{sh}} = \frac{1}{2}\mu_0 M_{\mathrm{s}} H_{\mathrm{sh}}$.

Substituting Eq. (5.3) in Eq. (5.1) gives the DW velocity at the steady state

$$|\mathrm{v_s}| = \frac{\gamma_0\Delta\pi\hbar|\theta_{\mathrm{sh}}|}{4\alpha\,|e|\,t_{\mathrm{FM}}\,\mu_0\,M_{\mathrm{s}}}|\mathrm{J_{HM}}|\sqrt{1 - \left(\frac{\pi\hbar|\theta_{\mathrm{sh}}|}{8\alpha\,|e|\,t_{\mathrm{FM}}(\frac{K_{\mathrm{sh}}}{2} - B_1\varepsilon_{xx})}\right)^2|\mathrm{J_{HM}}|^2} \tag{5.4}$$

if the current is bellow the critical one $\mathrm{J_{HM}} < \mathrm{J_c}$. Above this critical current, $|\mathrm{v_s}| = 0$.

The critical currents, $\mathrm{J_c}$ and $\mathrm{J_m}$, can be determined from Eq.(5.4) by respectively imposing $|\mathrm{v_s}| = 0$ and $\mathrm{d}|\mathrm{v_s}|/\mathrm{dJ_{HM}} = 0$

$$|\mathrm{J_c}| = \frac{8\alpha|e|t_{\mathrm{FM}}(\frac{K_{\mathrm{sh}}}{2} - B_1\varepsilon_{xx})}{\pi\hbar|\theta_{\mathrm{sh}}|} \tag{5.5}$$

$$|\mathrm{J_m}| = \frac{1}{\sqrt{2}}|\mathrm{J_c}| \tag{5.6}$$

The DW velocity shown in Fig. 5.2 is a direct consequence of the changes that its internal angle undergoes. This becomes evident from Eq. (5.3), where it is analytically shown that, if $\mathrm{J_{HM}}$ overcomes $\mathrm{J_c}$, the DW changes to a Bloch configuration with $\varphi = -\frac{\pi}{2}$. This DW angle behavior is depicted in Fig. 5.2(d), where we can see how the increase of the applied current changes gradually the DW angle from $\varphi = 0$ to $\varphi = -\frac{\pi}{2}$.

To understand the physical mechanism behind this behavior, let us analyze the DW dynamics depicted in Fig. 5.2 in terms of the torques involved in Eq. (5.1) and Eq. (5.2). Once the applied current is turned on, the damping component of SOT ($\alpha\Gamma_{\mathrm{SOT}}$) triggers the DW displacement along x-axis. Simultaneously, its corresponding precessional component (Γ_{SOT}) tilts the internal DW angle away from its equilibrium ($\varphi = 0$). The tilt of the DW angle strengthens the damping in-plane anisotropy torque ($\alpha\Gamma_{\mathrm{AN}}$), which starts competing with Γ_{SOT} trying to bring the DW angle back to its equilibrium. As long as the applied current is below the threshold $\mathrm{J_c}$, these torques balance each other, leading the DW angle to reach a steady state value according to Eq. (5.3). Afterwards, the DW velocity reaches

a constant value that only depends on the applied current and the in-plane strain, as displayed in Eq. (5.4). Once the applied current surpasses the threshold, Γ_{SOT} becomes dominant and brings the DW angle to the Bloch configuration ($\varphi = -\frac{\pi}{2}$), which cancels out all the torques acting on the DW, leading it to a complete stop. This DW behavior was also recently reported for bistable Néel DWs stabilized via shape anisotropies in narrow strips depicting a uniform internal DW configuration along the transverse direction [199].

5.3 SOT driven achiral Néel DW dynamics in wide strips

5.3.1 Achiral Néel DW dynamics in wide strips

Let us focus now on investigating the DW dynamics in wider strips with the aim of checking whether the behavior observed in Sec. 5.2 is universal. To do so, we keep the system as in Fig. 5.2(a) with the same material parameters but now with a variable width W.

Fig. 5.3(a) shows the DW velocity versus applied current obtained from μM simulations for strips with different widths plotted together with the prediction of the 1D model Eq. (5.4). As can be observed, the 1D model predicts that the DW velocity initially increases with current up to approximately $160\,\mathrm{GA/m^2}$ and then it starts decreasing gradually until it becomes null when $\mathrm{J_{HM}}$ reaches $240\,\mathrm{GA/m^2}$, remaining immobile for larger current values. As explained in Sec. 5.2, this behavior is due to the fact that by increasing the current, the DW internal angle gradually tilts from a Néel ($\varphi = 0, \pi$) to a Bloch configuration ($\varphi = \pm\frac{\pi}{2}$), which makes SOT increasingly inefficient to move the DW [107]. A very similar behavior is obtained from μM simulations for the narrowest nanostrip ($W = 24\,\mathrm{nm}$), which indicates that the DW behaves like a rigid 1D object in this case. For the other cases, however, the initial regime of increasing velocity remains practically unchanged, but instead of getting a gradual decreasing regime, the DW abruptly comes to a complete stop when a certain critical current $\mathrm{J_c}$ is reached, which is a clear indication that the DW deviates from the 1D behavior. This becomes obvious if one looks at Fig. 5.3(b), where we show typical snapshots of the magnetization for three different widths and an applied current above $\mathrm{J_c}$. They correspond to the steady state once the DW stops and, as it can be observed, in the three cases the DW presents a regular undulating structure consisting of a concatenation of segments of the same curvature but of alternating sign. In the enlarged area, we present a detailed view of the transition region separating two consecutive segments magnetized along positive $+x$ (top) and

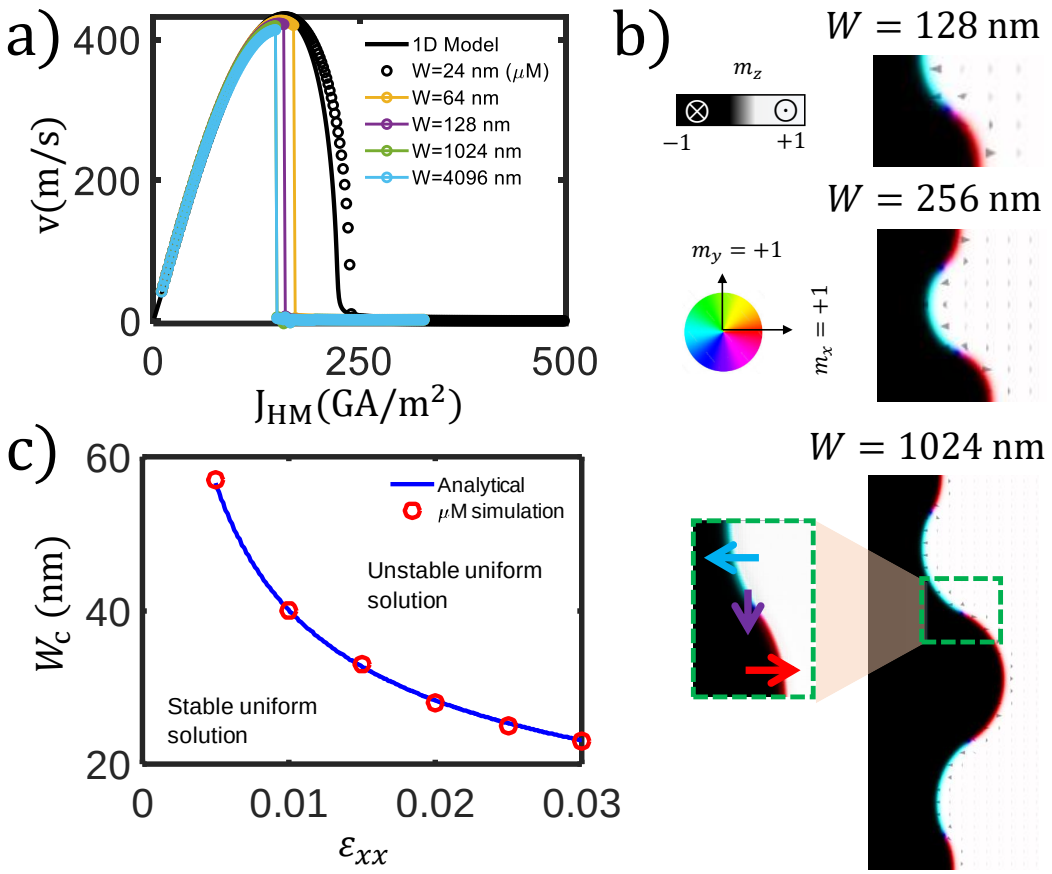

Fig. 5.3.: a) DW average velocity versus applied current from μM simulations for strips with different widths together with the 1D model prediction. b) Micromagnetic snapshots of the DW structure at the steady state for strips with different widths. The inset shows a magnification of the magnetization inside the DW. c) Critical width for unstable linear solution versus the in-plane strain from both micromagnetic simulation and a linear stability analysis of Eq.(5.9) and Eq.(5.10). The blue curve was obtained form Eq. (A.65) and the LSA was detailed in Appendix. A.4.2.

$-x$ (bottom) directions, respectively.In the transition region, which extends only over a few nanometers, the magnetization points along the $-y$ direction. Though these structures belong to the Bloch lines (BL) family, they have different features, as will be discussed later in this chapter. Hence, in what follows, we will refer to them as $kinks$ for the sake of simplicity.

5.3.2 Extended collective coordinates model and steady state DW structure

Considering the structures shown by the DWs (Fig. 5.3(b)), and with the aim of understanding their features and the dynamic processes that lead to them, we

generalize the 1D model mentioned previously in Sec. 5.2 allowing both DW coordinates q and φ to vary along the y-axis. To do so, we used a modified Walker ansatz [101] to include the space variation of both the DW position $q(t,y)$ and its internal angle $\varphi(t,y)$ as follows

$$\begin{cases} \theta(x,y,t) = 2\tan^{-1}\left(e^{\frac{x-q(y,t)}{\Delta}}\right) \\ \phi(x,y,t) = \varphi(y,t) \end{cases} \tag{5.7}$$

where θ and ϕ are the spherical coordinates of the magnetization as sketched in Fig. 5.2(a).

Plugging this new ansatz in the energy density Eq. (2.22) and integrating it along x-axis yields the DW energy density per unit surface as

$$\begin{aligned} \mathcal{U}_{\text{DW}} = A_{\text{ex}}\left[\frac{2}{\Delta} - \frac{4}{\Delta}\frac{\mathrm{d}q(y,t)}{\mathrm{d}y} + \frac{2}{\Delta}\left(\frac{\mathrm{d}q(y,t)}{\mathrm{d}y}\right)^2 + 2\Delta\left(\frac{\mathrm{d}\varphi(y,t)}{\mathrm{d}y}\right)\right] + 2\Delta K_{\text{eff}} \\ + 2\Delta K_{\text{sh}}\sin^2(\varphi(y,t)) + 2\Delta B_1\varepsilon_{xx}\cos^2(\varphi(y,t)) \end{aligned} \tag{5.8}$$

Using Eq. (5.8) together with LLG equation Eq.(2.41) and following the procedure developed in Appendix. A.4 we get two partial differential equations describing the DW dynamics as

$$(1+\alpha^2)\partial_t\frac{q}{\Delta} = \alpha\mathcal{D}\partial_{yy}\frac{q}{\Delta} - \alpha\Gamma_{\text{SOT}} - \mathcal{D}\partial_{yy}\varphi + \Gamma_{\text{AN}} \tag{5.9}$$

$$(1+\alpha^2)\partial_t\varphi = \mathcal{D}\partial_{yy}\frac{q}{\Delta} - \Gamma_{\text{SOT}} + \alpha\mathcal{D}\partial_{yy}\varphi - \alpha\Gamma_{\text{AN}} \tag{5.10}$$

where $\mathcal{D} = \frac{2\gamma_0 A_{\text{ex}}}{\mu_0 M_{\text{s}}}$ is a dispersive-like constant, $\Gamma_{\text{SOT}} = \frac{\gamma_0\pi}{2}H_{\text{SOT}}\cos\varphi$ is the SOT torque and $\Gamma_{\text{AN}} = \gamma_0 H_{\text{AN}}\sin 2\varphi$ is the in-plane anisotropy torque. Note that the partial derivatives are represented as $\partial_i \equiv \frac{\partial}{\partial i}$, where i stands for the variable with respect to which we are performing the differentiation.

In order to confirm whether our model captures the behavior observed in μM simulations, we check the stability of the steady state solutions of Eq. (5.9) and Eq. (5.10) for $\mathrm{J_{HM}} > \mathrm{J_c}$. For that purpose, we carry out a linear stability analysis (LSA) of the two PDEs of our model, Eq. (5.9) and Eq. (5.10), as detailed in Appendix. A.4. The LSA unveils that, at a critical width $W_{\text{c}} = \pi\sqrt{\frac{A_{\text{ex}}}{K_{\text{sh}} - B_1\varepsilon_{xx}}}$ (see Eq. (A.65)), a stationary bifurcation takes place, where the uniform solution ($q = cst$

and $\varphi_s = -\frac{\pi}{2}$) becomes unstable and, instead, space-dependent patterns will appear as illustrated in Fig. 5.3(b). This behavior is clearly displayed in Fig. 5.3(c), where we plot the critical width W_c versus the applied strain from both the model and μM simulation. Interestingly, both approaches agree on predicting the phase boundary, separating the pure 1D DW behavior from the intricate 2D behavior observed for the largest widths in Fig. 5.3(b).

Once we have a clear proof that our model captures the main features exhibited by DW in 2D strips, let us explore its steady state structure when $\mathrm{J_{HM}} > \mathrm{J_c}$. With this aim, we impose equilibrium conditions ($\partial_t \frac{q}{\Delta} = 0$ and $\partial_t \varphi = 0$) to Eqs. (5.9) and (5.10) and solve them analytically to get both the space-dependent DW angle $\varphi(y)$ and position $q(y)$ at the steady state as

$$\varphi(y) = 2\tan^{-1}\left[e^{\frac{-Qy}{\lambda}}\right] \tag{5.11}$$

$$q(y) = \frac{\Omega}{2}y^2 + \frac{\Omega r}{2}y + \frac{\Omega}{2}\lambda^2 Li_2\left(-e^{\frac{2y}{\lambda}}\right) + \frac{\Omega}{24}\pi^2\lambda^2 \tag{5.12}$$

where $\lambda = \sqrt{\frac{A_\mathrm{ex}}{K_\mathrm{sh} - B_1\varepsilon_{xx}}}$ is the kink width, $Q = \pm 1$ denotes the orientation of the in-plane magnetization around the kink, $\Omega = -Q\frac{\pi\Delta\hbar\theta_\mathrm{sh}\mathrm{J_{HM}}}{8|e|A_\mathrm{ex}t_\mathrm{FM}}$ and $Li_2(x)$ is the Spence's function (Dilogarithm) [200].

Fig. 5.4(a) and Fig. 5.4(b) show the transverse component of internal DW magnetization $m_y = \sin\varphi(y)$ and position $q(y)$ along y-axis for $W = 256\,\mathrm{nm}$ and $\mathrm{J_{HM}} = 200\,\mathrm{GA/m^2}$ obtained from both μM simulations, Eq. (5.11) and Eq. (5.12), respectively. As can be perceived from the two figures, both μM simulation and the model agree on predicting the steady state of the DW internal structure. Remarkably, the internal twist of the DW takes the form of a $180°$-kink where the DW internal magnetization at the kink transition is always pointing towards the $-y$ direction (i.e. $\varphi(y) = -\frac{\pi}{2}$) as one can also confirm from Fig. 5.4(b). This orientation is a direct consequence of the SOT, which forces the magnetization in the kink to point alongside its corresponding effective field, $\mathbf{H}_\mathrm{SOT}$. This phenomenon results in a two-fold degeneracy within the system. Specifically, it allows for only two possible orientations of magnetization around the kink: either transitioning from an "$+x$" orientation to a "$-x$" one ($\uparrow\rightarrow\downarrow$) or vice versa ($\downarrow\rightarrow\uparrow$). On the other hand, when examining the DW position $q(y)$, we observe that the DW shifts in opposite directions around the center of the kink. This behavior is attributed to the fact that the force exerted by the SOT points in opposite directions on both sides of the

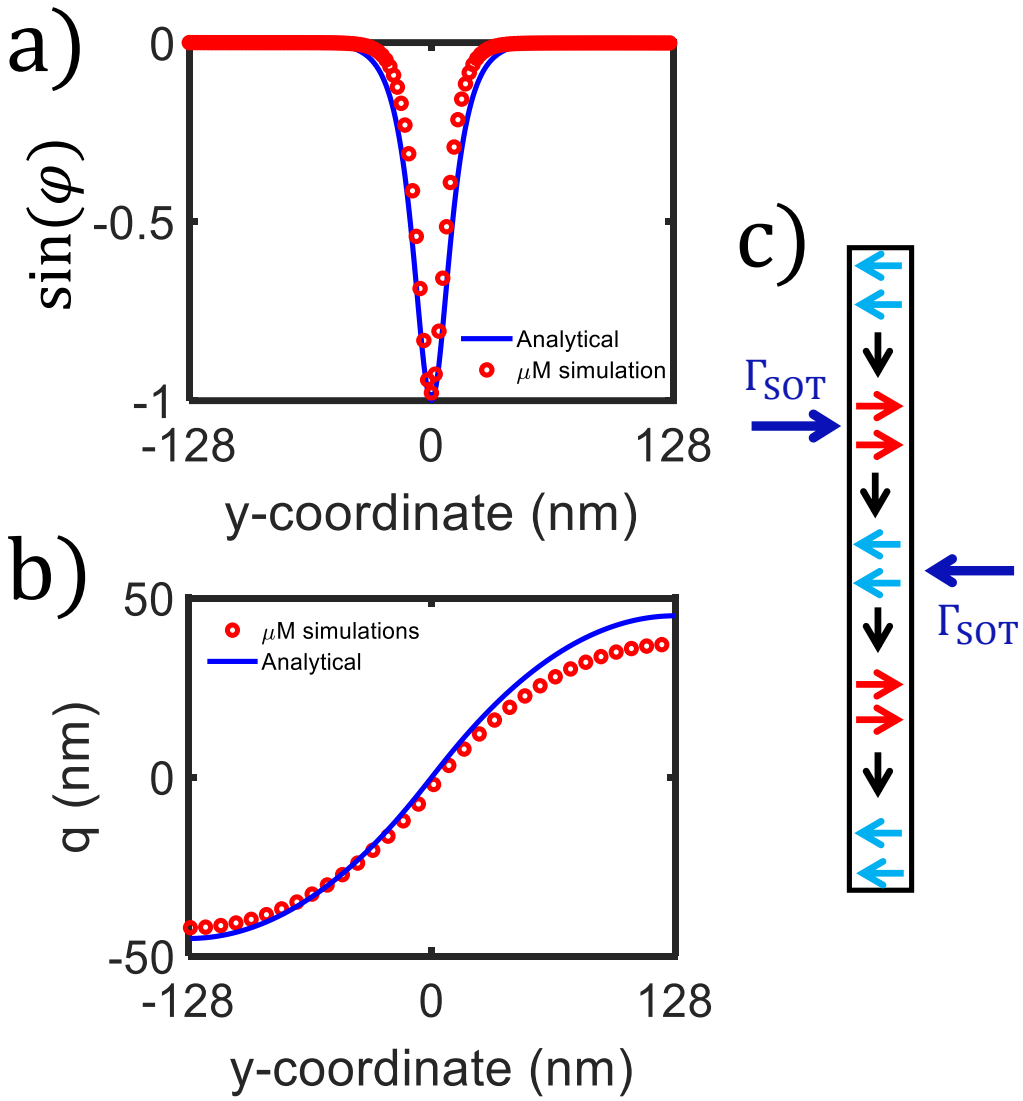

Fig. 5.4.: a) The transverse magnetization $m_y = \sin\varphi(y)$ along y-axis from both Eq.(5.11) and μM simulation with $W = 256$ nm, $J_{HM} = 200\,GA/m^2$ and $\varepsilon_{xx} = 2\%$. b) DW displacement along $y-$axis from both Eq. (5.12) and μM simulation with $W = 256$ nm and $\varepsilon_{xx} = 2\%$. c) Schematic representation of the SOT acting along the DW within regions of different magnetization orientations.

kink, as schematized in Fig. 5.4(c). Hence, it experiences a stretching effect where the inversely in-plane-oriented parts of the DW move in opposite directions. We can anticipate from Eq. (5.12) that the amount of DW stretching is a compromise between the SOT and exchange, which becomes evident as $\Omega \propto \frac{\mathrm{J_{HM}}}{A_{\mathrm{ex}}}$. This predicts the crucial role that the DW elasticity is poised to play on its structure and stability, as we will explore in the following section.

5.3.3 Transient dynamics and kinks stabilization

After examining the DW steady state structure and unveiling the main features of the nucleated kinks, let us now focus on understanding the transient regime, including their nucleation. As described previously in Sec. 5.3.1, the achiral Néel DW stops under SOT if the applied current $\mathrm{J_{HM}}$ is above a certain threshold. This phenomenon is related to the nucleation of magnetic kinks inside the DW, which is initially triggered by the precessional component of the SOT (Γ_{SOT}). Hence, when $\mathrm{J_{HM}}$ is above the threshold $\mathrm{J_c}$, Γ_{SOT} becomes important, leading the internal spins of the DW to rotate away from their equilibrium ($\varphi(y) = 0, \pi$) as shown in Fig. 5.5, where we plot all the torques involved in Eq. (5.10) as a function of y at different time instants. Due to the inhomogeneity of the demagnetizing field near the DW boundary [189], its internal spins there rotate with different angular velocities with respect to the ones located far from the strip edge, as schematized in Fig. 5.5(b). As soon as neighboring spins in an arbitrary region along the DW start exhibiting a large non-colinearity (see Fig. 5.5(b)), the one with the largest tilting reverses, leading to the nucleation of kink pairs as schematized in Fig. 5.5(c). When the first kink pairs appear, the nucleation spreads along the DW due to the precessional dispersive-like torque ($\mathcal{D}\partial_{yy}\frac{q}{\Delta}$). This becomes evident in Fig. 5.5(c), where it can be seen that this torque is the dominant one.

Right after the nucleation regime, the kinks start evolving slowly towards a steady state by moving and annihilating via kink-kink or kink-edge collisions. The post-nucleation regime is found to be much slower compared to the nucleation one. While the nucleation time is around $t_{nucl} = 0.1\,\mathrm{ns}$ the time required to reach the final state varies in the range $t_f = 1 - 100\,\mathrm{ns}$ depending on the strip width. This is ascribed to the fact that after nucleating the kinks over the DW, the precessional SOT (Γ_{SOT}) and dispersive-like ($\mathcal{D}\partial_{yy}\frac{q}{\Delta}$) torques compensate each other. Afterwards, the dynamics of $\varphi(t, y)$ is essentially associated with the damping contributions of the exchange dispersive-like torque ($\alpha\mathcal{D}\partial_{yy}\varphi$) and IP anisotrpy one ($\Gamma_{\mathrm{AN}}$), both of which are considerably smaller, as evidenced by the torques plot in Fig. 5.5(b). These findings anticipate that the number of kinks at nucleation is not necessarily

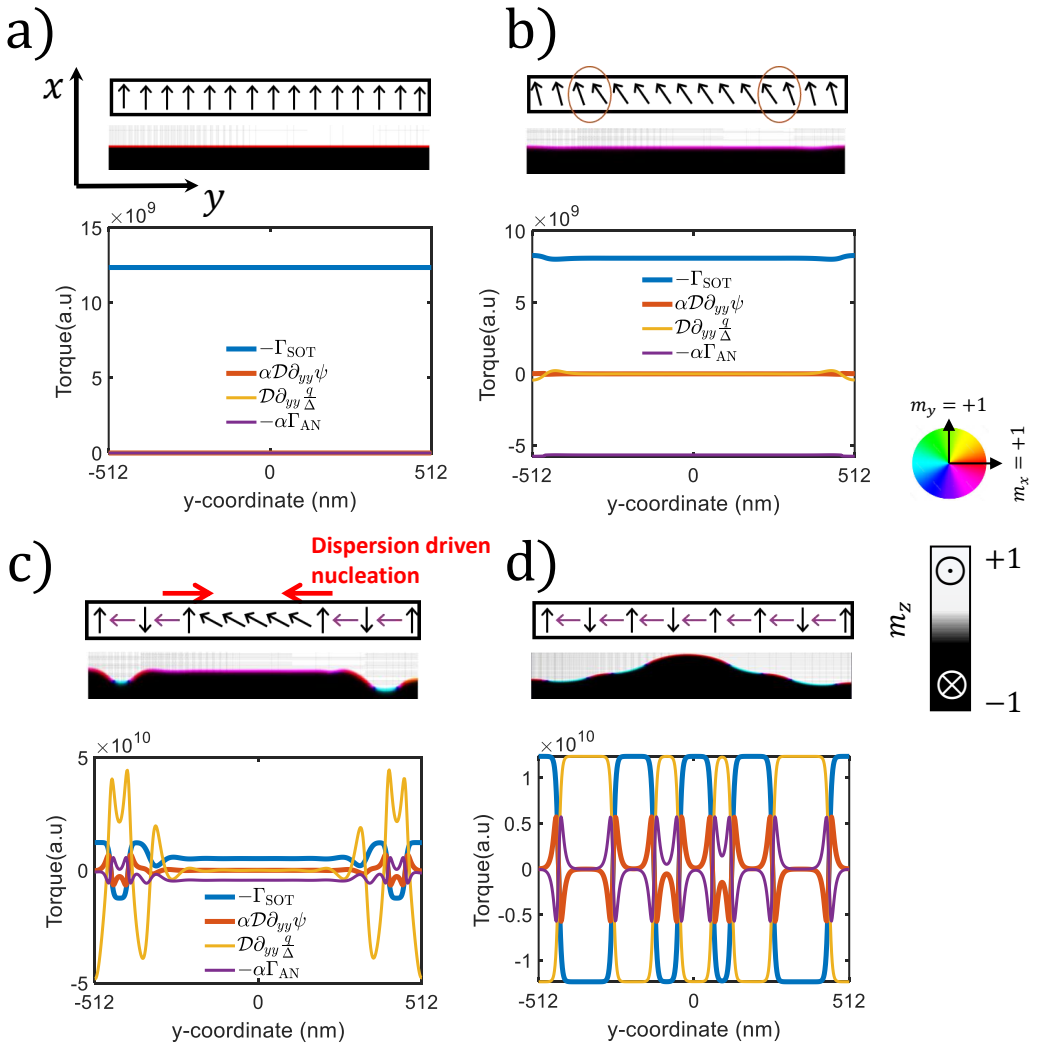

Fig. 5.5.: Sketch of the internal DW structure together with its corresponding micromagnetic snapshot and a plot of the space distribution of various torques involved the dynamics of $\varphi(t, y)$ as presented in Eq. (5.10) for: a) t=0 ns when the current is turned on. b) t= 0.01 ns when the spins along the DW starts tilting from their equilibrium positions due to SOT. c) t=0.3 ns where the first kink pairs are nucleated. d) t=1 ns when the nucleation has spread along the DW.

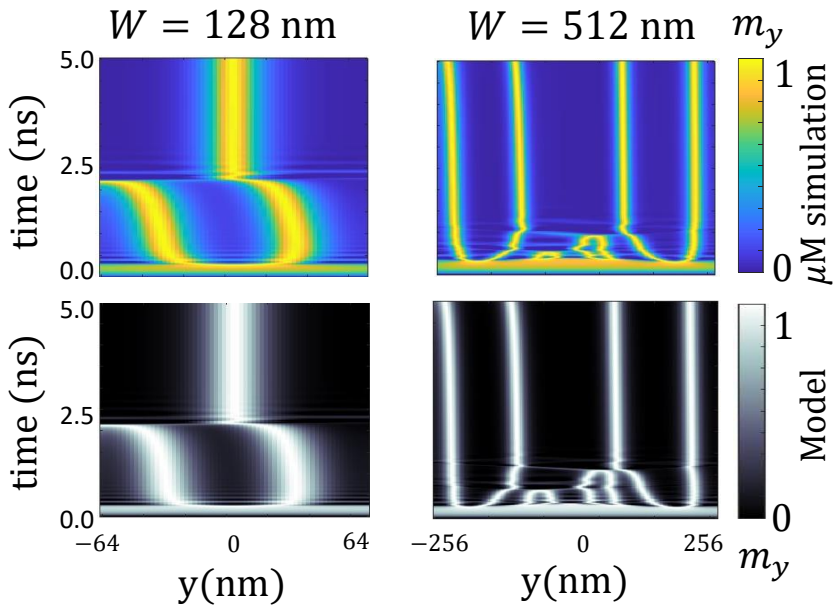

Fig. 5.6.: Spatio-temporal diagrams of the magnetization inside the DW from both μM simulation and the numerical solution of the model (Eq. 5.9 and Eq. 5.10) for an applied current $J_{HM} = 175\,GA/m^2$ and two different widths $W = 128$ nm (left panel), $W = 512$ nm (right panel).

equivalent to their number at the final state. A confirmation of such a claim is in Fig. 5.6, where the time evolution of m_y along the DW is shown for two systems with different widths (W). The discrepant time scales between the nucleation and relaxation regimes lead to first nucleating a given number of kinks, which causes the precessional torques to compensate for each other (see Fig .5.5(d)). Afterwards, these kinks evolve slowly, undergoing annihilation and eventually reaching a final state where all the torques are balanced. This reveals the difference between the physical mechanism upon which the DW stops in the narrow and wide strip cases. While in a quasi-1D system the DW stops because all the torques vanish, in wider strips the DW stops due to a local balance between the dispersive, spin-orbit, and the anisotropy torques.

Let us now examine the dependence of the number of kinks (k) at the final state on the strip width (W) and the applied current (J_{HM}). Fig. 5.7(a) shows k in the steady state versus the applied current for different widths. As can be remarked, for a fixed current, the number of kinks increases with W. Similarly, by increasing the current for a fixed width steps appear in which the number of kinks increases by one. To gain more insight into this behavior, let us examine how the DW length (see Fig. 5.7(b)) changes when we increase the applied current. To do so, we compute the DW length using the following formula

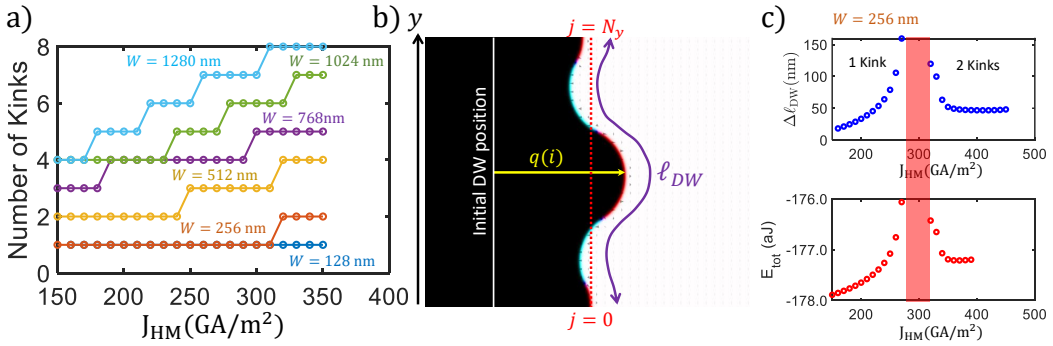

Fig. 5.7.: a) Number of kinks k at the steady or quasi-steady states versus applied current for strips with different widths computed via μM simulations. b) Sketch of the DW length and the relevant parameters to compute it. c) DW elongation ($\Delta\ell_{DW} = \ell_{DW} - W$) and total energy E versus current for a strip width $W = 256$ nm computed via μM simulations.

$$\ell_{DW} = \int_0^W \sqrt{1 + \left(\frac{\mathrm{d}q(y)}{\mathrm{d}y}\right)^2}\,\mathrm{d}y \tag{5.13}$$

In Fig. 5.7(c), we show both the DW elongation ($\Delta\ell_{DW} = \ell_{DW} - \ell_0$ where, $\ell_0 = W$ is the DW length at rest) as well as its total energy when the system passes from one to two kinks as J_{HM} increases for $W = 256\,\mathrm{nm}$. It can be observed that the appearance of a new kink inside the DW is anticipated by a significant DW elongation and a drastic increase of its energy. This behavior is ascribed to the DW surface pressure, which is enhanced when more kinks come into play since the DW local curvature radius is reduced [201–203]. It is worth mentioning that the transition from a k number of kinks to $k + 1$ could be accompanied by a critical regime (red shaded region in Fig. 5.7(c)) where the DW becomes unstable and undergoes more intricate non-linear dynamics, which is out of the scope of the present chapter.

5.4 Conclusion

To sum up, we have explored the SOT-driven dynamics of magnetic Néel DWs stabilized by uniform IP strain through micromagnetic simulations and analytical models. Initially, we investigated how DWs in narrow magnetic strips respond to externally applied current. Our findings revealed that, at a critical current value, the DW reaches a complete halt, remaining static irrespective of the applied current strength. This phenomenon is primarily attributed to the SOT precessional component, leading to a gradual transition in the DW configuration from Néel to Bloch, which are insensitive to SOTs. Expanding our investigation to wider strips, we observed a similar cessation of DW displacement beyond a specific threshold current. However, in this case, the internal magnetization of the DW exhibited a twist along the transverse direction. To gain deeper insights into the underlying physics governing this intricate DW behavior, we extended the collective coordinates 1D model to account for spatial variations of the DW variables along y-axis. This model extension allowed us to identify an internal twist characterized by a $180°$-kink structure, where the kink width is found to depend on exchange interactions and magnetoelastic anisotropy. Additionally, we observed distortions in the DW structure due to the competition between SOTs and exchange torques. Furthermore, our investigation revealed that the cessation of DW displacement in wide strips is the result of a balance between non-linear and dispersive effects.

Conclusions and Perspectives

6

This thesis was devoted to exploring the effects of mechanical strain on the static and dynamic properties of magnetic textures, namely DWs and skyrmions. The work has been carried out using micromagnetic simulation and a set of analytical models.

We started by exploring the effect of in-plane strain gradients on the current-driven skyrmion dynamics. In this part, we demonstrated that such strain gradients can be used to control the skyrmion motion in a versatile way, allowing for the displacement of the skyrmion in different directions. Furthermore, we showed that this approach can be used to minimize the skyrmion Hall effect, enabling the straight motion of skyrmions along the tracks. We also demonstrated that our approach works efficiently under realistic conditions, such as the presence of structural disorder. Finally, we proposed that strain gradients can be used in narrow magnetic racetracks to rectify skyrmion trajectories and raise the threshold current beyond which skyrmions are annihilated at the track boundaries. Our proposed approach for controlling current-driven skyrmions holds significant potential due to its versatility. Looking ahead, our perspective is centered on exploring the experimental feasibility of this method, and the possibilities to use it for logic and neuromorphic computing devices.

We also investigated the effects of both uniform and space-dependent strain on static and dynamic properties of DWs in PMA systems. First, we demonstrated that uniform strain can be used to switch between Néel and Bloch DWs. Later on we showed that space-dependent strain can be used to drive DW dynamics without magnetic fields or spin-polarized currents. We found that in-plane strain gradients trigger a special DW dynamics where Walker breakdown does not take place. This effect was explored via both micromagnetic simulations and the 1D model, which both agreed on predicting the absence of turbulent DW dynamics.

Additionally, we explored the SOT-driven dynamics of Néel DWs stabilized via in-plane strain. This study was divided into two parts. On one hand, in narrow ferromagnetic strips, we found that, beyond a threshold current, the DW stops moving and remains static since SOT switches its internal structure from Néel to Bloch configuration. On the other hand, in wide strips, the DW was found to

depict the same behavior, with the peculiarity that its internal structure exhibits non-uniform patterns and more intricate transient dynamics. This behavior was understood with an extended model that includes both space and time variations of the DW coordinates. Such a model revealed that, in wide strips, the DW stops due to a precise balance between the different torques involved, dispersive exchange, spin-orbit, anisotropy and magnetoelastic. If such a balance is broken, intricate non-linear dynamical regimes take place, including dissipative solitons. As a perspective, we aim to further explore this dynamical regimes and the mechanisms behind their existence.

In addition to the research work presented in this thesis manuscript, the author actively engaged in a close collaboration with experimental researchers and made significant contributions to several research projects through modeling and simulation. These collaborative works were conducted as part of the MagnEFi ITN. Among them we highlight the following:

- In collaboration with Sensitec Gmbh and Johannes Gutenberg University, we experimentally demonstrated that the DW injection from a nucleation pad to a magnetic nanowire can be improved by using a uniform in-plane strain. By performing micromagnetic simulations, we were able to explain this improved injection in terms of the effective anisotropy. This anisotropy influences the switching in the nucleation pad as well as the pining at the nanowire entrance [204].

- In collaboration with Eindhoven University of Technology, we experimentally demonstrated field-free SOT switching of a SAF through the introduction of interlayer Dzyaloshinskii-Moriya interactions. Including the new interlayer DMI contribution to our micromagnetic simulation, we were able to effectively explain the physical mechanism behind this switching and evidence its origin [205].

- In a second collaboration with Sensitec Gmbh and Johannes Gutenberg University, we proposed and evaluated an inexpensive and CMOS-compatible method to locally apply strain on a Si/SiOx substrate. Using Kerr microscopy, we experimentally demonstrated how the magnetoelastic energy landscape, created by a pair of openings in a magnetic nanowire, enables the creation of pinning sites for in-plane vortex walls that propagate in a magnetic racetrack. These observations were explained via micromagnetic simulation and a 1D model. The behavior observed in this work was attributed to the local strain gradients that take place due to the openings in the Si/SiOx substrate. This

gradients compete with the magnetic field, leading to pin or modify the DW velocity [206].

Bibliography

[1] S. Wolf, D. Awschalom, R. Buhrman, J. Daughton, v. S. von Molnár, M. Roukes, A. Y. Chtchelkanova, and D. Treger. "Spintronics: a spin-based electronics vision for the future". In: *science* 294.5546 (2001), pp. 1488–1495.

[2] M. N. Baibich, J. M. Broto, A. Fert, F. N. Van Dau, F. Petroff, P. Etienne, G. Creuzet, A. Friederich, and J. Chazelas. "Giant magnetoresistance of (001) Fe/(001) Cr magnetic superlattices". In: *Physical review letters* 61.21 (1988), p. 2472.

[3] C. Day. "Discoverers of giant magnetoresistance win this year's physics nobel". In: *Physics Today* 60.12 (2007), pp. 12–14.

[4] C. Chappert, A. Fert, and F. N. Van Dau. "The emergence of spin electronics in data storage". In: *Nature materials* 6.11 (2007), pp. 813–823.

[5] P. Barla, V. K. Joshi, and S. Bhat. "Spintronic devices: a promising alternative to CMOS devices". In: *Journal of Computational Electronics* 20.2 (2021), pp. 805–837.

[6] S. A. Wolf, J. Lu, M. R. Stan, E. Chen, and D. M. Treger. "The promise of nanomagnetics and spintronics for future logic and universal memory". In: *Proceedings of the IEEE* 98.12 (2010), pp. 2155–2168.

[7] R. Lavrijsen, J.-H. Lee, A. Fernández-Pacheco, D. C. Petit, R. Mansell, and R. P. Cowburn. "Magnetic ratchet for three-dimensional spintronic memory and logic". In: *Nature* 493.7434 (2013), pp. 647–650.

[8] K. Y. Mak, J. Xia, X.-C. Zhang, L. Li, M. Fattouhi, M. Ezawa, X.-X. Liu, and Y. Zhou. "Single-bit full adder and logic gate based on synthetic antiferromagnetic bilayer skyrmions". In: *Rare Metals* 41.7 (2022), pp. 2249–2258.

[9] X. Yao, J. Harms, A. Lyle, F. Ebrahimi, Y. Zhang, and J.-P. Wang. "Magnetic tunnel junction-based spintronic logic units operated by spin transfer torque". In: *IEEE Transactions on Nanotechnology* 11.1 (2011), pp. 120–126.

[10] S. S. Parkin, M. Hayashi, and L. Thomas. "Magnetic domain-wall racetrack memory". In: *Science* 320.5873 (2008), pp. 190–194.

[11] S. Fukami and H. Ohno. "Perspective: Spintronic synapse for artificial neural network". In: *Journal of Applied Physics* 124.15 (2018).

[12] A. Makarov, T. Windbacher, V. Sverdlov, and S. Selberherr. "CMOS-compatible spintronic devices: a review". In: *Semiconductor Science and Technology* 31.11 (2016), p. 113006.

[13] S. Parkin, X. Jiang, C. Kaiser, A. Panchula, K. Roche, and M. Samant. "Magnetically engineered spintronic sensors and memory". In: *Proceedings of the IEEE* 91.5 (2003), pp. 661–680.

[14]Z. Zhang, Y. Zhu, Y. Zhang, K. Zhang, J. Nan, Z. Zheng, Y. Zhang, and W. Zhao. “Skyrmion-based ultra-low power electric-field-controlled reconfigurable (SUPER) logic gate, IEEE Trans”. In: *Electron Devices* 40 (2019), p. 1984.

[15]W. H. Brigner, X. Hu, N. Hassan, C. H. Bennett, J. A. C. Incorvia, F. Garcia-Sanchez, and J. S. Friedman. “Graded-anisotropy-induced magnetic domain wall drift for an artificial spintronic leaky integrate-and-fire neuron”. In: *IEEE Journal on Exploratory Solid-State Computational Devices and Circuits* 5.1 (2019), pp. 19–24.

[16]W. H. Brigner, N. Hassan, L. Jiang-Wei, X. Hu, D. Saha, C. H. Bennett, M. J. Marinella, J. A. C. Incorvia, F. Garcia-Sanchez, and J. S. Friedman. “Shape-based magnetic domain wall drift for an artificial spintronic leaky integrate-and-fire neuron”. In: *IEEE Transactions on Electron Devices* 66.11 (2019), pp. 4970–4975.

[17]B. Dieny, I. L. Prejbeanu, K. Garello, P. Gambardella, P. Freitas, R. Lehndorff, W. Raberg, U. Ebels, S. O. Demokritov, J. Akerman, et al. “Opportunities and challenges for spintronics in the microelectronics industry”. In: *Nature Electronics* 3.8 (2020), pp. 446–459.

[18]A. Hirohata, K. Yamada, Y. Nakatani, I.-L. Prejbeanu, B. Diény, P. Pirro, and B. Hillebrands. “Review on spintronics: Principles and device applications”. In: *Journal of Magnetism and Magnetic Materials* 509 (2020), p. 166711.

[19]S. Chikazumi. *Physics of ferromagnetism*. 94. Oxford university press, 1997.

[20]S. Blundell. *Magnetism in condensed matter*. OUP Oxford, 2001.

[21]A. B. Pippard. *Magnetoresistance in metals*. Vol. 2. Cambridge university press, 1989.

[22]E. Hirota, H. Sakakima, and K. Inomata. *Giant magneto-resistance devices*. Vol. 40. Springer Science & Business Media, 2002.

[23]J. C. Mallinson. *Magneto-resistive and spin valve heads: fundamentals and applications*. Elsevier, 2001.

[24]A. N. Bogdanov and D. Yablonskii. “Thermodynamically stable “vortices” in magnetically ordered crystals. The mixed state of magnets”. In: *Zh. Eksp. Teor. Fiz* 95.1 (1989), p. 178.

[25]S. Mühlbauer, B. Binz, F. Jonietz, C. Pfleiderer, A. Rosch, A. Neubauer, R. Georgii, and P. Böni. “Skyrmion lattice in a chiral magnet”. In: *Science* 323.5916 (2009), pp. 915–919.

[26]A. Fert, V. Cros, and J. Sampaio. “Skyrmions on the track”. In: *Nat. Nano* 8 (2013), p. 152.

[27]B. Göbel and I. Mertig. “Skyrmion ratchet propagation: Utilizing the skyrmion Hall effect in AC racetrack storage devices”. In: *Sci Rep* 11 (2021), p. 3020.

[28]M. Fattouhi, M. Y. El Hafidi, and M. El Hafidi. “Single skyrmion induced by external magnetic field in CoFeB ferromagnetic alloy nanodisks”. In: *Journal of Magnetism and Magnetic Materials* 468 (2018), pp. 8–13.

[29] K. Everschor-Sitte, J. Masell, R. M. Reeve, and M. Kläui. "Perspective: Magnetic skyrmions—Overview of recent progress in an active research field". In: *Journal of Applied Physics* 124.24 (2018).

[30] S. Das, Y. Tang, Z. Hong, M. Gonçalves, M. McCarter, C. Klewe, K. Nguyen, F. Gómez-Ortiz, P. Shafer, E. Arenholz, et al. "Observation of room-temperature polar skyrmions". In: *Nature* 568.7752 (2019), pp. 368–372.

[31] A. Leonov, T. Monchesky, N. Romming, A. Kubetzka, A. Bogdanov, and R. Wiesendanger. "The properties of isolated chiral skyrmions in thin magnetic films". In: *New Journal of Physics* 18.6 (2016), p. 065003.

[32] Y. Zhang, S. Luo, B. Yan, J. Ou-Yang, X. Yang, S. Chen, B. Zhu, and L. You. "Magnetic skyrmions without the skyrmion Hall effect in a magnetic nanotrack with perpendicular anisotropy". In: *Nanoscale* 9 (2017), p. 10212.

[33] B. Göbel, A. Mook, J. Henk, and I. Mertig. "Overcoming the speed limit in skyrmion racetrack devices by suppressing the skyrmion Hall effect". In: *Phys. Rev. B* 99 (2019), 020405(R).

[34] C. A. Akosa, H. Li, G. Tatara, and O. A. Tretiakov. "Tuning the Skyrmion Hall Effect via Engineering of Spin-Orbit Interaction". In: *Phys. Rev. Appl.* 12 (2019), p. 054032.

[35] M. Fattouhi, K. Y. Mak, Y. Zhou, X. Zhang, X. Liu, and M. E. Hafidi. "Logic Gates Based on Synthetic Antiferromagnetic Bilayer Skyrmions, Phys". In: *Rev. Appl.* 16 (2021), p. 014040.

[36] M. Chauwin, X. Hu, F. Garcia-Sanchez, N. Betrabet, A. Paler, C. Moutafis, and J. S. Friedman. "Skyrmion Logic System for Large-Scale Reversible Computation, Phys". In: *Rev. Appl.* 12 (2019), p. 064053.

[37] S. Luo, M. Song, X. Li, Y. Zhang, J. Hong, X. Yang, X. Zou, N. Xu, and L. You. "Reconfigurable skyrmion logic gates". In: *Nano Lett.* 18 (2018), p. 1180.

[38] K. M. Song et al. "Skyrmion-based artificial synapses for neuromorphic computing". In: *Nat Electron* 3 (2020), p. 148.

[39] D. Prychynenko, M. Sitte, K. Litzius, B. Krüger, G. Bourianoff, M. Kläui, J. Sinova, and K. Everschor-Sitte. "Magnetic Skyrmion as a Nonlinear Resistive Element: A Potential Building Block for Reservoir Computing". In: *Phys. Rev. Appl.* 9 (2018), p. 014034.

[40] X. Chen, H. Zhang, E. Deng, M. Yang, N. Lei, Y. Zhang, W. Kang, and W. Zhao. "Sky-RAM: Skyrmionic random access memory". In: *IEEE Electron Device Lett.* 40 (2019), p. 722.

[41] R. Tomasello, E. Martinez, R. Zivieri, L. Torres, M. Carpentieri, and A. G. Finocchio. "strategy for the design of skyrmion racetrack memories". In: *Sci Rep* 4 (2014), p. 6784.

[42] A. D. Kent, H. Ohldag, H. A. Dürr, and J. Z. Sun. "Magnetization dynamics". In: *Handbook of Magnetism and Magnetic Materials* (2020), pp. 1–33.

[43] M. Liu and N. X. Sun. "Voltage control of magnetism in multiferroic heterostructures". In: *Philosophical Transactions of the Royal Society A: Mathematical, Physical and Engineering Sciences* 372.2009 (2014), p. 20120439.

[44]Y. Choi, C. Zhang, N. Lee, and S. Cheong. “Cross-control of magnetization and polarization by electric and magnetic fields with competing multiferroic and weak-ferromagnetic phases”. In: *Physical review letters* 105.9 (2010), p. 097201.

[45]Y.-H. Chu, L. W. Martin, M. B. Holcomb, and R. Ramesh. “Controlling magnetism with multiferroics”. In: *Materials Today* 10.10 (2007), pp. 16–23.

[46]W. Eerenstein, N. Mathur, and J. F. Scott. “Multiferroic and magnetoelectric materials”. In: *nature* 442.7104 (2006), pp. 759–765.

[47]C. A. Vaz. “Electric field control of magnetism in multiferroic heterostructures”. In: *Journal of Physics: Condensed Matter* 24.33 (2012), p. 333201.

[48]J.-M. Hu, L.-Q. Chen, and C.-W. Nan. “Multiferroic heterostructures integrating ferroelectric and magnetic materials”. In: *Advanced materials* 28.1 (2016), pp. 15–39.

[49]I. Gilbert, A. C. Chavez, D. T. Pierce, J. Unguris, W.-Y. Sun, C.-Y. Liang, and G. P. Carman. “Magnetic microscopy and simulation of strain-mediated control of magnetization in PMN-PT/Ni nanostructures”. In: *Applied physics letters* 109.16 (2016).

[50]X. Li, D. Carka, C.-y. Liang, A. E. Sepulveda, S. M. Keller, P. K. Amiri, G. P. Carman, and C. S. Lynch. “Strain-mediated 180 perpendicular magnetization switching of a single domain multiferroic structure”. In: *Journal of Applied Physics* 118.1 (2015).

[51]Z. Xiao, R. Lo Conte, C. Chen, C.-Y. Liang, A. Sepulveda, J. Bokor, G. P. Carman, and R. N. Candler. “Bi-directional coupling in strain-mediated multiferroic heterostructures with magnetic domains and domain wall motion”. In: *Scientific reports* 8.1 (2018), p. 5207.

[52]M. Filianina, L. Baldrati, T. Hajiri, K. Litzius, M. Foerster, L. Aballe, and M. Kläui. “Piezo-electrical control of gyration dynamics of magnetic vortices”. In: *Applied Physics Letters* 115.6 (2019).

[53]G. Breit. “The magnetic moment of the electron”. In: *Nature* 122.3078 (1928), pp. 649–649.

[54]P. Kusch and H. Foley. “The magnetic moment of the electron”. In: *Physical Review* 74.3 (1948), p. 250.

[55]A. Aharoni. *Introduction to the Theory of Ferromagnetism*. Vol. 109. Clarendon Press, 2000.

[56]D. J. Griffiths and D. F. Schroeter. *Introduction to quantum mechanics*. Cambridge university press, 2018.

[57]L. Exl, D. Suess, and T. Schrefl. “Micromagnetism”. In: *Handbook of Magnetism and Magnetic Materials* (2020), pp. 1–44.

[58]P. Curie. “Sur une balance de précision et à lecture directe des derniers poids”. In: *CR Hebd Séances Acad Sci* 108 (1889), pp. 663–666.

[59]M. Massimi. *Pauli’s exclusion principle: The origin and validation of a scientific principle*. Cambridge University Press, 2005.

[60]I. G. Kaplan. *The Pauli exclusion principle: origin, verifications, and applications*. John Wiley & Sons, 2017.

[61]A. Aharoni. "Demagnetizing factors for rectangular ferromagnetic prisms". In: *Journal of Applied Physics* 83.6 (1998), pp. 3432–3434. eprint: https://doi.org/10.1063/1.367113.

[62]I. Dzyaloshinskii et al. "Thermodynamic theory of weak ferromagnetism in antiferromagnetic substances". In: *Sov. Phys. JETP* 5.6 (1957), pp. 1259–1272.

[63]T. Moriya. "Anisotropic superexchange interaction and weak ferromagnetism". In: *Physical review* 120.1 (1960), p. 91.

[64]M. Getzlaff. "Magnetic Anisotropy Effects". In: *Fundamentals of Magnetism*. Berlin, Heidelberg: Springer Berlin Heidelberg, 2008, pp. 89–115.

[65]J. Zang, V. Cros, and A. Hoffmann. *Topology in magnetism*. Vol. 192. Springer, 2018.

[66]S. Seki and M. Mochizuki. *Skyrmions in magnetic materials*. Springer, 2016.

[67]A. Thiaville, S. Rohart, É. Jué, V. Cros, and A. Fert. "Dynamics of Dzyaloshinskii domain walls in ultrathin magnetic films". In: *EPL (Europhysics Letters)* 100.5 (Dec. 2012), p. 57002.

[68]A. Bogdanov and U. Rößler. "Chiral symmetry breaking in magnetic thin films and multilayers". In: *Physical review letters* 87.3 (2001), p. 037203.

[69]S. Rohart and A. Thiaville. "Skyrmion confinement in ultrathin film nanostructures in the presence of Dzyaloshinskii-Moriya interaction". In: *Physical Review B* 88.18 (2013), p. 184422.

[70]B. Dieny and M. Chshiev. "Perpendicular magnetic anisotropy at transition metal/oxide interfaces and applications". In: *Reviews of Modern Physics* 89.2 (2017), p. 025008.

[71]K. Nakamura, T. Akiyama, T. Ito, M. Weinert, and A. Freeman. "Role of an interfacial FeO layer in the electric-field-driven switching of magnetocrystalline anisotropy at the Fe/MgO interface". In: *Physical Review B* 81.22 (2010), p. 220409.

[72]M. Blanco-Rey, P. Perna, A. Gudin, J. M. Diez, A. Anadón, P. Olleros-Rodríguez, L. de Melo Costa, M. Valvidares, P. Gargiani, A. Guedeja-Marron, et al. "Large Perpendicular Magnetic Anisotropy in Nanometer-Thick Epitaxial Graphene/Co/Heavy Metal Heterostructures for Spin–Orbitronics Devices". In: *ACS Applied Nano Materials* 4.5 (2021), pp. 4398–4408.

[73]P. Carcia. "Magnetic Anisotropy and Structure of Palladium/Cobalt and Platinum/Cobalt Artificial Metal Superlattices.(Retroactive Coverage)". In: *Physics of Magnetic Materials* (1987), pp. 240–245.

[74]G. Winkler, A. Kobs, A. Chuvilin, D. Lott, A. Schreyer, and H. Oepen. "On the variation of magnetic anisotropy in Co/Pt (111) on silicon oxide". In: *Journal of Applied Physics* 117.10 (2015).

[75]M. Johnson, R. Jungblut, P. Kelly, and F. Den Broeder. “Perpendicular magnetic anisotropy of multilayers: recent insights”. In: *Journal of magnetism and magnetic materials* 148.1-2 (1995), pp. 118–124.

[76]R. C. Fernow. *Principles of magnetostatics*. Cambridge University Press, 2017.

[77]M. Schabes and A. Aharoni. “Magnetostatic interaction fields for a three-dimensional array of ferromagnetic cubes”. In: *IEEE Transactions on Magnetics* 23.6 (1987), pp. 3882–3888.

[78]D. D. Stancil. *Theory of magnetostatic waves*. Springer Science & Business Media, 2012.

[79]G. Bertotti. *Hysteresis in magnetism: for physicists, materials scientists, and engineers*. Gulf Professional Publishing, 1998.

[80]W. F. Brown. “Micromagnetics”. In: *New York: Interscience Publisher* (1963).

[81]D. Cortés-Ortuño, M. Beg, V. Nehruji, L. Breth, R. Pepper, T. Kluyver, G. Downing, T. Hesjedal, P. Hatton, T. Lancaster, et al. “Proposal for a micromagnetic standard problem for materials with Dzyaloshinskii–Moriya interaction”. In: *New Journal of Physics* 20.11 (2018), p. 113015.

[82]N. S. Gusev, A. V. Sadovnikov, S. A. Nikitov, M. V. Sapozhnikov, and O. G. Udalov. “Manipulation of the Dzyaloshinskii–Moriya Interaction in Co/Pt Multilayers with Strain”. In: *Phys. Rev. Lett.* 124 (15 Apr. 2020), p. 157202.

[83]A. Seo, P. P. Stavropoulos, H.-H. Kim, K. Fürsich, M. Souri, J. G. Connell, H. Gretarsson, M. Minola, H. Y. Kee, and B. Keimer. “Compressive strain induced enhancement of exchange interaction and short-range magnetic order in $\mathrm{Sr_2IrO_4}$ investigated by Raman spectroscopy”. In: *Phys. Rev. B* 100 (16 Sept. 2019), p. 165106.

[84]C. Feng, Y. Li, L. Wang, Y. Cao, M. Yao, F. Meng, F. Yang, B. Li, K. Wang, and G. Yu. “Giant strain control of antiferromagnetic moment in metallic FeMn by tuning exchange spring structure”. In: *Advanced Functional Materials* 30.14 (2020), p. 1909708.

[85]A. Hubert and R. Schäfer. *Magnetic domains: the analysis of magnetic microstructures*. Springer Science & Business Media, 2008.

[86]W. Voigt. “Lehrbuch der Kristallphysik (reprinted 1928)”. In: *Teubner, Leipzig* (1910).

[87]K. Helbig. “Foundations of Anisotropy for Exploration Seismics, 486 pp”. In: *NY: Elsevier* (1994).

[88]J. Mandel. “Généralisation de la théorie de plasticité de WT Koiter”. In: *International Journal of Solids and structures* 1.3 (1965), pp. 273–295.

[89]A. E. H. Love. *A treatise on the mathematical theory of elasticity*. University press, 1927.

[90]C. Kittel. “Physical Theory of Ferromagnetic Domains”. In: *Rev. Mod. Phys.* 21 (4 Oct. 1949), pp. 541–583.

[91]R. Roldán, A. Castellanos-Gomez, E. Cappelluti, and F. Guinea. “Strain engineering in semiconducting two-dimensional crystals”. In: *Journal of Physics: Condensed Matter* 27.31 (2015), p. 313201.

[92]R.-C. Peng, J.-M. Hu, K. Momeni, J.-J. Wang, L.-Q. Chen, and C.-W. Nan. “Fast 180 magnetization switching in a strain-mediated multiferroic heterostructure driven by a voltage”. In: *Scientific reports* 6.1 (2016), p. 27561.

[93]E. P. Wohlfarth. *Handbook of magnetic materials*. Vol. 2. Elsevier, 1986.

[94]M. C. Hickey and J. S. Moodera. “Origin of intrinsic Gilbert damping”. In: *Physical review letters* 102.13 (2009), p. 137601.

[95]K. Eason, M. Patricia Rouelli Garcia Sabino, M. Tran, and Y. Fook Liew. “Origins of magnetic damping measurement variations using ferromagnetic resonance for nano-sized devices”. In: *Applied Physics Letters* 102.23 (2013).

[96]L. Landau and E. Lifshitz. “On the theory of the dispersion of magnetic permeability in ferromagnetic bodies. reproduced in collected papers of ld landau”. In: *Pergamon, New York* (1935).

[97]T. L. Gilbert. “A Lagrangian formulation of the gyromagnetic equation of the magnetization field”. In: *Phys. Rev.* 100 (1955), p. 1243.

[98]J. Xiao, A. Zangwill, and M. D. Stiles. “Macrospin models of spin transfer dynamics”. In: *Physical Review B* 72.1 (2005), p. 014446.

[99]J. Sinova, S. O. Valenzuela, J. Wunderlich, C. H. Back, and T. Jungwirth. “Spin Hall effects”. In: *Rev. Mod. Phys.* 87 (4 Sept. 2015), pp. 1213–1260.

[100]A. Vansteenkiste, J. Leliaert, M. Dvornik, M. Helsen, F. Garcia-Sanchez, and B. Van Waeyenberge. “The design and verification of MuMax3”. In: *AIP advances* 4.10 (2014), p. 107133.

[101]N. L. Schryer and L. R. Walker. “The motion of 180 domain walls in uniform dc magnetic fields”. In: *Journal of Applied Physics* 45.12 (1974), pp. 5406–5421. eprint: https://doi.org/10.1063/1.1663252.

[102]A. Malozemoff and J. Slonczewski. “Magnetic domain walls in bubble materials, Appl”. In: *Solid State Sci.(Academic Press, New York, NY, 1979)* (1979).

[103]O. Alejos, V. Raposo, and E. Martinez. “Domain Wall Motion in Magnetic Nanostrips”. In: *Materials Science and Technology*. John Wiley and Sons, Ltd, 2020. Chap. 5, pp. 1–49. eprint: 10.1002/9783527603978.mst0459.

[104]D. Kumar, T. Jin, R. Sbiaa, M. Kläui, S. Bedanta, S. Fukami, D. Ravelosona, S.-H. Yang, X. Liu, and S. Piramanayagam. “Domain wall memory: Physics, materials, and devices”. In: *Physics Reports* 958 (2022), pp. 1–35.

[105]E. Raymenants, O. Bultynck, D. Wan, T. Devolder, K. Garello, L. Souriau, A. Thiam, D. Tsvetanova, Y. Canvel, D. Nikonov, et al. “Nanoscale domain wall devices with magnetic tunnel junction read and write”. In: *Nature Electronics* 4.6 (2021), pp. 392–398.

[106]S.-H. Yang and S. Parkin. “Novel domain wall dynamics in synthetic antiferromagnets”. In: *Journal of Physics: Condensed Matter* 29.30 (2017), p. 303001.

[107]O. Boulle, S. Rohart, L. D. Buda-Prejbeanu, E. Jué, I. M. Miron, S. Pizzini, J. Vogel, G. Gaudin, and A. Thiaville. “Domain Wall Tilting in the Presence of the Dzyaloshinskii-Moriya Interaction in Out-of-Plane Magnetized Magnetic Nanotracks”. In: *Phys. Rev. Lett.* 111 (21 Nov. 2013), p. 217203.

[108]O. Boulle, J. Vogel, H. Yang, S. Pizzini, D. de Souza Chaves, A. Locatelli, T. O. Menteş, A. Sala, L. D. Buda-Prejbeanu, O. Klein, et al. “Room-temperature chiral magnetic skyrmions in ultrathin magnetic nanostructures”. In: *Nature nanotechnology* 11.5 (2016), pp. 449–454.

[109]S. Heinze, K. Von Bergmann, M. Menzel, J. Brede, A. Kubetzka, R. Wiesendanger, G. Bihlmayer, and S. Blügel. “Spontaneous atomic-scale magnetic skyrmion lattice in two dimensions”. In: *nature physics* 7.9 (2011), pp. 713–718.

[110]T. H. R. Skyrme. “A non-linear field theory”. In: *Proceedings of the Royal Society of London. Series A. Mathematical and Physical Sciences* 260.1300 (1961), pp. 127–138.

[111]A. Bernand-Mantel, C. B. Muratov, and V. V. Slastikov. “A micromagnetic theory of skyrmion lifetime in ultrathin ferromagnetic films”. In: *Proceedings of the National Academy of Sciences* 119.29 (2022), e2122237119.

[112]A. Bernand-Mantel, C. B. Muratov, and T. M. Simon. “Unraveling the role of dipolar versus Dzyaloshinskii-Moriya interactions in stabilizing compact magnetic skyrmions”. In: *Physical Review B* 101.4 (2020), p. 045416.

[113]A. S. Varentcova, S. von Malottki, M. N. Potkina, G. Kwiatkowski, S. Heinze, and P. F. Bessarab. “Toward room-temperature nanoscale skyrmions in ultrathin films”. In: *npj Computational Materials* 6.1 (2020), p. 193.

[114]M. Fattouhi, M. Y. El Hafidi, and M. El Hafidi. “Formation of a hexagonal skyrmion lattice assisted by magnetic field in CeFeB ultrathin films”. In: *Journal of Magnetism and Magnetic Materials* 495 (2020), p. 165870.

[115]A. A. Thiele. “Steady-State Motion of Magnetic Domains”. In: *Phys. Rev. Lett.* 30 (6 Feb. 1973), pp. 230–233.

[116]C. Reichhardt, D. Ray, and C. J. O. Reichhardt. “Collective Transport Properties of Driven Skyrmions with Random Disorder”. In: *Phys. Rev. Lett.* 114.21720 (2015), p. 2.

[117]C. Reichhardt, C. J. O. Reichhardt, and M. V. Milosevic. “Statics and Dynamics of Skyrmions Interacting with Pinning: A Review”. In: *[cond-mat.mes-hall] arXiv:arXiv:* 2102 (), p. 10464. arXiv: 2102.10464.

[118]C. Reichhardt and C. J. O. Reichhardt. “Plastic flow and the skyrmion Hall effect”. In: *Nat. Commun.* 11 (2020), p. 738.

[119]W. Jiang, X. Zhang, G. Yu, W. Zhang, X. Wang, M. B. Jungfleisch, J. E. Pearson, X. Cheng, O. Heinonen, K. L. Wang, Y. Zhou, A. Hoffmann, and S. G. E. te Velthuis. “Direct observation of the skyrmion Hall effect”. In: *Nat. Phys.* 13 (2017), p. 162.

[120]X. Zhang, J. Xia, L. Shen, M. Ezawa, O. A. Tretiakov, G. Zhao, X. Liu, and Y. Zhou. “Static and dynamic properties of bimerons in a frustrated ferromagnetic monolayer”. In: *Physical Review B* 101.14 (2020), p. 144435.

[121]M.-W. Yoo, F. Mineo, and J.-V. Kim. “Analytical model of the deformation-induced inertial dynamics of a magnetic vortex”. In: *Journal of Applied Physics* 129.5 (2021).

[122]C. Song, C. Jin, J. Wang, Y. Ma, H. Xia, J. Wang, J. Wang, and Q. Liu. “Dynamics of a magnetic skyrmionium in an anisotropy gradient”. In: *Applied Physics Express* 12.8 (2019), p. 083003.

[123]A. Fert, N. Reyren, and V. Cros. “Magnetic skyrmions: advances in physics and potential applications”. In: *Nature Reviews Materials* 2.7 (2017), pp. 1–15.

[124]K. Litzius et al. “Skyrmion Hall effect revealed by direct time-resolved X-ray microscopy”. In: *Nat. Phys.* 13 (2017), p. 170.

[125]M. Fattouhi, F. Garcia-Sanchez, R. Yanes, V. Raposo, E. Martinez, and L. Lopez-Diaz. “Electric Field Control of the Skyrmion Hall Effect in Piezoelectric-Magnetic Devices”. In: *Phys. Rev. Appl.* 16 (4 Oct. 2021), p. 044035.

[126]G. Finocchio, M. Ricci, R. Tomasello, A. Giordano, M. Lanuzza, V. Puliafito, P. Burrascano, B. Azzerboni, and M. Carpentieri. “Skyrmion based microwave detectors and harvesting”. In: *Appl. Phys. Lett.* 107.26240 (2015), p. 1.

[127]R. Tomasello, S. Komineas, G. Siracusano, M. Carpentieri, and G. Finocchio. “Chiral skyrmions in an anisotropy gradient”. In: *Phys. Rev. B* 98 (2018), p. 024421.

[128]R. Yanes, F. Garcia-Sanchez, R. F. Luis, E. Martinez, V. Raposo, L. Torres, and L. Lopez-Diaz. “Skyrmion motion induced by voltage-controlled in-plane strain gradients”. In: *Appl. Phys. Lett.* 115.13240 (2019), p. 1.

[129]R. Nepala, U. Güngördü, and A. A. Kovalev. “Magnetic skyrmion bubble motion driven by surface acoustic waves”. In: *Appl. Phys. Lett.* 112.11240 (2018), p. 4.

[130]J. J. Liang, J. H. Yu, J. Chen, M. H. Qin, M. Zeng, X. B. Lu, X. S. Gao, and J.-M. Liu. “Magnetic field gradient driven dynamics of isolated skyrmions and antiskyrmions in frustrated magnets”. In: *New J. Phys.* 20 (2018), p. 053037.

[131]S. Li, J. Xia, X. Zhang, M. Ezawa, W. Kang, X. Liu, Y. Zhou, and W. Zhao. “Dynamics of a magnetic skyrmionium driven by spin waves”. In: *Appl. Phys. Lett.* 112.14240 (2018), p. 4.

[132]L. Kong and J. Zang. “Dynamics of an Insulating Skyrmion Under a Temperature Gradient”. In: *Phys. Rev. Lett.* 111 (2013), p. 067203.

[133]B. L. Brown, U. C. Täuber, and M. Pleimling. “Effect of the Magnus force on skyrmion relaxation dynamics”. In: *Phys. Rev. B* 97 (2018).

[134]H. Velkov, O. Gomonay, M. Beens, G. Schwiete, A. Brataas, J. Sinova, and R. A. Duine. “Phenomenology of current-induced skyrmion motion in antiferromagnets”. In: *New J. Phys.* 18 (2016), p. 075016.

[135]J. Barker and O. A. Tretiakov. “Static and dynamical properties of antiferromagnetic skyrmions in the presence of applied current and temperature”. In: *Phys Rev Let* 116.14720 (2016), p. 3.

[136]X. Zhang, Y. Zhou, and M. Ezawa. “Magnetic bilayer-skyrmions without skyrmion Hall effect”. In: *Nat. Comm* 7 (2016), p. 10293.

[137]W. Legrand, D. Maccariello, F. Ajejas, S. Collin, A. Vecchiola, K. Bouzehouane, N. Reyren, V. Cros, and A. Fert. “Room-temperature stabilization of antiferromagnetic skyrmions in synthetic antiferromagnets”. In: *Nat. Mater* 19 (2020), p. 34.

[138]T. Dohi, S. Dutta-Gupta, S. Fukami, and H. Ohno. “Formation and current-induced motion of synthetic antiferromagnetic skyrmion bubbles”. In: *Nat. Commun.* 10 (2019), p. 5153.

[139]L. Shen, X. Li, Y. Zhao, J. Xia, G. Zhao, and Y. Zhou. “Current-Induced Dynamics of the Antiferromagnetic Skyrmion and Skyrmionium”. In: *Phys. Rev. Appl.* 12 (2019), p. 064033.

[140]X. Zhang, J. Xia, Y. Zhou, D. Wang, X. Liu, W. Zhao, and M. Ezawa. “Control and manipulation of a magnetic skyrmionium in nanostructures”. In: *Phys. Rev. B* 94 (2016), p. 094420.

[141]C. Multiphysics. *user’s guide (4.3 ed)*. COMSOL Multiphysics AB. (www.comsol.com).

[142]S. J. A. Koh, H. P. Lee, C. Lu, and Q. H. Cheng. “Molecular dynamics simulation of a solid platinum nanowire under uniaxial tensile strain: Temperature and strain-rate effects”. In: *Phys. Rev. B* 72 (2005), p. 085414.

[143]A. T. Hindmarch, A. W. Rushforth, R. P. Campion, C. H. Marrows, and B. L. Gallagher. “Origin of in-plane uniaxial magnetic anisotropy in CoFeB amorphous ferromagnetic thin films”. In: *Phys. Rev. B* 83.21240 (2011), p. 4.

[144]C.-S. Zha, H.-k. Mao, and R. J. Hemley. “Elasticity of MgO and a primary pressure scale to 55 GPa”. In: *PNAS* 97 (2000), p. 1349.

[145]J. C. Slonczewski. “Current-driven excitation of magnetic multilayers”. In: *J. Magn. Magn. Mater* 159 (1996).

[146]I. B.-E. Mokhtari, D. Ourdani, Y. Roussigne, R. B. Mos, M. Nasui, S. M. Cherif, A. Stachkevich, M. S. Gabor, and M. Belmeguenai. “Investigation of the correlation between perpendicular magnetic anisotropy, spin mixing conductance and interfacial Dzyaloshinskii–Moriya interaction in CoFeB-based systems”. In: *J. Phys. D: Appl. Phys.* 53.50500 (2020), p. 3.

[147]L. H. Diez, F. García-Sánchez, J.-P. Adam, T. Devolder, S. Eimer, M. S. E. Hadri, A. Lamperti, R. Mantovan, B. Ocker, and D. Ravelosona. “Controlling magnetic domain wall motion in the creep regime in He+-irradiated CoFeB/MgO films with perpendicular anisotropy”. In: *Appl. Phys. Lett.* 107 (2015), p. 032401.

[148]J.-M. Hu, T. Yang, and L.-Q. Chen. “Strain-mediated voltage-controlled switching of magnetic skyrmions in nanostructures,” in: *Npj Comput Mater* 4 (2018), p. 62.

[149]M. Gueye, F. Zighem, M. Belmeguenai, M. S. Gabor, C. Tiusan, and D. Faurie. “Spectroscopic investigation of elastic and magnetoelastic properties of CoFeB thin films”. In: *J. Phys. D: Appl. Phys.* 49.14500 (2016), p. 3.

[150]L. H. Diez et al. “Enhancement of the dzyaloshinskii-moriya interaction and domain wall velocity through interface intermixing in Ta/CoFeB/MgO”. In: *Phys. Rev. B* 99 (2019), p. 054431.

[151]G. B. Philippa M. Shepley and T. Moore. “domain wall energy and strain in Pt/Co/Ir thin films on piezoelectric transducers”. In: *J. Phys: Condens. Matter* 30.34400 (2018), p. 2.

[152]J.-V. Kim and M.-W. Yoo. “Current-driven skyrmion dynamics in disordered films”. In: *Appl. Phys. Lett.* 110.13240 (2017), p. 4.

[153]J. Leliaert, B. V. de Wiele, A. Vansteenkiste, L. Laurson, G. Durin, L. Dupré, and B. V. Waeyenberge. “Current-driven domain wall mobility in polycrystalline permalloy nanowires: A numerical study”. In: *J. Appl. Phys.* 115.23390 (2014), p. 3.

[154]V. Raposo. “Ricardo francisco luis martinez, and eduardo martinez, current-driven skyrmion motion along disordered magnetic tracks”. In: *AIP Adv* 7 (2017), p. 056017.

[155]C. Reichhardt and C. J. O. Reichhardt. “Noise fluctuations and drive dependence of the skyrmion Hall effect in disordered systems”. In: *New J. Phys.* 18 (2016), p. 095005.

[156]K. Litzius et al. “The role of temperature and drive current in skyrmion dynamics”. In: *Nat Electron* 3 (2020), p. 30.

[157]C. Reichhardt and C. J. O. Reichhardt. “Thermal creep and the skyrmion Hall angle in driven skyrmion crystals”. In: *J. Phys: Condens. Matter* 31 (2019), 07LT01.

[158]J. C. Martinez, W. S. Lew, W. L. Gan, and M. B. A. Jalil. “Theory of current-induced skyrmion dynamics close to a boundary”. In: *J. Magn. Magn. Mater* 465 (2018), p. 685.

[159]M. Fattouhi, F. Garcia-Sanchez, R. Yanes, V. Raposo, E. Martinez, and L. Lopez-Diaz. “Absence of Walker Breakdown in the Dynamics of Chiral Néel Domain Walls Driven by In-Plane Strain Gradients”. In: *Phys. Rev. Appl.* 18 (4 Oct. 2022), p. 044023.

[160]S. Parkin and S. H. Yang. “Memory on the racetrack”. In: *Nature Nanotechnology* 10 (3 Mar. 2015), pp. 195–198.

[161]X. Zhang, N. Vernier, Z. Cao, Q. Leng, A. Cao, D. Ravelosona, and W. Zhao. “Magnetoresistive sensors based on the elasticity of domain walls”. In: *Nanotechnology* 29 (36 July 2018), p. 365502.

[162]J. H. Franken, H. J. Swagten, and B. Koopmans. “Shift registers based on magnetic domain wall ratchets with perpendicular anisotropy”. In: *Nature Nanotechnology* 7 (8 2012), pp. 499–503.

[163]Z. Luo, A. Hrabec, T. P. Dao, G. Sala, S. Finizio, J. Feng, S. Mayr, J. Raabe, P. Gambardella, and L. J. Heyderman. “Current-driven magnetic domain-wall logic”. In: *Nature* 579 (7798 Mar. 2020), pp. 214–218.

[164]M. Alamdar, T. Leonard, C. Cui, B. P. Rimal, L. Xue, O. G. Akinola, T. P. Xiao, J. S. Friedman, C. H. Bennett, M. J. Marinella, and J. A. C. Incorvia. “Domain wall-magnetic tunnel junction spin-orbit torque devices and circuits for in-memory computing”. In: *Applied Physics Letters* 118 (11 Mar. 2021), p. 112401.

[165]K. Yue, Y. Liu, R. K. Lake, and A. C. Parker. “A brain-plausible neuromorphic on-the-fly learning system implemented with magnetic domain wall analog memristors”. In: *Science Advances* 5.4 (2019), p. 8170.

[166]S. Glathe, R. Mattheis, and D. V. Berkov. “Direct observation and control of the Walker breakdown process during a field driven domain wall motion”. In: *Applied Physics Letters* 93 (7 2008), p. 072508.

[167]A. Mougin, M. Cormier, J. P. Adam, P. J. Metaxas, and J. Ferré. “Domain wall mobility, stability and Walker breakdown in magnetic nanowires”. In: *EPL* 78 (5 June 2007), p. 57007.

[168]K. S. Ryu, L. Thomas, S. H. Yang, and S. Parkin. “Chiral spin torque at magnetic domain walls”. In: *Nature Nanotechnology* 8 (7 2013), pp. 527–533.

[169]E. Martinez, S. Emori, and G. S. Beach. “Current-driven domain wall motion along high perpendicular anisotropy multilayers: The role of the Rashba field, the spin Hall effect, and the Dzyaloshinskii-Moriya interaction”. In: *Applied Physics Letters* 103 (7 Aug. 2013), p. 072406.

[170]T. Shiino, S. H. Oh, P. M. Haney, S. W. Lee, G. Go, B. G. Park, and K. J. Lee. “Antiferromagnetic Domain Wall Motion Driven by Spin-Orbit Torques”. In: *Physical Review Letters* 117 (8 Aug. 2016), p. 087203.

[171]S. A. Siddiqui, J. Han, J. T. Finley, C. A. Ross, and L. Liu. “Current-Induced Domain Wall Motion in a Compensated Ferrimagnet”. In: *Physical Review Letters* 121 (5 July 2018), p. 057701.

[172]S. H. Yang, K. S. Ryu, and S. Parkin. “Domain-wall velocities of up to 750 $m.s^{-1}$ driven by exchange-coupling torque in synthetic antiferromagnets”. In: *Nature Nanotechnology* 10 (3 Mar. 2015), pp. 221–226.

[173]W. H. Li, Z. Jin, D. L. Wen, X. M. Zhang, M. H. Qin, and J. M. Liu. “Ultrafast domain wall motion in ferrimagnets induced by magnetic anisotropy gradient”. In: *Physical Review B* 101 (2 Jan. 2020), p. 024414.

[174]L. Sanchez-Tejerina, O. Alejos, V. Raposo, and E. Martinez. “Current-driven domain wall motion along ferromagnetic strips with periodically-modulated perpendicular anisotropy”. In: *Journal of Applied Physics* 123 (22 June 2018), p. 223904.

[175]D. L. Wen, Z. Y. Chen, W. H. Li, M. H. Qin, D. Y. Chen, Z. Fan, M. Zeng, X. B. Lu, X. S. Gao, and J. M. Liu. “Ultralow-loss domain wall motion driven by a magnetocrystalline anisotropy gradient in an antiferromagnetic nanowire”. In: *Physical Review Research* 2 (1 Feb. 2020), p. 013166.

[176]J. H. Franken, M. Hoeijmakers, R. Lavrijsen, and H. J. Swagten. “Domain-wall pinning by local control of anisotropy in Pt/Co/Pt strips”. In: *Journal of Physics Condensed Matter* 24 (2 Jan. 2012), p. 024216.

[177]X. S. Wang and X. R. Wang. “Thermodynamic theory for thermal-gradient-driven domain-wall motion”. In: *Physical Review B* 90 (1 July 2014), p. 014414.

[178]F. Schlickeiser, U. Ritzmann, D. Hinzke, and U. Nowak. “Role of entropy in domain wall motion in thermal gradients”. In: *Physical Review Letters* 113 (9 Aug. 2014), p. 097201.

[179]K. V. Yershov, V. P. Kravchuk, D. D. Sheka, O. V. Pylypovskyi, D. Makarov, and Y. Gaididei. “Geometry-induced motion of magnetic domain walls in curved nanostripes”. In: *Phys. Rev. B* 98 (6 Aug. 2018), p. 060409.

[180]M. T. Bryan, J. Dean, and D. A. Allwood. “Dynamics of stress-induced domain wall motion”. In: *Phys. Rev. B* 85 (14 Apr. 2012), p. 144411.

[181]Z. Xiao, R. Lo Conte, C. Chen, et al. “Bi-directional coupling in strain-mediated multiferroic heterostructures with magnetic domains and domain wall motion.” In: *Scientific reports* 8 (2018), p. 5207.

[182]G. Yu, S. Shi, R. Peng, R. Guo, Y. Qiu, G. Wu, Y. Li, M. Zhu, and H. Zhou. “Strain-driven magnetic domain wall dynamics controlled by voltage in multiferroic heterostructures”. In: *Journal of Magnetism and Magnetic Materials* 552 (2022), p. 169229.

[183]F. Chen, X. Ge, W. Luo, R. Xing, S. Liang, X. Yang, L. You, R. Xiong, Y. Otani, and Y. Zhang. “Strain-induced Megahertz Oscillation and Stable Velocity of an Antiferromagnetic Domain Wall”. In: *Phys. Rev. Applied* 15 (1 Jan. 2021), p. 014030.

[184]P. Shepley, A. Rushforth, M. Wang, G. Burnell, and T. Moore. “Modification of perpendicular magnetic anisotropy and domain wall velocity in Pt/Co/Pt by voltage-induced strain”. In: *Scientific reports* 5.1 (2015), pp. 1–5.

[185]A. Malozemoff and J. Slonczewski. “IV - Domain-Wall Statics”. In: *Magnetic Domain Walls in Bubble Materials*. Ed. by A. Malozemoff and J. Slonczewski. Academic Press, 1979, pp. 77–121.

[186]C.-Y. Liang, S. M. Keller, A. E. Sepulveda, A. Bur, W.-Y. Sun, K. Wetzlar, and G. P. Carman. “Modeling of magnetoelastic nanostructures with a fully coupled mechanical-micromagnetic model”. In: *Nanotechnology* 25.43 (Oct. 2014), p. 435701.

[187]K. J. A. Franke, C. Ophus, A. K. Schmid, and C. H. Marrows. “Switching between Magnetic Bloch and Néel Domain Walls with Anisotropy Modulations”. In: *Phys. Rev. Lett.* 127 (12 Sept. 2021), p. 127203.

[188]S. Emori, U. Bauer, S. Ahn, E. Martinez, and G. Beach. “Current-driven dynamics of chiral ferromagnetic domain walls”. In: *Nature Materials* 12 (2013), pp. 611–616.

[189]A. Malozemoff and J. Slonczewski. “V - Wall Dynamics in One Dimension”. In: *Magnetic Domain Walls in Bubble Materials*. Ed. by A. Malozemoff and J. Slonczewski. Academic Press, 1979, pp. 123–143.

[190]P. J. Metaxas, J. P. Jamet, A. Mougin, M. Cormier, J. Ferré, V. Baltz, B. Rodmacq, B. Dieny, and R. L. Stamps. “Creep and Flow Regimes of Magnetic Domain-Wall Motion in Ultrathin $\mathrm{Pt/Co/Pt}$ Films with Perpendicular Anisotropy”. In: *Phys. Rev. Lett.* 99 (21 Nov. 2007), p. 217208.

[191]P. Han, W. Yan, J. Tian, X. Huang, and H. Pan. “Cut directions for the optimization of piezoelectric coefficients of lead magnesium niobate lead titanate ferroelectric crystals”. In: *Applied Physics Letters* 86.5 (2005), p. 052902.

[192]A. Skaugen, P. Murray, and L. Laurson. “Analytical computation of the demagnetizing energy of thin-film domain walls”. In: *Phys. Rev. B* 100 (9 Sept. 2019), p. 094440.

[193]J. Kim, H. Akinaga, and J. Kim. “Direct observation of the spin configurations of vertical Bloch line”. In: *Applied Physics Letters* 98.5 (Feb. 2011), p. 052510. eprint: https://pubs.aip.org/aip/apl/article-pdf/doi/10.1063/1.3549694/14444573/052510_1_online.pdf.

[194]T. Herranen and L. Laurson. “Domain walls within domain walls in wide ferromagnetic strips”. In: *Phys. Rev. B* 92 (10 Sept. 2015), p. 100405.

[195]T. Herranen and L. Laurson. “Bloch-line dynamics within moving domain walls in 3D ferromagnets”. In: *Phys. Rev. B* 96 (14 Oct. 2017), p. 144422.

[196]J. Slonczewski. “Theory of Bloch-line and Bloch-wall motion”. In: *Journal of Applied Physics* 45.6 (1974), pp. 2705–2715.

[197]J. Żebrowski and A. Sukiennicki. “Dynamic Bloch-line stacking—A new domain-wall structure at high drives”. In: *Journal of Applied Physics* 52.6 (June 1981), pp. 4176–4180. eprint: https://pubs.aip.org/aip/jap/article-pdf/52/6/4176/7974498/4176_1_online.pdf.

[198]Y. Yoshimura, K.-J. Kim, T. Taniguchi, T. Tono, K. Ueda, R. Hiramatsu, T. Moriyama, K. Yamada, Y. Nakatani, and T. Ono. “Soliton-like magnetic domain wall motion induced by the interfacial Dzyaloshinskii–Moriya interaction”. In: *Nature Physics* 12.2 (2016), pp. 157–161.

[199]E. Haltz, K. J. Franke, and C. H. Marrows. “Dynamics of bistable N\’eel domain walls under spin-orbit torque”. In: *arXiv preprint arXiv:2303.06142* (2023).

[200]R. Morris. “The dilogarithm function of a real argument”. In: *Mathematics of computation* 33.146 (1979), pp. 778–787.

[201]M. Viret, A. Vanhaverbeke, F. Ott, and J.-F. Jacquinot. “Current induced pressure on a tilted magnetic domain wall”. In: *Phys. Rev. B* 72 (14 Oct. 2005), p. 140403.

[202]E. Della Torre. “Pressures on cylindrical magnetic domain walls”. In: *IEEE Transactions on Magnetics* 6.4 (1970), pp. 822–827.

[203]X. Zhang, N. Vernier, W. Zhao, H. Yu, L. Vila, Y. Zhang, and D. Ravelosona. “Direct Observation of Domain-Wall Surface Tension by Deflating or Inflating a Magnetic Bubble”. In: *Phys. Rev. Appl.* 9 (2 Feb. 2018), p. 024032.

[204]G. Masciocchi, M. Fattouhi, A. Kehlberger, L. Lopez-Diaz, M.-A. Syskaki, and M. Kläui. “Strain-controlled domain wall injection into nanowires for sensor applications”. In: *Journal of Applied Physics* 130.18 (2021).

[205]Z. Wang, P. Li, M. Fattouhi, Y. Yao, Y. L. Van Hees, C. F. Schippers, X. Zhang, R. Lavrijsen, F. Garcia-Sanchez, E. Martinez, et al. “Field-free spin-orbit torque switching of synthetic antiferromagnet through interlayer Dzyaloshinskii-Moriya interactions”. In: *Cell Reports Physical Science* 4.4 (2023).

[206] G. Masciocchi, M. Fattouhi, E. Spetzler, M.-A. Syskaki, R. Lehndorff, E. Martinez, J. McCord, L. Lopez-Diaz, A. Kehlberger, and M. Kläui. “Generation of imprinted strain gradients for spintronics”. In: *Applied Physics Letters* 123.2 (July 2023), p. 022404. eprint: https://pubs.aip.org/aip/apl/article-pdf/doi/10.1063/5.0157687/18038862/022404_1_5.0157687.pdf.

[207] S. I. Kin, T. S. Suh, and A. Ankiewicz. *Dissipative Solitons. Lecture Notes in Physics*. Springer, 2005.

[208] Z. Mei. *Numerical bifurcation analysis for reaction-diffusion equations*. Vol. 28. Springer Science & Business Media, 2000.

APPENDIX A

A.1 One-dimensional model

In this section we present some aspects about the one-dimensional model that are not detailed in the thesis.

A.1.1 Magnetic DW profile

We consider a thin ferromagnetic strip with perpendicular magnetization. In the absense of any external field or current the energy per unit volume can be expressed as

$$\mathcal{E} = A_{\mathrm{ex}} \mid \nabla \mathbf{m} \mid^2 + K_{\mathrm{u}}(1 - m_z^2) + \frac{\mu_0 M_{\mathrm{s}}^2}{2} N_z m_z^2 \tag{A.1}$$

Using spherical coordinates for the magnetization

$$\mathbf{m} = (\sin\theta\cos\phi, \sin\theta\sin\phi, \cos\theta) \tag{A.2}$$

and assuming that $\mathbf{m}$ changes only along the longitudinal direction, Eq. (A.1) can be rewritten as

$$\mathcal{E}[\theta(x)] = A_{\mathrm{ex}} \left(\frac{\partial\theta}{\partial x}\right)^2 + K_{\mathrm{eff}} \sin^2\theta \tag{A.3}$$

where $K_{\mathrm{eff}} = K_{\mathrm{u}} - \frac{\mu_0 M_{\mathrm{s}}^2}{2} N_z$ is the effective anisotropy including both the magnetocrystalline and the magnetostatic contributions as discussed previously in Sec. 2.8.1.

To find a profile $\theta(x)$ that minimizes the energy we assume a small variation of $\theta(x) \to \theta(x) + \delta\theta(x)$. Following a variational procedure where the Eq. (A.3) should satisfy ${}^{\mathrm{d}\mathcal{E}(\theta)}/_{\mathrm{d}\theta} = 0$ we end up with a second order differential equation for $\theta(x)$ as

$$A_{\mathrm{ex}}\frac{\partial^2\theta}{\partial x^2} - 2K_{\mathrm{eff}}\cos\theta\sin\theta = 0 \tag{A.4}$$

Multiplying Eq. (A.4) by $\frac{\partial\theta}{\partial x}$, integrating it along x-axis and solving the resulting first order differential equation yields

$$\theta(x) = 2\tan^{-1} e^{\pm\frac{x}{\Delta}} \tag{A.5}$$

Eq. (A.5) describes the DW spatial profile with $\Delta = \sqrt{\frac{A_{\mathrm{ex}}}{K_{\mathrm{eff}}}}$ being the DW width and it is the commonly used SW ansatz in reduced models like the ones used in this thesis [101].

A.1.2 Derivation of the dynamic equations

In this subsection we will present the detailed derivation of the 1D model dynamic equations.

Considering the constraint $|\mathbf{m}| = 1$ and the magnetization vector in spherical coordinates Eq. (A.2), the magnetization gradient reads

$$\nabla\mathbf{m} = (\nabla\theta)\mathbf{e}_\theta + \sin\theta(\nabla\phi)\mathbf{e}_\phi \tag{A.6}$$

where θ and ϕ are the magnetization spherical coordinates. Using Eq. (A.2) and Eq. (A.6) the micromagnetic energy density terms presented in Sec. 2.3 can be expressed as

$$\mathcal{E}_{\mathrm{ex}} = A_{\mathrm{ex}}(\nabla\mathbf{m})^2 = A_{\mathrm{ex}}\left[(\nabla\theta)^2 + \sin^2\theta(\nabla\phi)^2\right] \tag{A.7}$$

$$\begin{aligned}\mathcal{E}_{\mathrm{d}} &= -\frac{1}{2}\mu_0 M_{\mathrm{s}}\mathbf{H}_{\mathrm{d}}\cdot\mathbf{m} = -\frac{1}{2}\mu_0 M_{\mathrm{s}}^2\mathbf{m}\cdot\bar{N}\mathbf{m} = -\frac{1}{2}\mu_0 M_{\mathrm{s}}^2\left(N_x m_x^2 + N_y m_y^2 + N_z m_z^2\right)\\ &= -\frac{1}{2}\mu_0 M_{\mathrm{s}}^2\left[N_z + (N_x - N_z)\sin^2\theta + (N_y - N_x)\sin^2\theta\sin^2\phi\right]\end{aligned} \tag{A.8}$$

with N_x, N_y and N_z are the demagnetizing factors discussed before in Sec. 2.8.1.

$$\mathcal{E}_{anis} = K_{\mathrm{u}}\left(1 - (\mathbf{m}\cdot\mathbf{e}_z)^2\right) = K_{\mathrm{u}}\sin^2\theta \tag{A.9}$$

$$\mathcal{E}_Z = -\mu_0 M_\mathrm{s} \mathbf{H}_{ext} \cdot \mathbf{m} = -\mu_0 M_\mathrm{s} \left(H_x \sin\theta \cos\phi + H_y \sin\theta \sin\phi + H_z \cos\theta \right) \quad \text{(A.10)}$$

with H_x, H_y and H_z being the Cartesian components of the external field.

$$\begin{aligned} \mathcal{E}_{DM} &= D\left[m_z(\nabla \mathbf{m}) - (m \cdot \nabla) m_z \right] = D(m_z \frac{\partial m_x}{\partial x} - m_x \frac{\partial m_z}{\partial x} + m_z \frac{\partial m_y}{\partial y} - m_y \frac{\partial m_z}{\partial y}) \\ &= D\left[\cos\phi \frac{\partial \theta}{\partial x} + \sin\phi \frac{\partial \theta}{\partial y} + \sin\theta \cos\theta \left(\sin\phi \frac{\partial \phi}{\partial x} - \cos\phi \frac{\partial \phi}{\partial y} \right) \right] \quad \text{(A.11)} \end{aligned}$$

The DW profile within the 1D model is described by the well-known Walker ansatz, which was derived previously in Eq. (A.5) and reads [67, 101]

$$\theta(x,t) = 2\tan^{-1} e^{Q\frac{x-q(t)}{\Delta}} \quad \text{(A.12a)}$$

$$\phi(x,t) = \varphi(t) \quad \text{(A.12b)}$$

where q denotes the DW position along x-axis, φ the internal DW angle with respect to x-axis and $Q = +1$ for an up-down DW or $Q = -1$ for a down-up DW going from left to right across the wall along the x-axis.

Using Eq. (A.12) the total micromagnetic energy density can be expressed as

$$\begin{aligned} \mathcal{E} = A_\mathrm{ex} \frac{\sin^2\theta}{\Delta^2} + K_\mathrm{eff} \sin^2\theta + K_\mathrm{sh} \sin^2\theta \sin^2\phi + QD\cos\phi \left(\frac{\sin\theta}{\Delta} \right) \\ - \mu_0 M_\mathrm{s} (H_x \sin\theta\cos\phi + H_y \sin\theta \sin\phi + H_z \cos\theta) \quad \text{(A.13)} \end{aligned}$$

where $K_\mathrm{eff} = K_\mathrm{u} - \frac{1}{2}\mu_0 M_\mathrm{s}^2 N_z$ and $K_\mathrm{sh} = \frac{1}{2}\mu_0 M_\mathrm{s}^2 (N_y - N_x)$. The following identities were used in the derivations

$$\nabla\theta(x,t) = \frac{\partial\theta}{\partial x} = Q\frac{\sin\theta}{\Delta} \quad \text{(A.14a)}$$

$$\delta\theta(x,t) = -Q\frac{\sin\theta}{\Delta}\delta q \quad \text{(A.14b)}$$

$$\dot{\theta}(x,t) = -Q\frac{\sin\theta}{\Delta}\dot{q} \quad \text{(A.14c)}$$

$$\nabla\phi = \delta\phi = 0 \quad \text{(A.14d)}$$

$$\dot{\phi} = \dot{\varphi} \quad \text{(A.14e)}$$

By integrating Eq. (A.13) along the x-axis, the DW surface energy density $\mathcal{U}_\mathrm{DW}$ reads

$$\mathcal{U}_{\mathrm{DW}} = \int_{-\infty}^{+\infty} \mathcal{E}\,\mathrm{d}x = \frac{2A_{\mathrm{ex}}}{\Delta} + 2\Delta(K_{\mathrm{eff}} + K_{\mathrm{sh}}\sin^2\varphi) + \pi Q D\cos\varphi \\ - \mu_0 M_{\mathrm{s}}\pi\Delta(H_x\cos\varphi + H_y\sin\varphi) - 2Q\mu_0 M_{\mathrm{s}} q H_z \quad \text{(A.15)}$$

where the following integrals were used

$$\int_{-\infty}^{+\infty} \sin^2\theta\, dx = 2\Delta \quad \text{(A.16a)}$$

$$\int_{-\infty}^{+\infty} (x-q)\sin^2\theta\, dx = 0 \quad \text{(A.16b)}$$

$$\int_{-\infty}^{+\infty} \cos\theta\sin\theta\, dx = 0 \quad \text{(A.16c)}$$

$$\int_{-\infty}^{+\infty} (x-q)^2\sin^2\theta\, dx = \Delta^3\frac{\pi^2}{6} \quad \text{(A.16d)}$$

$$\int_{-\infty}^{+\infty} \sin\theta\, dx = \pi\Delta \quad \text{(A.16e)}$$

$$\int_{-\infty}^{+\infty} \cos\theta\, dx = 2Qq \quad \text{(A.16f)}$$

The differential of the DW energy density with respect to the DW coordinates reads

$$d\mathcal{U}_{\mathrm{DW}} = \frac{\partial\mathcal{U}_{\mathrm{DW}}}{\partial q}\mathrm{d}q + \frac{\partial\mathcal{U}_{\mathrm{DW}}}{\partial\varphi}\mathrm{d}\varphi \quad \text{(A.17)}$$

with

$$\frac{\partial\mathcal{U}_{\mathrm{DW}}}{\partial q} = -2Q\mu_0 M_{\mathrm{s}} H_z \quad \text{(A.18a)}$$

$$\frac{\partial\mathcal{U}_{\mathrm{DW}}}{\partial\varphi} = 2\Delta K_{\mathrm{sh}}\sin 2\varphi - \pi Q D\sin\varphi \quad \text{(A.18b)}$$

As explained in Sec. 2.6, magnetization dynamics is governed by LLG equation augmented only with the damping-like SOT

$$\frac{\mathrm{d}\mathbf{m}}{\mathrm{d}t} = -\gamma_0\mathbf{m}\times\mathbf{H}_{\mathrm{eff}} + \alpha\mathbf{m}\times\frac{\mathrm{d}\mathbf{m}}{\mathrm{d}t} - \frac{\hbar \mathrm{J}_{\mathrm{HM}}\theta_{\mathrm{sh}}}{2\mu_0 M_{\mathrm{s}}|e|t_{\mathrm{FM}}}[\mathbf{m}\times(\mathbf{m}\times\boldsymbol{\sigma})] \quad \text{(A.19)}$$

Using spherical coordinates in Eq. (A.19) we obtain

$$\frac{\delta \mathcal{E}}{\delta \phi} = -\frac{\mu_0 M_\mathrm{s} \sin\theta}{\gamma_0}\left(\dot{\theta} + \alpha \sin\theta\, \dot{\phi} + \gamma_0 H_\mathrm{SOT} \cos\theta \sin\phi\right) \tag{A.20a}$$

$$\frac{\delta \mathcal{E}}{\delta \theta} = \frac{\mu_0 M_\mathrm{s}}{\gamma_0}\left(\sin\theta\, \dot{\phi} - \alpha\dot{\theta} + \gamma_0 H_\mathrm{SOT} \cos\phi\right) \tag{A.20b}$$

where $H_\mathrm{SOT} = \frac{\hbar \theta_\mathrm{sh} \mathrm{J_{HM}}}{2e\mu_0 M_\mathrm{s} t_\mathrm{FM}}$, $\mathrm{d}\mathbf{m} = \mathrm{d}\theta\ \mathbf{e}_\theta + \sin\theta \mathrm{d}\varphi\ \mathbf{e}_\varphi$ and $\mathbf{H}_\mathrm{eff} = -\frac{1}{\mu_0 M_\mathrm{s}}\frac{\delta \mathcal{E}}{\delta \theta}\ \mathbf{e}_\theta - \frac{1}{\mu_0 M_\mathrm{s} \sin\theta}\frac{\delta \mathcal{E}}{\delta \varphi}\ \mathbf{e}_\varphi$.

The variation of the micromagnetic energy density from Eq. (A.20) can be expressed as

$$\delta \mathcal{E} = \frac{\partial \mathcal{E}}{\partial \theta}\delta\theta + \frac{\partial \mathcal{E}}{\partial \phi}\delta\phi \tag{A.21}$$

Integrating Eq. (A.21) along x-axis gives

$$\mathrm{d}\mathcal{U}_\mathrm{DW} = \int_{-\infty}^{+\infty} \mathrm{d}x = -\frac{2\mu_0 M_\mathrm{s}}{\gamma_0}\left[\left(\alpha\frac{\dot{q}}{\Delta} + Q\dot{\varphi} + \gamma_0 \frac{\pi}{2} Q H_\mathrm{SOT} \cos\varphi\right)\mathrm{d}q + (Q\dot{q} - \alpha\Delta\dot{\varphi})\,\mathrm{d}\varphi\right] \tag{A.22}$$

Using Eq. (A.22) and Eq. (A.17) we get the dynamic equations describing the DW motion in presence of an external field H_z and a spin-polarized current $\mathrm{J_{HM}}$ as

$$(1+\alpha^2)\frac{\dot{q}}{\Delta} = -\alpha\ \Gamma_\mathrm{A} + Q\Gamma_\mathrm{B} \tag{A.23a}$$

$$(1+\alpha^2)\dot{\varphi} = -Q\Gamma_\mathrm{A} - \alpha\Gamma_\mathrm{B} \tag{A.23b}$$

where

$$\Gamma_\mathrm{A} = -\gamma_0 Q H_z + Q\gamma_0 \frac{\pi}{2} H_\mathrm{SOT} \cos\varphi$$

$$\Gamma_\mathrm{B} = \gamma_0 \frac{H_\mathrm{sh}}{2} \sin 2\varphi - \gamma_0 \frac{\pi}{2} Q H_\mathrm{DMI} \sin\varphi$$

and $H_\mathrm{DMI} = \frac{D}{\mu_0 M_\mathrm{s} \Delta}$.

A.2 Thiele's Model

In this appendix we derive the skyrmion dynamic equation presented in chapter 2 Eq. (2.69), which is also called Thiele's equation. To do so we consider LLG equation augmented with the damping-like SOT as shown in Eq. (A.19).

Eq. (A.19) LLG can be rearranged as

$$\frac{\partial \mathbf{m}}{\partial t} = \gamma_0 \mathbf{m} \times \underbrace{\left(-\mathbf{H}_{\text{eff}} + \frac{\alpha}{\gamma_0} \frac{\partial \mathbf{m}}{\partial t} + \mathbf{H}_{\text{SOT}} \right)}_{\mathbf{H}_0} \tag{A.25}$$

where $\mathbf{H}_{\text{SOT}} = -\frac{\hbar \mathrm{J}_{\text{HM}} \theta_{\text{sh}}}{2\mu_0 M_{\text{s}} |e| t_{\text{FM}}} (\mathbf{m} \times \boldsymbol{\sigma})$.

By multiplying both sides of Eq. (A.25) by $\mathbf{m}\times$ we get

$$\frac{1}{\gamma_0} \mathbf{m} \times \frac{\partial \mathbf{m}}{\partial t} = \mathbf{m} \cdot (\mathbf{H}_0 \cdot \mathbf{m}) - \mathbf{H}_0 \tag{A.26}$$

The main assumption of Thiele's model is based on considering the magnetic structure (i.e. DW, Vortex or Skyrmion) as a rigid body moving along the ferromagnetic sample maintaining its structure, without distortion. This assumption results in the following mathematical formulation

$$\mathbf{m}(\mathbf{r}, t) = \mathbf{m}(\mathbf{r} - \mathbf{v}t) \tag{A.27}$$

with $\mathbf{v}$ being the velocity and $\mathbf{r} = (x, y, z)$ the position vector.

$$\frac{\partial \mathbf{m}}{\partial t} = -(\mathbf{v} \cdot \nabla)\mathbf{m} = \sum_i v_i \frac{\partial \mathbf{m}}{\partial x_i} \tag{A.28}$$

The total force acting on the magnetic texture reads

$$\mathbf{F} = \sum -\mu_0 M_{\text{s}} \int \mathbf{H}_{\text{eff}} \cdot \frac{\partial \mathbf{m}}{\partial x_i} \mathrm{d}V \tag{A.29}$$

Using Eqs. (A.27)-(A.29), Eq. (A.26) can be rewritten as

$$\frac{1}{\gamma_0} \sum_i \left[v_i \mathbf{m} \times \frac{\partial \mathbf{m}}{\partial x_i} + \alpha v_i \frac{\partial \mathbf{m}}{\partial x_i} \right] = \mathbf{H}_{\text{eff}} - \mathbf{H}_{\text{SOT}} + \mathbf{m} \cdot (\mathbf{H}_0 \cdot \mathbf{m}) \tag{A.30}$$

Multiplying both sides of Eq. (A.30) by $-\sum_i \mu_0 M_\mathrm{s} \int \frac{\partial \mathbf{m}}{\partial x_i} \mathrm{d}V$ and considering a 2D system where $\mathrm{d}V = t_\mathrm{FM} \mathrm{d}S$ we can write

$$\frac{-\mu_0 M_\mathrm{s} t_\mathrm{FM}}{\gamma_0} \iint \sum_i \sum_j \left[v_i \left(\frac{\partial \mathbf{m}}{\partial x_i} \times \frac{\partial \mathbf{m}}{\partial x_j} \right) \cdot \mathbf{m} \right. \\ \left. + \alpha v_i \left(\frac{\partial \mathbf{m}}{\partial x_i} \cdot \frac{\partial \mathbf{m}}{\partial x_j} \right) \right] \mathrm{d}x\mathrm{d}y = \mathbf{F} + \mathbf{F}_\mathrm{SOT} \quad \text{(A.31)}$$

Finally, Eq. (A.31) can be written in the tensor form yielding the well-known Thiele equation

$$\mathbf{G} \times (\mathbf{v} + \mathbf{u}) - \bar{\bar{\mathcal{D}}} \cdot (\alpha \mathbf{v} - \xi \mathbf{u}) = \mathbf{F} + \mathbf{F}_\mathrm{SOT} \quad \text{(A.32)}$$

where $\mathbf{G} = G\mathbf{e}_z$ with

$$G = -\frac{\mu_0 M_\mathrm{s} t_\mathrm{FM}}{\gamma_0} \iint \mathbf{m} \cdot \left(\frac{\partial \mathbf{m}}{\partial x} \times \frac{\partial \mathbf{m}}{\partial y} \right) \mathrm{d}x\mathrm{d}y \quad \text{(A.33)}$$

being the gyrovector, which reads $G = \frac{-\mu_0 M_\mathrm{s} t_\mathrm{FM}}{\gamma_0} Q_\mathrm{sk}$ for any arbitrary magnetic texture with a non-vanishing topological charge Q_sk [115]. The second-rank tensor $\bar{\bar{\mathcal{D}}}$ is the so-called dissipation tensor, whose components read

$$\mathcal{D}_{ij} = \frac{\mu_0 M_\mathrm{s} t_\mathrm{FM}}{\gamma_0} \iint \left(\frac{\partial \mathbf{m}}{\partial x_i} \cdot \frac{\partial \mathbf{m}}{\partial x_j} \right) \mathrm{d}x\mathrm{d}y \quad \text{(A.34)}$$

$\mathbf{F}_{ext}$ is the external force originating from magnetic fields, spin-currents, anisotropy gradients, etc.

Eq. (A.32) is the general form for Thiele equation describing the motion of a magnetic texture under the effect of an arbitrary external force. This equation is widely used to investigate the dynamics of several exotic magnetic structure such as skyrmion, vortices, skyrmioniums, bimerons, ...

A.3 DW dynamics driven via strain gradients: Analytical model

In this section we focus our attention on the 1D Model description of the DW motion induced by strain gradients, either in-plane ($\varepsilon_{xx}(x) = \varepsilon'_{xx}x$ with $\varepsilon'_{xx} \equiv \partial\varepsilon_{xx}/\partial x$) or perpendicular ($\varepsilon_{zz}(x) = \varepsilon'_{zz}x$ with $\varepsilon'_{zz} \equiv \partial\varepsilon_{zz}/\partial x$) strain gradients, as discussed in chapter 4.

Considering that the magnetoelastic energy density reads $\mathcal{E}_{\rm mel} = B_1(\varepsilon'_{xx}\, x\cos^2\phi\sin^2\theta - \varepsilon'_{zz}\, x\sin^2\theta)$, the DW surface energy density in presence of the strain gradients reads

$$\mathcal{U}_{\rm DW} \;=\; \frac{2A}{\Delta} \;+\; 2\Delta\left[K_{\rm eff} + K_{\rm sh}\sin^2\varphi + B_1\varepsilon'_{xx}q\cos^2\varphi - B_1\varepsilon'_{zz}q\right] \;+\; \pi QD\cos\varphi \tag{A.35}$$

where $\int_{-\infty}^{+\infty} x\sin^2\theta\,\mathrm{d}x = 2q\Delta$ was used.

The differential of the surface DW energy with respect to q, φ and Δ reads

$$\mathrm{d}\mathcal{U}_{DW} = \frac{\partial\mathcal{U}_{DW}}{\partial q}(\mathrm{d}q) + \frac{\partial\mathcal{U}_{DW}}{\partial\varphi}(\mathrm{d}\varphi) + \frac{\partial\mathcal{U}_{DW}}{\partial\Delta}(\mathrm{d}\Delta) \tag{A.36}$$

where

$$\begin{aligned}
\frac{\partial\mathcal{U}_{DW}}{\partial q} &= 2\Delta B_1\left(\varepsilon'_{xx}\cos^2\varphi - \varepsilon'_{zz}\right)\\
\frac{\partial\mathcal{U}_{DW}}{\partial\varphi} &= 2\Delta\left(K_{\rm sh} - B_1\varepsilon'_{xx}q\right)\sin 2\varphi - \pi QD\sin\varphi\\
\frac{\partial\mathcal{U}_{DW}}{\partial\Delta} &= -\frac{2A}{\Delta^2} + 2\left(K_{\rm eff} + K_{\rm sh}\sin^2\varphi\right) + 2qB_1\left(\varepsilon'_{xx}\cos^2\varphi - \varepsilon'_{zz}\right)
\end{aligned}$$

On the other hand using LLG equation in spherical coordinates as shown in Appendix. A.1, we can express $\mathrm{d}\mathcal{U}_{\rm DW}$ as

$$\begin{aligned}
\mathrm{d}\mathcal{U}_{DW} &= \int_{-\infty}^{+\infty}\delta\mathcal{E}\mathrm{d}x\\
&= -\frac{2\mu_0 M_{\rm s}}{\gamma_0}\left\{\left[\alpha\frac{\dot{q}}{\Delta} + Q\dot{\varphi}\right]\mathrm{d}q + [Q\dot{q} - \alpha\Delta\dot{\varphi}]\mathrm{d}\varphi + \left[\alpha\frac{\pi^2}{12}\frac{\dot{\Delta}}{\Delta}\right]\mathrm{d}\Delta\right\}
\end{aligned} \tag{A.37}$$

where the same identities of Appendix. A.1 are used now.

From Eq. (A.36) and Eq. (A.37) we get the 1D model equations describing the DW dynamics in presence of strain gradients as

$$\alpha\frac{\dot{q}}{\Delta} + Q\dot{\varphi} = -\gamma_0\Delta H_{\mathrm{mel}}\left(\varepsilon'_{xx}\cos^2\varphi - \varepsilon'_{zz}\right) \tag{A.38a}$$

$$-Q\frac{\dot{q}}{\Delta} + \alpha\dot{\varphi} = -\gamma_0\left[\frac{H_{\mathrm{sh}}}{2}\sin 2\varphi - \frac{\pi}{2}QH_{\mathrm{DMI}}\sin\varphi - H_{\mathrm{mel}}\varepsilon'_{xx}q\sin 2\varphi\right] \tag{A.38b}$$

$$\dot{\Delta} = \frac{12\gamma_0}{\alpha\mu_0 M_{\mathrm{s}}\pi^2}\left[\frac{A}{\Delta} - \Delta\left(K_{\mathrm{eff}} + K_{\mathrm{sh}}\sin^2\varphi\right) - \Delta B_1 q\left(\varepsilon'_{xx}\cos^2\varphi - \varepsilon'_{zz}\right)\right] \tag{A.38c}$$

where $H_{\mathrm{sh}} = \frac{2K_{\mathrm{sh}}}{\mu_0 M_{\mathrm{s}}}, H_{\mathrm{DMI}} = \frac{D}{\mu_0 M_{\mathrm{s}}\Delta}$ and $H_{\mathrm{mel}} = \frac{B_1}{\mu_0 M_{\mathrm{s}}}$. These equations, already presented in chapter 4, are presented again here in their general form (including both in-plane and perpendicular contributions):

$$\left(1+\alpha^2\right)\frac{\dot{q}}{\Delta} = -\alpha\Gamma_{\mathrm{A}}(\varphi) + Q\Gamma_{\mathrm{B}}(q,\varphi) \tag{A.39a}$$

$$\left(1+\alpha^2\right)\dot{\varphi} = -Q\Gamma_{\mathrm{A}}(\varphi) - \alpha\Gamma_{\mathrm{B}}(q,\varphi) \tag{A.39b}$$

$$\dot{\Delta} = \frac{12\gamma_0}{\alpha\mu_0 M_{\mathrm{s}}\pi^2}\left[\frac{A}{\Delta} - \Delta\left(K_{\mathrm{eff}} + K_{\mathrm{sh}}\sin^2\varphi\right) - \Delta B_1 q\left(\varepsilon'_{xx}\cos^2\varphi - \varepsilon'_{zz}\right)\right] \tag{A.39c}$$

where

$$\Gamma_{\mathrm{A}}(\varphi) = \gamma_0\Delta H_{\mathrm{mel}}\varepsilon'_{xx}\cos^2\varphi - \gamma_0\Delta H_{\mathrm{mel}}\varepsilon'_{zz}$$

$$\Gamma_{\mathrm{B}}(\varphi,q) = \Gamma_{\mathrm{sh}} + \Gamma_{\mathrm{DMI}} + \Gamma_{\varepsilon'_{xx}}$$

$$= \gamma_0\frac{H_{\mathrm{sh}}}{2}\sin 2\varphi - \gamma_0\frac{\pi}{2}QH_{\mathrm{DMI}}\sin\varphi - \gamma_0 H_{\mathrm{mel}}\varepsilon'_{xx}q\sin 2\varphi$$

Eqs. (A.39a)-(A.39c) are numerically solved for two particular cases: either in-plane ($\varepsilon_{xx}(x) = \varepsilon'_{xx}x$ with $\varepsilon'_{xx} \neq 0$, and $\varepsilon_{zz} = 0$) or perpendicular ($\varepsilon_{zz}(x) = \varepsilon'_{zz}x$ with $\varepsilon'_{zz} \neq 0$, and $\varepsilon_{xx} = 0$) strain gradients. Typical results were shown in chapter 4. However, the 1D model also allows us to extract some analytical results which are described in the following for perpendicular and in-plane cases respectively.

A.3.1 DW dynamics under perpendicular strain gradient

Perpendicular strain gradient (ε'_{zz}) enters in 1D model equations similarly to an equivalent out-of-plane field ($H_{\rm eq} = \Delta H_{\rm mel}\varepsilon'_{zz}$) and, consequently, the DW dynamics under ε'_{zz} is easily predicted from well-known bases of the field-driven DW motion. Under low perpendicular strain gradient, the DW reaches a steady-state regime with constant terminal velocity given by

$$v_t = -\frac{\gamma_0 \Delta}{\alpha} H_{\rm eq} = \frac{\gamma_0 \Delta^2}{\alpha} H_{\rm mel}\varepsilon'_{zz} \tag{A.40}$$

However, there is a limit for this rigid DW motion, the so-called Walker breakdown, which takes place when equivalent driving field ($H_{\rm eq} = \Delta H_{\rm mel}\varepsilon'_{zz}$ is higher than $\left|\frac{\alpha}{2}\pi Q H_{\rm DMI}\right|$). Note also that in our case $H_{\rm DMI} \gg H_{\rm sh}$. Therefore, the Walker breakdown perpendicular strain gradient threshold, $(\varepsilon'_{zz})_{\rm WB}$, reads as

$$(\varepsilon'_{zz})_{\rm WB} = -\frac{1}{\Delta H_{\rm mel}} \left|\frac{\alpha}{2}\pi Q H_{\rm DMI}\right|$$

For perpendicular strain gradient above the Walker breakdown, $\varepsilon'_{zz} > (\varepsilon'_{zz})_{\rm WB}$, the DW depicts a turbulent regime where its internal DW moment precesses periodically whereas the DW displaces as it was shown in Fig. 4.2(a) of chapter 4.

A.3.2 DW dynamics under in-plane strain gradient

Under in-plane strain gradient (ε'_{xx}) the DW dynamics is significantly different and novel. On one hand, the in-plane strain gradient contribution includes a factor $\cos^2\varphi$ $\left(H^{\rm eq}_{\varepsilon'_{xx}}(\varphi) = \Delta H_{\rm mel}\varepsilon'_{xx}\cos^2\varphi\right)$ in the corresponding term of $\Gamma_{\rm A}(\varphi)$ which is not present for the perpendicular gradient case. On the other hand, it also adds a term $\Gamma_{\varepsilon'_{xx}} = -\gamma_0 H_{\rm mel}\varepsilon'_{xx} q \sin 2\varphi$ in $\Gamma_{\rm B}(\varphi, q)$, which is proportional to both the DW position (q) and to the $\sin 2\varphi$, and therefore, competes with the shape anisotropy $\left(\Gamma_{\rm sh} = \gamma_0 \frac{H_{\rm sh}}{2}\sin 2\varphi\right)$ and with the DMI ($\Gamma_{\rm DMI} = -\gamma_0 \frac{\pi}{2} Q H_{\rm DMI}\sin\varphi$) terms. These terms make the DW dynamic induced by in-plane strain gradient significantly different from conventional field-driven case, as already shown in Fig. 4.2 of chapter 4. Indeed, no Walker breakdown occurs for any arbitrarily high in-plane strain gradients, and after a transient the DW depicts a terminal regime where the DW angle goes back asymptotically to 0 (that is, $\varphi(t \to \infty) \equiv \varphi_t \to \varphi_0 \approx 0$) according to

$$\varphi_t = \tan^{-1}\left(\frac{Q\Delta}{2\alpha q}\right) \tag{A.41}$$

which can be deduced by solving $\dot{\varphi} = 0$ in the large time window limit $(t \to \infty)$ where $|\Gamma_{\varepsilon'_{xx}}| \gg |\Gamma_{\rm sh} + \Gamma_{\rm DMI}|$. This is followed by a temporal evolution of the DW velocity that asymptotically approaches to a terminal value (v_t). This terminal velocity can be directly deduced from Eq. (A.39a) by imposing $\varphi = 0$, resulting in

$$v_t = -\frac{\gamma_0}{\alpha}\Delta^2 H_{\rm mel}\varepsilon'_{xx} \tag{A.42}$$

In order to further support our discussion on the transient DW dynamics under in-plane strain gradient (ε'_{xx}), Fig. A.1 shows the temporal evolution of the different torques acting on the DW as corresponding to the Fig. 4.3(b) of the main text. These torques are the four terms on the rhs of Eqs. (A.39a) and (A.39b). As the DW starts from its equilibrium state, before the strain gradient is applied $(t < 0)$, all the torques are identically zero. Upon the application of the strain gradient at $t = 0$, the precession torque due to the in-plane strain gradient $(Q\Gamma_{\rm A})$ suddenly increases its strength. However, the three damping contributions $(\alpha\Gamma_{\rm sh}, \alpha\Gamma_{\rm DMI}, \alpha\Gamma_{\varepsilon'_{xx}})$ gradually evolve away from zero. Fig. A.1 shows that after a transient both $\alpha\Gamma_{\rm sh}$ and $\alpha\Gamma_{\rm DMI}$ tend to zero, whereas the two other torques due to the strain gradient remain finite and compensates each other, $Q\Gamma_{\rm A} = -\alpha\Gamma_{\varepsilon'_{xx}}$, triggering the internal DW moment to return asymptotically to its initial Néel state $(\varphi_t \to \varphi_0 = 0)$. This compensation, which takes place dynamically as the DW moves toward high strain values ($|\varepsilon_{xx}|$ increases as q increases), is the responsible of the absence of Walker breakdown under in-plane strain gradients.

A.3.3 Micromagnetic details and results

In order to further validate our 1DM results of the DW dynamics driven by strain gradients, here we also analyzed them using a full micromagnetic model (μM). The magneto-elastic interaction is introduced as an additional contribution to the effective field, $\mathbf{H}_{\rm mel} = -\frac{1}{\mu_0 M_{\rm s}}\frac{\delta \mathcal{E}_{\rm mel}}{\delta \mathbf{m}}$. Micromagnetic simulations were carried out with $\rm Mumax^3$ [100], with same material parameters as describe before: $M_{\rm s} = 0.58\,\rm MA/m$, $A = 20\,\rm pJ/m$, $K_{\rm u} = 0.9\,\rm MJ/m^3$, $B_1 = 1.2\,\rm MJ/m^3$ ($\lambda_{\rm s} = -5 \times 10^{-5}$, $C_{11} = 298\,\rm GPa$, $C_{12} = 233\,\rm GPa$). Typical μM results are shown in Fig. A.1 for in-plane $(\varepsilon_{xx}(x) = \varepsilon'_{xx}x$ with $\varepsilon'_{xx} \neq 0$, and $\varepsilon_{zz} = 0)$ or perpendicular $(\varepsilon_{zz}(x) = \varepsilon'_{zz}x$ with $\varepsilon'_{zz} \neq 0$, and $\varepsilon_{xx} = 0)$ strain gradients with two different magnitudes: $|\varepsilon'_{ii}| =$

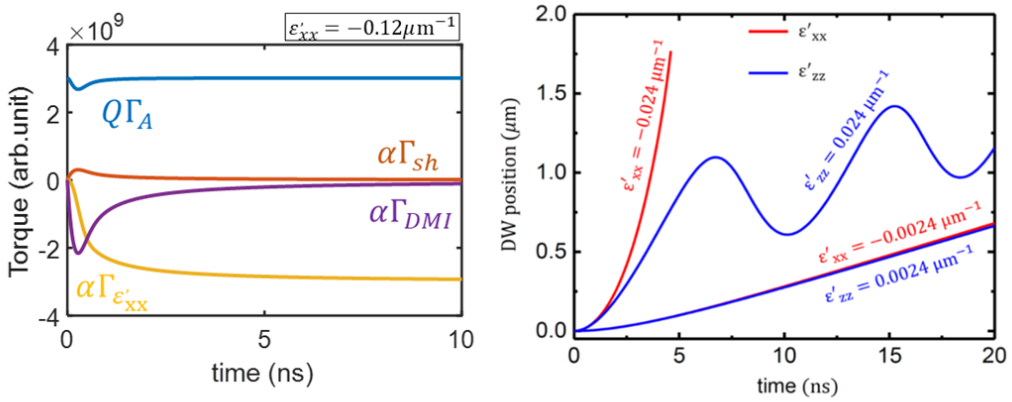

Fig. A.1.: a) Temporal evolution of the different torques entering in Eq. (A.39b) for the DW dynamics under an in-plane strain gradient of $\varepsilon'_{xx} = -0.12\mu\mathrm{m}^{-1}$. b) Micromagnetic results of the temporal evolution of the DW position under in-plane (ε'_{xx}) and perpendicular (ε'_{zz}) strain gradients with two different magnitudes: $|\varepsilon'_{ii}| = 0.0024\mu\mathrm{m}^{-1}$ and $|\varepsilon'_{ii}| = 0.024\mu\mathrm{m}^{-1}$ ($i : x$ for in-plane strain gradient, or $i : z$ for perpendicular strain gradient). Material parameters and dimensions are provided in Chapter 4.

$0.0024\mu\mathrm{m}^{-1}$ and $|\varepsilon'_{ii}| = 0.024\mu\mathrm{m}^{-1}$. Here the DMI and damping parameters are $D = -0.5\ \mathrm{mJ/m^2}$ and $\alpha = 0.01$ respectively. As it can be observed in Fig. A.1 and similar to 1D model predictions, for perpendicular strain gradient the DW dynamics is rigid for small strain gradients $(\varepsilon'_{zz} = 0.0024\,\mu\mathrm{m}^{-1})$, but it becomes turbulent above a Walker breakdown threshold (see blue curve for $\varepsilon'_{zz} = 0.024\,\mu\mathrm{m}^{-1}$ rigid regime for any arbitrary strain gradient (see red curves in Fig. A.1 for both $\varepsilon'_{xx} = 0.0024\mu\mathrm{m}^{-1}$ and $\varepsilon'_{xx} = 0.024\mu\mathrm{m}^{-1}$).

A.4 Internal magnetic DW twist in presence of uniform strain: Mathematical details

A.4.1 Extended collective coordinates model for DW dynamics

In this section we will present the derivation of the 2D collective coordinate model used in chapter 5.

As discussed in chapter 5, we extended the collective coordinates model [101, 103, 107] to account for both space and time variation of the DW degrees of freedom. To do so, we used a modified Walker ansatz to include the space variation of both the DW position $q(t, y)$ and its internal angle $\varphi(t, y)$ as follows

$$\begin{cases} \theta(x, y, t) = 2 \operatorname{atan}\left(e^{\frac{x-q(y,t)}{\Delta}}\right) \\ \varphi(x, y, t) = \varphi(y, t) \end{cases} \tag{A.43}$$

where θ and φ are the spherical coordinates of the magnetization as explain in chapter 5.

Our work was mainly focused on DWs in a PMA system in presence of the magneto-elastic anisotropy contribution due to a longitudinal in-plane strain ε_{xx}. In this case, our DW total energy density reads

$$\mathcal{U}_{\mathrm{DW}} = \int_{-\infty}^{+\infty} [A_{\mathrm{ex}}(\nabla \mathbf{m})^2 - K_{\mathrm{u}} m_z^2 - \frac{\mu_0 M_s}{2} \mathbf{m} \cdot \mathbf{H}_{\mathrm{d}} + B_1 \, \varepsilon_{xx} \, m_x^2] \, dx \tag{A.44}$$

Plugging the ansatz Eq. (A.43) in Eq. (A.44) and integrating it, yields

$$\mathcal{U}_{\mathrm{DW}} = A_{\mathrm{ex}} \left[\frac{2}{\Delta} - \frac{4}{\Delta} \frac{\mathrm{d}q(y,t)}{\mathrm{d}y} + \frac{2}{\Delta} \left(\frac{\mathrm{d}q(y,t)}{\mathrm{d}y} \right)^2 + 2\Delta \left(\frac{\mathrm{d}\varphi(y,t)}{\mathrm{d}y} \right) \right] + 2\Delta K_{\mathrm{eff}} + 2\Delta K_{\mathrm{sh}} \sin^2(\varphi) + 2\Delta B_1 \varepsilon_{xx} \cos^2(\varphi) \tag{A.45}$$

where Eq. (A.45) describes the DW energy per unit area, and was calculated using the same set of integrals shown in Appendices.A.1 and A.2.

The differential of the DW energy density Eq. (A.45) reads

$$\mathrm{d}\mathcal{U}_{\mathrm{DW}} = \frac{\partial \mathcal{U}_{\mathrm{DW}}}{\partial q(y,t)}\mathrm{d}q(y,t) + \frac{\partial \mathcal{U}_{\mathrm{DW}}}{\partial \varphi(y,t)}\mathrm{d}\varphi(y,t) \tag{A.46}$$

with

$$\frac{\partial \mathcal{U}_{\mathrm{DW}}}{\partial q(y,t)} = \frac{4A_{\mathrm{ex}}}{\Delta}\frac{\mathrm{d}^2 q(y,t)}{\mathrm{d}y^2} \tag{A.47a}$$

$$\frac{\partial \mathcal{U}_{\mathrm{DW}}}{\partial \varphi(y,t)} = 4A_{\mathrm{ex}}\Delta\frac{\mathrm{d}^2\varphi(y,t)}{\mathrm{d}y^2} + 2\Delta\sin 2\varphi\left(K_{\mathrm{sh}} - B_1\varepsilon_{xx}\right) \tag{A.47b}$$

On the other hand, the energy variation can also be evaluated from LLG equation. To do so we need first to write this equation in spherical coordinates. Considering that the magnetization derivative reads $\mathrm{d}\mathbf{m} = \mathrm{d}\theta\,\mathbf{e}_\theta + \sin\theta\,\mathrm{d}\varphi\,\mathbf{e}_\varphi$ and the effective field can be written as $\mathbf{H}_{\mathrm{eff}} = -\frac{1}{\mu_0 M_{\mathrm{s}}}\frac{\delta\mathcal{E}}{\delta\theta}\mathbf{e}_\theta - \frac{1}{\mu_0 M_{\mathrm{s}}\sin\theta}\frac{\delta\mathcal{E}}{\delta\varphi}\mathbf{e}_\varphi$, LLG equation can be rearranged as

$$\begin{cases} \dot{\theta} = -\frac{\gamma_0}{\mu_0 M_{\mathrm{s}}\sin\theta}\frac{\delta\mathcal{E}}{\delta\varphi} - \alpha\,\sin\theta\dot{\varphi} - \gamma_0 H_{\mathrm{SOT}}\cos\theta\sin\phi \\ \dot{\varphi} = \frac{1}{\sin\theta}\left(\frac{\gamma_0}{\mu_0 M_{\mathrm{s}}}\frac{\delta\mathcal{E}}{\delta\theta} - \alpha\,\dot{\theta} - \gamma_0 H_{\mathrm{SOT}}\cos\theta\right) \end{cases} \tag{A.48}$$

where $\mathcal{E}$ is the total energy of the system per unit volume. Hence, the DW energy variation can be deduced from LLG equation Eq. (A.48) as

$$\begin{aligned} \mathrm{d}\mathcal{U}_{\mathrm{DW}} = \frac{2\mu_0 M_{\mathrm{s}}}{\gamma_0}\left[-\dot{\varphi}(y,t) - \alpha\frac{\dot{q}(y,t)}{\Delta} - \gamma_0 H_{\mathrm{SOT}}\cos\varphi(y,t)\right]\mathrm{d}q(y,t) \\ + \frac{2\mu_0 M_{\mathrm{s}}}{\gamma_0}\left[\dot{q}(y,t) - \alpha\Delta\dot{\varphi}(y,t)\right]\mathrm{d}\varphi(y,t) \end{aligned} \tag{A.49}$$

By direct comparison of Eq. (A.46) and Eq. (A.49), the partial differential dynamic equations describing the evolution of the DW position and its internal angle are

$$(1+\alpha^2)\partial_t\frac{q}{\Delta} = \alpha\mathcal{D}\partial_{yy}\frac{q}{\Delta} - \alpha\Gamma_{\mathrm{SOT}} - \mathcal{D}\partial_{yy}\varphi + \Gamma_{\mathrm{AN}} \tag{A.50}$$

$$(1+\alpha^2)\partial_t\varphi = \mathcal{D}\partial_{yy}\frac{q}{\Delta} - \Gamma_{\mathrm{SOT}} + \alpha\mathcal{D}\partial_{yy}\varphi - \alpha\Gamma_{\mathrm{AN}} \tag{A.51}$$

where $\mathcal{D} = \frac{2\gamma_0 A_{\mathrm{ex}}}{\mu_0 M_{\mathrm{s}}}$ is a dispersive-like constant, $\Gamma_{\mathrm{SOT}} = \frac{\gamma_0\pi}{2}H_{\mathrm{SOT}}\cos\varphi$ is the SOT torque and $\Gamma_{\mathrm{AN}} = \gamma_0 H_{AN}\sin 2\varphi$ is the in-plane anisotropy torque. $H_{AN} = \frac{H_{\mathrm{sh}}}{2} - H_{\mathrm{mel}}\varepsilon_{xx}$ is the in-plane anisotropy field including the magnetoelastic and shape contributions.

A.4.2 Linear stability analysis

As mentioned in chapter 5, with aim to determine the critical width above which the 1D solution of the DW internal structure is unstable, we carry out a linear stability analysis (LSA) of Eq. (A.50) and Eq. (A.51) [207, 208]. To do so, let us reconsider the two equation in Eq. (A.50) and Eq. (A.51) and rewrite them using a redefinition of constants to simplify them as

$$\partial_t q = \sigma_1 \partial_{yy} q \overbrace{-\sigma_3 \Delta\alpha \cos\varphi - \sigma_2 \Delta \partial_{yy}\varphi + \sigma_4 \Delta \sin 2\varphi}^{f(q,\varphi,\xi)} \tag{A.52}$$

$$\partial_t \varphi = \sigma_1 \partial_{yy} \varphi \underbrace{-\sigma_3 \cos\varphi + \frac{\alpha\sigma_2}{\Delta}\partial_{yy} q - \alpha\sigma_4 \sin 2\varphi}_{g(q,\varphi,\xi)} \tag{A.53}$$

where $\sigma_1 = \Gamma_{\mathrm{G}} \frac{2A_{\mathrm{ex}}}{\mu_0 M_s}$, $\sigma_2 = \Gamma_{\mathrm{LL}} \frac{2A_{\mathrm{ex}}}{\mu_0 M_s}$, $\sigma_3 = \Gamma_{\mathrm{LL}} \frac{\pi}{2} H_{\mathrm{SOT}}$ and $\sigma_4 = \Gamma_{\mathrm{LL}} \left(\frac{H_{\mathrm{sh}}}{2} - H_{\mathrm{mel}} \varepsilon_{xx} \right)$ with $\Gamma_{\mathrm{LL}} = \frac{\gamma_0}{1+\alpha^2}$ and $\Gamma_{\mathrm{G}} = \frac{\alpha\gamma_0}{1+\alpha^2}$.

Eqs. (A.52) and (A.53) can be rewritten as

$$\partial_t q = \sigma_1 \partial_{yy} q + f(q, \varphi, \xi) \tag{A.54}$$

$$\partial_t \varphi = \sigma_1 \partial_{yy} \varphi + g(q, \varphi, \xi) \tag{A.55}$$

where the solution domain of Eq. (A.54) and Eq. (A.55) is $\mathrm{D} = [0, W]$ with W being the width of the ferromagnetic strip and ξ is an arbitrary control parameter that can induce bifurcations in the system.

Let us now consider that $q = q_0 + \tilde{q}$ and $\varphi = \varphi_0 + \tilde{\varphi}$ with q_0, φ_0 being the homogeneous solutions and $\tilde{q}$,$\tilde{\varphi}$ are infinitesimal perturbation to the homogeneous state. We then need to incorporate the width W explicitly into the equations. To do so, we use the transformation $y \to Wy$, which changes the domain $\mathrm{D} = [0, W]$ to the unit interval $\mathrm{D} = [0, 1]$. Using these assumption, Eqs. (A.54) and (A.55) become

$$\partial_t \tilde{q} = \frac{\sigma_1}{W^2} \partial_{yy} \tilde{q} + f(q_0 + \tilde{q}, \varphi_0 + \tilde{\varphi}, \xi) \tag{A.56}$$

$$\partial_t \tilde{\varphi} = \frac{\sigma_1}{W^2} \partial_{yy} \tilde{\varphi} + g(q_0 + \tilde{q}, \varphi_0 + \tilde{\varphi}, \xi) \tag{A.57}$$

Using $U = \begin{pmatrix} \tilde{q} \\ \tilde{\varphi} \end{pmatrix}$ we can rewrite the equations above as

$$\partial_t U = F(U, \xi) \tag{A.58}$$

where $F(U,\xi) = \begin{pmatrix} \frac{\sigma_1}{W^2}\partial_{yy}\tilde{q} \\ \frac{\sigma_1}{W^2}\partial_{yy}\tilde{\varphi} \end{pmatrix} + \begin{pmatrix} f(q_0+\tilde{q}, \varphi_0+\tilde{\varphi}, \xi) \\ g(q_0+\tilde{q}, \varphi_0+\tilde{\varphi}, \xi) \end{pmatrix}$.

Differentiating F with respect to U at the homogeneous equilibrium $U_0 = \begin{pmatrix} 0 \\ \frac{\pi}{2} \end{pmatrix}$, we obtain L, the linearization of F, as

$$L = \begin{pmatrix} \frac{\sigma_1}{W^2}\partial_{yy} & 0 \\ 0 & \frac{\sigma_1}{W^2}\partial_{yy} \end{pmatrix} + \begin{pmatrix} \partial_{\tilde{q}} f(q_0, \varphi_0, \xi) & \partial_{\tilde{\varphi}} f(q_0, \varphi_0, \xi) \\ \partial_{\tilde{q}} g(q_0, \varphi_0, \xi) & \partial_{\tilde{\varphi}} g(q_0, \varphi_0, \xi) \end{pmatrix} \tag{A.59}$$

Subsequently, stability of U_0 can be analyzed via solutions of

$$\partial_t U = LU \tag{A.60}$$

Since our interest is to investigate the stability of the steady state homogeneous solutions, we limit our analysis to the steady state with $\partial_t U = 0$. Then we can analyse the spectrum of L assuming an ansatz solution as $U = A\sin(k\,\pi\,y)$ which gives

$$LU = M_k A \sin(k\,\pi\,y) \tag{A.61}$$

where

$$M_k = \begin{pmatrix} -\frac{\pi^2\sigma_1 k}{W^2} + \partial_{\tilde{q}} f(q_0, \varphi_0, \xi) & \partial_{\tilde{\varphi}} f(q_0, \varphi_0, \xi) \\ \partial_{\tilde{q}} g(q_0, \varphi_0, \xi) & -\frac{\pi^2\sigma_1 k}{W^2} + \partial_{\tilde{\varphi}} g(q_0, \varphi_0, \xi) \end{pmatrix}$$

Then, the homogeneous solution U_0 is stable if and only if

$$\mathbf{Tr}(M_k) < 0 \tag{A.62}$$

and

$$\mathbf{Det}(M_k) > 0 \tag{A.63}$$

Using the two conditions in Eq. (A.62) and Eq. (A.63), we end the up with a system of two inequations as

$$\begin{cases} \frac{\sigma_1}{W^2}\pi^2k^2 + \sigma_3 + \pi^2k^2\frac{\sigma_1}{W^2} + 2\alpha\sigma_4 < 0 \\ \frac{-\sigma_1}{W^2}\pi^2k^2(\sigma_3 - \pi^2k^2\frac{\sigma_1}{W^2} + 2\alpha\sigma_4) + \frac{\sigma_2}{\Delta W^2}\pi^2k^2(\sigma_3\Delta\alpha + \frac{\sigma_2\Delta}{W^2}\pi^2k^2 - 2\sigma_4\Delta) > 0 \end{cases} \tag{A.64}$$

Solving the inequations in Eq. (A.64) for W, we obtain the critical width over which the homogeneous steady state solution becomes unstable for $k = 1$ as

$$W > \pi\sqrt{\frac{A_{\mathrm{ex}}}{K_{\mathrm{sh}} - B_1\varepsilon_{xx}}} \tag{A.65}$$

Eq. (A.65) represents the critical width above which the uniform solution of Eqs. (A.50) and (A.51) becomes unstable. As discussed in chapter 5, bellow this critical width the DW internal structure at the steady state depicts a Bloch pattern. In contrary, when the strip width is larger then then critical one the DW depicts non-uniform patterns, which we called $kinks$.

List of Publications

B

- **Mouad Fattouhi**, Kai Yu Mak, Yan Zhou, Xichao Zhang, Xiaoxi Liu, and Mohamed El Hafidi. *Logic Gates Based on Synthetic Antiferromagnetic Bilayer Skyrmions*. **Physical Review Applied**, 16, 014040(2021).

- Giovanni Masciocchi, **Mouad Fattouhi**, Andreas Kehlberger, Luis Lopez-Diaz, Maria-Andromachi Syskaki, and Mathias Kläui. *Strain-controlled domain wall injection into nanowires for sensor applications*. **Journal of Applied Physics**, 130, 183903(2021).

- Kai Yu Mak, Jing Xia, Xi-Chao Zhang, Li Li, **Mouad Fattouhi**, Motohiko Ezawa, Xiao-Xi Liu, and Yan Zhou. *Single-bit full adder and logic gate based on synthetic antiferromagnetic bilayer skyrmions*. **Rare Metals**, 41, 2249–2258 (2022).

- **Mouad Fattouhi**, Felipe Garcia-Sanchez, Rocio Yanes, Victor Raposo, Eduardo Martinez, and Luis Lopez-Diaz. *Electric Field Control of the Skyrmion Hall Effect in Piezoelectric-Magnetic Devices*. **Physical Review Applied**, 16, 044035(2021).

- Johannes W. van der Jagt, Vincent Jeudy, André Thiaville, Mamour Sall, Nicolas Vernier, Liza Herrera-Diez, Mohamed Belmeguenai, Yves Roussigné, Salim M. Chérif, **Mouad Fattouhi**, Luis Lopez-Diaz, Alessio Lamperti, Roméo Juge, and Dafiné Ravelosona. *Revealing Nanoscale Disorder in W/CoFeB/MgO Ultrathin Films Using Domain-Wall Motion*. **Physical Review Applied**, 18, 054072(2022).

- **Mouad Fattouhi**, Felipe Garcia-Sanchez, Rocio Yanes, Victor Raposo, Eduardo Martinez, and Luis Lopez-Diaz. *Absence of Walker Breakdown in the Dynamics of Chiral Néel Domain Walls Driven by In-Plane Strain Gradients*. **Physical Review Applied**, 18, 044023(2022).

- Zilu Wang, Pingzhi Li, **Mouad Fattouhi**, Yuxuan Yao, Youri L.W. Van Hees, Casper F. Schippers, Xueying Zhang, Reinoud Lavrijsen, Felipe Garcia-Sanchez, Eduardo Martinez, Albert Fert, Weisheng Zhao, and Bert Koopmans. *Field-free spin orbit-torque switching of synthetic antiferromagnet through interlayer Dzyaloshinskii-Moriya interaction*. **Cell reports physical science**, 4, 101334(2023).

- Giovanni Masciocchi, **Mouad Fattouhi**, Elizaveta Spetzler, Maria-A.Syskaki, Roland Lehndorff, Eduardo Martinez, Jeffrey McCord, Luis Lopez-Diaz, Andreas Kehlberger, and Mathias Kläui. *Generation of imprinted strain gradients for spintronics*. **Applied Physics Letters**,123, 022404(2023).
- **Mouad Fattouhi**, André Thiaville, Felipe Garcia-Sanchez, Eduardo Martinez, and Luis Lopez-Diaz. *Dissipative Soliton Explosion in Spin-Orbit Torque Driven Magnetic Domain Wall Systems*. To be submitted, (2023).
- Adrien. A. D. Petrillo, **Mouad Fattouhi**, Adriano Di Pietro, Luis Lopez-Diaz, Gianfranco Durin, Bert Koopmans, and Reinoud Lavrijsen. *Optimization of VCMA effect for the manipulation of dipolar-dominated propagating spin waves*. To be submitted, (2023).
- Shen Li, **Mouad Fattouhi**, Tianxun Huang, Chen Lv, Mark C. H. de Jong, Pingzhi Li, Zilu Wang, Stéphane Mangin, Eduardo Martinez, Felipe Garcia-sanchez, Bert Koopmans, Reinoud Lavrijsen, Xiaoyang Lin and Weisheng Zhao. *Unraveling the role of interlayer Dzyaloshinskii–Moriya interaction in the hysteresis loop and spin-orbit torque switching of synthetic antiferromagnet*. To be submitted, (2023).